CHAPTER

Radiation and scattering of sound by the boundary integral method 13

CHAPTER OUTLINE

Acoustics: Sound Fields and Transducers. DOI: 10.1016/B978-0-12-391421-7.00013-0

PART XXXV: BOUNDARY INTEGRALS AND THE GREEN'S FUNCTION

13.1 THE HUYGENS–FRESNEL PRINCIPLE

The Huygens–Fresnel principle states that each point on the wave front of a propagating wave can be replaced with a point source as illustrated in Fig. 13.1, thus creating an array of wavelets whereby each wavelet is unaffected by the presence of all the other wavelets. Some time later, the wave front is equivalent to the envelope of these wavelets. In other words, the resultant field is due to the sum of the point sources, using the principle of superposition. The point sources can be monopoles or dipoles. Although the forward propagating wave remains unaltered, the principle does not explain the creation of a backward propagating wave that was not present in the original. However, if the surface over which the point sources are distributed encloses fully the original source(s), we can use the principle to analyse the internal or external fields separately. It can also be used to analyse sound radiation from vibrating surfaces, which may or may not be closed, provided that the boundary conditions are correct.

13.2 THE RAYLEIGH INTEGRALS AND GREEN'S FUNCTION

In this section, monopole and dipole boundary integrals are derived in an intuitive way based upon the Huygens–Fresnel principle whereby monopole and dipole point sources are summed over surfaces. A more mathematically rigorous treatment follows in Sec. 13.3. We have treated all problems so far in this text as *boundary value problems* based upon solutions to the following *homogeneous* Helmholtz wave equation in an arbitrary coordinate system:

$$(\nabla^2 + k^2)\tilde{p}(\mathbf{r}) = 0, \tag{13.1}$$

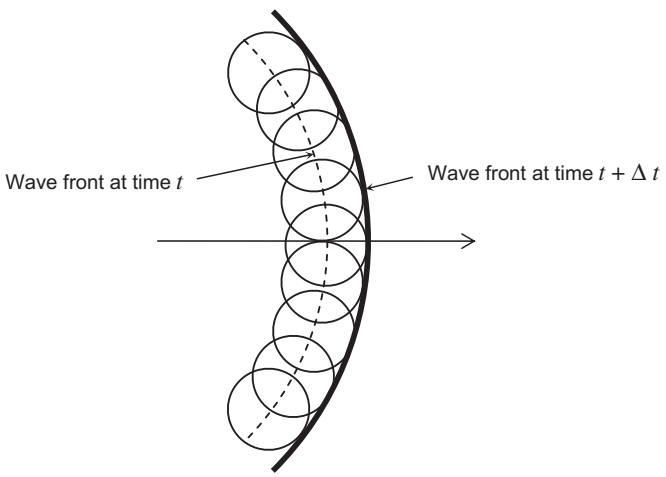

FIG. 13.1 Huygens–Fresnel principle.

where, for example, in rectangular coordinates $(\mathbf{r}) = (x,y,z)$ and the Laplacian ∇^2 is given in rectangular, cylindrical, and spherical coordinates by Eqs. (2.112), (2.125), and (2.146) respectively. By *homogeneous*, we mean that that the equation describes waves that could exist, but there are no driving forces or velocities present in the equation to create them. These come later from the boundary conditions. In general, the boundary value method involves solving the homogeneous Helmholtz wave equation in a suitable orthogonal coordinate system such that it becomes a separable equation. That is, the equation is split into a set of differential equations, each with respect to one ordinate only, as described in Secs. 2.9 to 2.11. The solutions to those equations then contain constants which can be determined by applying boundary conditions. By a suitable coordinate system, we mean one which first must lead to a separable wave equation (if there is more than one ordinate involved) and second fits the geometry of the problem, by which we mean that boundary conditions can be applied by setting pressure or velocity to specific values at constant ordinate values. The simplest example is the pulsating sphere which is solved by setting the particle velocity at the surface of the sphere, where the radial ordinate is equal to the sphere's radius. In the limit, when the radius approaches zero, this leads to the pressure field due to a point source as defined in Eq. (4.71). Let us now recast this equation in the following form:

$$\tilde{p}(\mathbf{r}|\mathbf{r}_0) = -jk\rho_0 c\tilde{U}_0 g(\mathbf{r}|\mathbf{r}_0), \tag{13.2}$$

where $\mathbf{r}$ and $\mathbf{r}_0$ are the positions of the observation point and source respectively in an arbitrary coordinate system. The function $g(\mathbf{r}|\mathbf{r}_0)$ is known as the *Green's function* and is defined by

$$g(\mathbf{r}|\mathbf{r}_0) = \frac{e^{-jk(\mathbf{r}-\mathbf{r}_0)}}{4\pi(\mathbf{r}-\mathbf{r}_0)}. \tag{13.3}$$

For example, in rectangular coordinates, we would write

$$g(x,y,z|x_0,y_0,z_0) = \frac{e^{-jk\sqrt{(x-x_0)^2+(y-y_0)^2+(z-z_0)^2}}}{4\pi\sqrt{(x-x_0)^2+(y-y_0)^2+(z-z_0)^2}}. \tag{13.4}$$

The Green's function is a useful short hand for the spatial distribution due to a point source, but does not indicate its absolute strength. In this instance, it tells us that the sound pressure varies sinusoidally as it spreads outwards from the source and its amplitude is inversely proportional to the distance from the source. It should be noted that there is a singularity at $\mathbf{r} = \mathbf{r}_0$. Using the Huygens–Fresnel principle we can treat a vibrating surface as an array of point sources, or rather surface elements which in the limit shrink to points. In the case of a closed surface (i.e., that which fully encloses a volume) we need not worry about the back wave when considering the external field. The volume velocity of each surface element is given by

$$\tilde{U}_0(\mathbf{r}_0) = \tilde{u}_0(\mathbf{r}_0)\delta S_0, \tag{13.5}$$

where δS_0 is the area of the surface element and $\tilde{u}_0(\mathbf{r}_0)$ is the velocity *normal to the surface* at point $\mathbf{r}_0$. The radiated field is the sum of the fields due to all the point sources so that

$$\tilde{p}_M(\mathbf{r}) = jk\rho_0 c \iint \tilde{u}_0(\mathbf{r}_0) g(\mathbf{r}|\mathbf{r}_0) dS_0, \tag{13.6}$$

which is known as the *monopole Rayleigh integral*. Furthermore, using the relationship

$$\tilde{u}_0(\mathbf{r}_0) = \frac{1}{-jk\rho_0 c}\frac{\partial}{\partial n_0}\tilde{p}(\mathbf{r}_0) \tag{13.7}$$

leads to

$$\tilde{p}_M(\mathbf{r}) = -\iint \frac{\partial}{\partial n_0}\tilde{p}(\mathbf{r}_0)g(\mathbf{r}|\mathbf{r}_0)dS_0. \tag{13.8}$$

Similarly, the surface can be made up of dipole point sources, each comprising two monopole point sources of opposite polarity, separated by a distance Δz_0 which tends to zero. Let the Green's function be defined in axisymmetric spherical-cylindrical coordinates by

$$g(r,\theta|z_0) = \frac{e^{-jkr_1}}{4\pi r_1}, \tag{13.9}$$

where

$$r_1^2 = r^2 + z_0^2 - 2rz_0\cos\theta$$

and θ is the inclination angle of the observation point relative to the z-axis, which passes through the two monopole point sources. The dipole point source is located a distance z_0 from the origin and r is the distance from the observation point to the origin. The gradient of the Green's function in the z direction is then given by

$$\frac{\partial}{\partial z_0}g(r,\theta|z_0)|_{z_0=0} = \left(\frac{1}{r}+jk\right)\cos\theta\frac{e^{-jkr}}{4\pi r}. \tag{13.10}$$

From Eq. (4.114), the field due to a single dipole point source has previously been shown to be

$$\tilde{p}(r,\theta) = -jk\rho_0 c\tilde{U}_0 b\left(\frac{1}{r}+jk\right)\cos\theta\frac{e^{-jkr}}{4\pi r}, \tag{13.11}$$

which after substituting Eq. (13.10) and letting $b = \Delta z_0$ becomes

$$\tilde{p}(r,\theta) = -jk\rho_0 c\tilde{U}_0\Delta z_0\frac{\partial}{\partial z_0}g(r,\theta|z_0)|_{z_0=0}. \tag{13.12}$$

Again, using the relationships of Eqs. (13.5) and (13.7), together with

$$\Delta z_0\frac{\partial\tilde{p}_0}{\partial z_0}\bigg|_{\Delta z_0\to 0} = \tilde{p}_0, \tag{13.13}$$

leads to

$$\tilde{p}(r,\theta) = \tilde{p}_0\frac{\partial}{\partial z_0}g(r,\theta|z_0)|_{z_0=0}\delta S_0, \tag{13.14}$$

which is then integrated over the surface to give

$$\tilde{p}_D(\mathbf{r}) = \iint \tilde{p}(\mathbf{r}_0)\frac{\partial}{\partial n_0}g(\mathbf{r}|\mathbf{r}_0)dS_0 \tag{13.15}$$

in any coordinate system. This is known as the *dipole Rayleigh integral*. We note that the derivative of the Green's function is taken with respect to the normal n_0 to the surface because the axis of each dipole element must be normal to the surface.

13.3 THE KIRCHHOFF–HELMHOLTZ BOUNDARY INTEGRAL

In the previous section we introduced the Green's function

$$g(\mathbf{r}|\mathbf{r}_0) = \frac{e^{-jk(\mathbf{r}-\mathbf{r}_0)}}{4\pi(\mathbf{r}-\mathbf{r}_0)}, \tag{13.16}$$

which turns out to be a solution of the following *inhomogeneous* wave equation:

$$(\nabla^2 + k^2)g(\mathbf{r}|\mathbf{r}_0) = -\delta(\mathbf{r}-\mathbf{r}_0). \tag{13.17}$$

An important principle in acoustics is that of *reciprocity* whereby the locations of the sound source $\mathbf{r}_0$ and its observation point $\mathbf{r}$ are interchangeable. It can be seen that Eqs. (13.16) and (13.17) are unaffected by interchanging $\mathbf{r}$ and $\mathbf{r}_0$. Hence

$$g(\mathbf{r}|\mathbf{r}_0) = g(\mathbf{r}_0|\mathbf{r}) \tag{13.18}$$

and

$$\delta(\mathbf{r}-\mathbf{r}_0) = \delta(\mathbf{r}_0-\mathbf{r}). \tag{13.19}$$

Equation (13.17) differs from the *homogeneous* wave equation (13.1) in that the Dirac delta function δ on the right hand side represents the excitation at the point $\mathbf{r}_0$. Equation (13.17) describes the normalized pressure field (that is, divided by $ik\rho c\tilde{U}_0$) of a point source. However, it is desirable to solve the following inhomogeneous wave equation for *any* source distribution:

$$(\nabla^2 + k^2)\tilde{p}(\mathbf{r}) = -\tilde{f}(\mathbf{r}). \tag{13.20}$$

where $\tilde{f}(\mathbf{r})$ is a source pressure distribution in Pa/m^2. This can be achieved [1,2] by multiplying Eq. (13.17) by $\tilde{p}(\mathbf{r})$ and then subtracting it from Eq. (13.20) multiplied by $g(\mathbf{r}|\mathbf{r}_0)$, which leads to

$$g(\mathbf{r}|\mathbf{r}_0)\nabla^2\tilde{p}(\mathbf{r}) - \tilde{p}(\mathbf{r})\nabla^2 g(\mathbf{r}|\mathbf{r}_0) = \tilde{p}(\mathbf{r})\delta(\mathbf{r}-\mathbf{r}_0) - g(\mathbf{r}|\mathbf{r}_0)\tilde{f}(\mathbf{r}). \tag{13.21}$$

Using the reciprocity relationships of Eqs. (13.18) and (13.19), we can exchange $\mathbf{r}$ and $\mathbf{r}_0$ in Eq. (13.21) and integrate over an arbitrary volume containing all the sources in order to obtain

$$\begin{aligned}&\iiint \Big(g(\mathbf{r}|\mathbf{r}_0)\nabla_0^2\tilde{p}(\mathbf{r}_0) - \tilde{p}(\mathbf{r}_0)\nabla_0^2 g(\mathbf{r}|\mathbf{r}_0)\Big)dV_0 \\ &= \iiint \tilde{p}(\mathbf{r}_0)\delta(\mathbf{r}-\mathbf{r}_0)dV_0 - \iiint g(\mathbf{r}|\mathbf{r}_0)\tilde{f}(\mathbf{r}_0)dV_0,\end{aligned} \tag{13.22}$$

where the zero subscripts indicate differentiation with respect to the $\mathbf{r}_0$ coordinates. Using Green's theorem [3], which essentially states that anything created within a diverging volume passes through its outer surface, the volume integral of the term in parentheses can be replaced with a surface integral:

$$\begin{aligned}\iiint \Big(g(\mathbf{r}|\mathbf{r}_0)\nabla_0^2\tilde{p}(\mathbf{r}_0) - \tilde{p}(\mathbf{r}_0)\nabla_0^2 g(\mathbf{r}|\mathbf{r}_0)\Big)dV_0 \\ = \iiint \nabla_0\Big(g(\mathbf{r}|\mathbf{r}_0)\nabla_0\tilde{p}(\mathbf{r}_0) - \tilde{p}(\mathbf{r}_0)\nabla_0 g(\mathbf{r}|\mathbf{r}_0)\Big)dV_0 \\ = \iint \left(g(\mathbf{r}|\mathbf{r}_0)\frac{\partial}{\partial n_0}\tilde{p}(\mathbf{r}_0) - \tilde{p}(\mathbf{r}_0)\frac{\partial}{\partial n_0}g(\mathbf{r}|\mathbf{r}_0)\right)dS_0,\end{aligned} \tag{13.23}$$

where the surface of integration bounds the volume of the original volume integral and the Laplace operator is replaced with a first-order derivative normal to the surface, pointing away from the space enclosed by the surface integral. We can verify the first step of Eq. (13.23) by working backwards. Although taking the derivative of the two products in the second line leads to four terms, two of them cancel to leave the remaining two terms in the first line. The third line is obtained from the second by the divergence theorem of Gauss. Inserting Eq. (13.23) into Eq. (13.22) and using the property of the Dirac delta function to solve the volume integral $\tilde{p}(\mathbf{r}_0)\delta(\mathbf{r}-\mathbf{r}_0)$ yields

$$\tilde{p}(\mathbf{r}) = \tilde{p}_V(\mathbf{r}) + \tilde{p}_S(\mathbf{r}), \tag{13.24}$$

where $\tilde{p}_V(\mathbf{r})$ is a volume integral given by

$$\tilde{p}_V(\mathbf{r}) = \iiint g(\mathbf{r}|\mathbf{r}_0)\tilde{f}(\mathbf{r}_0)dV_0 \tag{13.25}$$

and $\tilde{p}_S(\mathbf{r})$ is the Kirchhoff–Helmholtz surface integral given by

$$\tilde{p}_S(\mathbf{r}) = \tilde{p}_M(\mathbf{r}) + \tilde{p}_D(\mathbf{r}) \tag{13.26}$$

where $\tilde{p}_M(\mathbf{r})$ is the monopole integral given by

$$\tilde{p}_M(\mathbf{r}) = \iint g(\mathbf{r}|\mathbf{r}_0)\frac{\partial}{\partial n_0}\tilde{p}(\mathbf{r}_0)dS_0 \tag{13.27}$$

and $\tilde{p}_D(\mathbf{r})$ is the dipole integral given by

$$\tilde{p}_D(\mathbf{r}) = -\iint \tilde{p}(\mathbf{r}_0)\frac{\partial}{\partial n_0}g(\mathbf{r}|\mathbf{r}_0)dS_0. \tag{13.28}$$

What is remarkable about Eq.(13.24) is that, merely given a solution $g(\mathbf{r}|\mathbf{r}_0)$ to the wave equation for a point source, it provides a solution for the pressure field $\tilde{p}(\mathbf{r})$ everywhere in the presence of an arbitrary source distribution $\tilde{f}(\mathbf{r}_0)$ within the volume of integration.

It should be noted that in this instance, the integrals $\tilde{p}_M(\mathbf{r})$ and $\tilde{p}_D(\mathbf{r})$ have nothing to do with reflections, although they can be applied to problems of scattering surfaces when appropriate boundary conditions are applied. The volume of integration does not have a physical reflecting boundary surface but a transparent notional one. Inside the volume, $\tilde{p}_M(\mathbf{r})$ and $\tilde{p}_D(\mathbf{r})$ cancel each other so that there is no net contribution from $\tilde{p}_S(\mathbf{r})$, and the field is entirely given by the volume integral, or

$$\tilde{p}(\mathbf{r})\Big|_{\mathbf{r}\in V_0} = \tilde{p}_V(\mathbf{r}), \quad \tilde{p}_S(\mathbf{r}) = 0, \quad \tilde{p}_M(\mathbf{r}) = -\tilde{p}_D(\mathbf{r}) = -\tilde{p}_V(\mathbf{r})/2. \tag{13.29}$$

However, outside the boundary, the field due to the surface integral cancels the field due to the volume integral:

$$\tilde{p}(\mathbf{r})\Big|_{\mathbf{r}\notin V_0} = 0, \qquad \tilde{p}_S(\mathbf{r}) = -\tilde{p}_V(\mathbf{r}), \quad \tilde{p}_M(\mathbf{r}) = \tilde{p}_D(\mathbf{r}) = -\tilde{p}_V(\mathbf{r})/2. \tag{13.30}$$

Hence, $\tilde{p}_S(\mathbf{r})$ is a discontinuous solution to Eq. (13.20) which is only valid outside the volume containing the sources (provided that the sign is reversed). If the volume is infinitely large, the Sommerfeld condition applies and the boundary integrals vanish so that $\tilde{p}(\mathbf{r}) = \tilde{p}_V(\mathbf{r})$ is a solution to Eq. (13.20) everywhere. In practice, however, the volume of integration only has to include all the sources under consideration, but not necessarily all the observation points. The usefulness of the boundary surface integral of Eq. (13.26) for solving acoustical problems cannot be overstated; it forms the basis for many numerical methods such as Boundary Element Modeling (or BEM). It is an embodiment of the Huygens–Fresnel principle discussed in Sec. 13.1. The surface of integration must be a closed one which fully encloses all the sources, although they may form part or all of the surface. By a closed surface, we could also mean an infinite plane which isolates the sources on one side of the plane (or within the plane itself) from the observation field on the other. Although $\tilde{p}_M(\mathbf{r})$ and $\tilde{p}_D(\mathbf{r})$ are both needed in the case of general surfaces, such as the spherical cap in a sphere in Sec. 13.5, we shall see that in the case of planar sources, one of the integrals can often be eliminated due to the symmetry of the problem. Before we apply the boundary integral to some problems of practical importance, we shall take a further look at the Green's function.

13.4 THE GREEN'S FUNCTION IN DIFFERENT COORDINATE SYSTEMS

13.4.1 Rectangular coordinates

Rectangular coordinates—near-field. The Green's function in rectangular coordinates was given by Eq. (13.4) as

$$g(x, y, z|x_0, y_0, z_0) = e^{-jkR}/(4\pi R), \tag{13.31}$$

where

$$R = \sqrt{(x - x_0)^2 + (y - y_0)^2 + (z - z_0)^2}. \tag{13.32}$$

However, problems are often encountered when using this expression because the space variables are all enclosed in a square-root sign and therefore cannot be separated. This makes finding analytical solutions very difficult and one often has to resort to using moveable-origin coordinate systems. This limits its use to numerical integration in the Kirchhoff–Helmholtz surface integral. Unfortunately, the Green's function of Eq. (13.31) is not particularly amenable to numerical integration, because it is singular at the origin and leads to oscillatory integrands at high frequencies. The dipole integral is even more problematic because the Green's function normal gradient has a $1/R^2$ term which leads to

diverging numerical and analytical integrals. Furthermore, where the surface of integration encloses one or more sources, we can only calculate the field on the side of the surface where there are no sources and the waves are diverging. In other words we cannot solve the *reverse* problem and calculate the field in which there are sources and the waves are converging. A more useful formula [4] is given by

$$g(x,y,z|x_0,y_0,z_0) = \frac{-j}{8\pi^2}\int_{-\infty}^{\infty}\int_{-\infty}^{\infty}\frac{e^{-j(k_x(x-x_0)+k_y(y-y_0)+k_z|z-z_0|)}}{k_z}dk_xdk_y \tag{13.33}$$

where

$$k_z = \begin{cases} \sqrt{k^2-k_x^2-k_y^2}, & k_x^2+k_y^2 \le k^2 \\ -j\sqrt{k_x^2+k_y^2-k^2}, & k_x^2+k_y^2 > k^2 \end{cases} \tag{13.34}$$

where k_x, k_y, and k_z represent the spatial frequency components in the x, y, and z directions respectively of a plane wave of spatial frequency k traveling in an arbitrary direction. For example, if the direction of travel subtends an angle θ with the z-axis, then the trace velocity seen along the z-axis is $c/\cos\theta$ and the wave-number is $k_z = k\cos\theta$. Hence the wavelength will appear to be longer along the z-axis. In order to gain a better understanding of Eq. (13.33) we may compare it with Eq. (7.113) for the pressure field inside an enclosure by letting $k_x = m\pi/l_x$, $k_y = n\pi/l_y$, and $k_z = k_{mn}$. We also replace the infinite integrals with summations. In other words, Eq. (13.33) may be thought of as the spatial distribution of an infinite enclosure in which traveling plane waves of any wavelength may exist as opposed to standing ones of particular wavelengths that correspond to the dimensions of the finite enclosure. The fact that a point source can be represented as integral over all spatial frequencies is not so surprising when we consider that an infinite impulse contains all frequencies.

It may seem counterintuitive to introduce two extra integrals, but the troublesome $1/R$ term has vanished along with the square-root sign in the exponent. When used in the Kirchhoff–Helmholtz integrals, we will show in Sec. 13.20 that this integral form of the Green's function is an inverse Fourier transform. This leads to an important theorem that forms the basis of near-field acoustical holography in which the dipole Kirchhoff–Helmholtz integral evaluated over one plane is the Fourier transform of the pressure distribution in that plane. The sound field spectra is then propagated in k-space to another parallel plane in which the Green's function is the inverse Fourier transform that gives the pressure in that plane. Furthermore, we can solve the so-called reverse problem where there are one or more sources in the field of interest. This method of calculation is particularly amenable to the digital processing of sound fields captured by planar microphone arrays in order to calculate the entire sound field of interest. In other words, if there are sources on one side of the array, we can plot the pressure field on *both* sides of the array. This is not possible using the non-integral form of the Green's function of Eq. (13.31).

Proof of the integral Green's function in rectangular coordinates. In order to derive the integral Green's function, we shall apply a triple Fourier transform, one for each Cartesian ordinate, to the Green's function in the spatial domain in order to convert it to the spatial frequency domain or k-space.

$$G(k_x,k_y,k_z) = \int_{-\infty}^{\infty}\int_{-\infty}^{\infty}\int_{-\infty}^{\infty} g(x,y,z|x_0,y_0,z_0)e^{j(k_xx+k_yy+k_zz)}dxdydz, \tag{13.35}$$

where $G(k_x, k_y, k_z)$ is the Fourier transform of $g(x, y, z|x_0, y_0, z_0)$. The inverse transform is

$$g(x,y,z|x_0,y_0,z_0) = \frac{1}{8\pi^3}\int_{-\infty}^{\infty}\int_{-\infty}^{\infty}\int_{-\infty}^{\infty} G(k_x,k_y,k_z)e^{-j(k_xx+k_yy+k_zz)}dk_xdk_ydk_z, \tag{13.36}$$

In order to solve for $G(k_x, k_y, k_z)$, we take the Fourier transform of Eq. (13.17)

$$\begin{aligned}&\int_{-\infty}^{\infty}\int_{-\infty}^{\infty}\int_{-\infty}^{\infty}(\nabla^2+k^2)g(x,y,z|x_0,y_0,z_0)e^{j(k_xx+k_yy+k_zz)}dxdydz\\ &= -\int_{-\infty}^{\infty}\int_{-\infty}^{\infty}\int_{-\infty}^{\infty}\delta(x-x_0)\delta(y-y_0)\delta(z-z_0)e^{j(k_xx+k_yy+k_zz)}dxdydz,\end{aligned} \tag{13.37}$$

where

$$\nabla^2 = \frac{\partial^2}{\partial x^2}+\frac{\partial^2}{\partial y^2}+\frac{\partial^2}{\partial z^2}, \tag{13.38}$$

Using the general property of the Dirac delta function from Eq. (154) of Appendix II and noting that

$$\nabla^2 e^{-j(k_xx+k_yy+k_zz)} = (-k_x^2-k_y^2-k_z^2)e^{-j(k_xx+k_yy+k_zz)}$$

yields

$$\begin{aligned}&(k^2-k_x^2-k_y^2-k_z^2)\int_{-\infty}^{\infty}\int_{-\infty}^{\infty}\int_{-\infty}^{\infty} g(x,y,z|x_0,y_0,z_0)e^{j(k_xx+k_yy+k_zz)}dxdydz\\ &= -e^{jk(k_xx_0+k_yy_0+k_zz_0)},\end{aligned} \tag{13.39}$$

which after substituting in Eq. (13.35) gives us the Green's function in k-space:

$$G(k_x,k_y,k_z) = \frac{e^{j(k_xx_0+k_yy_0+k_zz_0)}}{k_x^2+k_y^2+k_z^2-k^2}. \tag{13.40}$$

Applying the inverse Fourier transform of Eq. (13.36) then gives us an integral Green's function in terms of k-parameters:

$$\begin{aligned}g(x,y,z|x_0,y_0,z_0) &= \frac{1}{8\pi^3}\int_{-\infty}^{\infty}\int_{-\infty}^{\infty}\int_{-\infty}^{\infty}\frac{e^{-j\left(k_x(x-x_0)+k_y(y-y_0)+k_z(z-z_0)\right)}}{k_x^2+k_y^2+k_z^2-k^2}dk_xdk_ydk_z\\ &= \frac{1}{8\pi^3}\int_{-\infty}^{\infty}\int_{-\infty}^{\infty}\int_{-\infty}^{\infty}\frac{e^{-j\left(k_x(x-x_0)+k_y(y-y_0)+k_z(z-z_0)\right)}}{\left(k_z+\sqrt{k^2-k_x^2-k_y^2}\right)\left(k_z-\sqrt{k^2-k_x^2-k_y^2}\right)}dk_xdk_ydk_z,\end{aligned} \tag{13.41}$$

which has two poles: one at $k_z = +\sigma$ and the other at $k_z = -\sigma$, where

$$\sigma = \sqrt{k^2 - k_x^2 - k_y^2}.$$

We now convert Eq. (13.41) from a volume integral to a surface one by integrating over k_z using the *residue theorem*, which states that

$$\int_{-\infty}^{\infty} f(x)e^{-jxt}dx = \begin{cases} -2\pi j(\text{sum of residues of } f(x)e^{jxt} \text{ at all its poles } \alpha_i \\ \text{above the real axis,} \qquad t \geq 0 \\ 2\pi j(\text{sum of residues of } f(x)e^{jxt} \text{ at all its poles } \alpha_i \\ \text{on or below the real axis,} \qquad t < 0 \end{cases} \tag{13.42}$$

where each residue is defined by

$$(x - \alpha_i)f(x)e^{-jxt}\big|_{x\to\alpha_i}. \tag{13.43}$$

Applying this to Eq. (13.41) in order to solve the integral over k_z gives

$$g(x, y, z|x_0, y_0, z_0) = \\ = \frac{-j}{8\pi^2}\int_{-\infty}^{\infty}\int_{-\infty}^{\infty} \frac{e^{-j\left(k_x(x-x_0)+k_y(y-y_0)+\sigma|z-z_0|\right)}}{\sigma} dk_x dk_y. \tag{13.44}$$

If we let $k_z = \sigma$, this then gives us Eq. (13.33).

Rectangular coordinates—far-field. At a large distance R, Eq. (13.31) simplifies to

$$g(x, y, z|x_0, y_0, z_0)|_{R\to\infty} = \frac{e^{-jk(x(x-x_0)+y(y-y_0)+z(z-z_0))/R}}{4\pi R}, \tag{13.45}$$

where

$$R = \sqrt{x^2 + y^2 + z^2}. \tag{13.46}$$

13.4.2 Cylindrical coordinates

If we substitute

$$x = w\cos\phi, \qquad y = w\sin\phi, \qquad x_0 = w_0\cos\phi_0, \qquad y_0 = w_0\sin\phi_0 \tag{13.47}$$

in Eq. (13.31) and use

$$\sin\phi\,\sin\phi_0 + \cos\phi\,\cos\phi_0 = \cos(\phi - \phi_0),$$

we obtain

$$g(w, \phi, z|w_0, \phi_0, z_0) = e^{-jkR}/(4\pi R), \tag{13.48}$$

where

$$R = \sqrt{w^2 + w_0^2 - 2ww_0\cos(\phi - \phi_0) + (z - z_0)^2}. \tag{13.49}$$

However, this expression is of limited use and suffers from all the same drawbacks as were described in reference to the non-integral Green's function in rectangular coordinates given by Eq. (13.31). A much more powerful formula [4] is given by

$$g(w, \phi, z|w_0, \phi_0, z_0) = \frac{-j}{4\pi}\sum_{n=0}^{\infty}(2 - \delta_{n0})\cos n(\phi - \phi_0)\int_0^{\infty} J_n(k_w w)J_n(k_w w_0)\frac{e^{-jk_z|z-z_0|}}{k_z}k_w dk_w, \tag{13.50}$$

where

$$k_z = \begin{cases} \sqrt{k^2 - k_w^2}, & 0 \le k_w \le k \\ -j\sqrt{k_w^2 - k^2}, & k_w > k, \end{cases} \tag{13.51}$$

which is known as the Lamb–Sommerfeld integral [5,6]. This equation can be considered as the integral over all spatial frequencies of radial standing waves in an infinite cylinder, which are also summed over all azimuthal harmonics of order n. The component in the z direction is planar as represented by the exponent term. The reason why we have radial standing waves is that incoming waves pass through the z axis (or $w = 0$) before traveling back out again. In doing so, the imaginary part of the Hankel function, or Y_n function, changes sign. Thus the Y_n function is canceled leaving just the J_n function. This can be considered as the same phenomena as the incoming waves being reflected back from a rigid termination at $w = 0$. Hence the standing waves. In the case of axial symmetry, we exclude all azimuthal harmonics but the $n = 0$ term:

$$g(w, z|w_0, z_0) = \frac{-j}{4\pi}\int_0^{\infty} J_0(k_w w)J_0(k_w w_0)\frac{e^{-jk_z|z-z_0|}}{k_z}k_w dk_w. \tag{13.52}$$

We will apply this formula to problems with cylindrical symmetry such as circular sources.

Proof of the integral Green's function in cylindrical coordinates. If we substitute $x_0 = w_0\cos\phi_0$, $y_0 = w_0\sin\phi_0$, $x = w\cos\phi$, $y = w\sin\phi$, $k_x = k_w\cos\varphi$, and $k_y = k_w\sin\varphi$ in Eq. (13.33) and use the identity of Eq. (46) in Appendix II, we obtain

$$g(w, \phi, z|w_0, \phi_0, z_0) = \frac{-j}{8\pi^2}\int_0^{2\pi}\int_0^{\infty} e^{-jk_w(w\cos(\varphi-\phi) - w_0\cos(\varphi-\phi_0))}\frac{e^{-j\sqrt{k^2-k_w^2}|z-z_0|}}{\sqrt{k^2 - k_w^2}}k_w dk_w d\varphi \tag{13.53}$$

We then expand the first exponent term using Eq. (110) of Appendix II to give

$$g(w,\phi,z|w_0,\phi_0,z_0) = \frac{-j}{8\pi^2}\sum_{m=0}^{\infty}\sum_{n=0}^{\infty}(2-\delta_{m0})(2-\delta_{n0})j^{m-n} \times \int_0^{2\pi}\int_0^{\infty}\cos m(\varphi-\phi_0)\cos n(\varphi-\phi)J_m(k_w w_0)J_n(k_w w)\frac{e^{-j\sqrt{k^2-k_w^2}|z-z_0|}}{\sqrt{k^2-k_w^2}}k_w dk_w d\varphi \tag{13.54}$$

where the angular integral over φ is solved using

$$\int_0^{2\pi}\cos m(\varphi-\phi_0)\cos n(\varphi-\phi)d\varphi = \begin{cases}\dfrac{2\pi\cos n(\phi-\phi_0)}{2-\delta_{n0}}, & m=n\\ 0, & m\neq n\end{cases} \tag{13.55}$$

so that the double expansion of Eq. (13.54) reduces to the single one of Eq. (13.50).

13.4.3 Spherical coordinates

The Green's function in rectangular coordinates was given by Eq. (13.4):

$$g(x,y,z|x_0,y_0,z_0) = e^{-jkR}/(4\pi R), \tag{13.56}$$

where

$$R = \sqrt{(x-x_0)^2+(y-y_0)^2+(z-z_0)^2}. \tag{13.57}$$

If we substitute

$$\begin{aligned} x &= r\sin\theta\cos\phi, & y &= r\sin\theta\sin\phi, & z &= r\cos\theta\\ x_0 &= r_0\sin\theta_0\cos\phi_0, & y_0 &= r_0\sin\theta_0\sin\phi_0, & z_0 &= r_0\cos\theta_0 \end{aligned} \tag{13.58}$$

and use

$$\sin\phi\sin\phi_0+\cos\phi\cos\phi_0 = \cos(\phi-\phi_0),$$

we obtain

$$g(r,\theta,\phi|r_0,\theta_0,\phi_0) = e^{-jkR}/(4\pi R), \tag{13.59}$$

where

$$R = \sqrt{r^2+r_0^2-2rr_0(\sin\theta\sin\theta_0\cos(\phi-\phi_0)+\cos\theta\cos\theta_0)}. \tag{13.60}$$

However, as in the cylindrical and rectangular cases, this expression is of limited use and suffers from all the same drawbacks as were described in reference to the non-integral Green's

function in rectangular coordinates given by Eq. (13.31). A much more powerful formula [7] is given by

$$g(r,\theta,\phi|r_0,\theta_0,\phi_0) = \frac{-jk}{4\pi}\sum_{n=0}^{\infty}(2n+1)\sum_{m=0}^{n}(2-\delta_{m0})\frac{(n-m)!}{(n+m)!}\cos m(\phi-\phi_0) \times P_n^m(\cos\theta_0)P_n^m(\cos\theta)\begin{cases} j_n(kr_0)h_n^{(2)}(kr), & r>r_0 \\ j_n(kr)h_n^{(2)}(kr_0), & r<r_0. \end{cases} \tag{13.61}$$

In the case of axial symmetry, we exclude all terms from the summation in m except for the $m=0$ term:

$$g(r,\theta|r_0,\theta_0) = \frac{-jk}{4\pi}\sum_{n=0}^{\infty}(2n+1)P_n(\cos\theta_0)P_n(\cos\theta)\begin{cases} j_n(kr_0)h_n^{(2)}(kr), & r>r_0 \\ j_n(kr)h_n^{(2)}(kr_0), & r<r_0. \end{cases} \tag{13.62}$$

By relocating the source to $\theta_0=\pi$, $r_0\to\infty$, we obtain the expansion for a plane wave:

$$e^{-jkr\cos\theta} = \sum_{n=0}^{\infty}(-j)^n(2n+1)j_n(kr)P_n(\cos\theta). \tag{13.63}$$

It should be noted, however, that while this expansion form of the Green's function has certain analytical and numerical advantages, it cannot be applied to solving reverse problems.

13.4.4 Spherical-cylindrical coordinates

Spherical-cylindrical coordinates—near-field. If we substitute

$$x = r\sin\theta\cos\phi, \quad y = r\sin\theta\sin\phi, \quad z = r\cos\theta, \quad x_0 = w_0\cos\phi_0, \quad y_0 = w_0\sin\phi_0 \tag{13.64}$$

in Eq. (13.31) and use

$$\sin\phi\sin\phi_0+\cos\phi\cos\phi_0 = \cos(\phi-\phi_0),$$

we obtain

$$g(r,\theta|w_0,\phi_0) = e^{-jkR}/(4\pi R), \tag{13.65}$$

where

$$R^2 = r^2+w_0^2+z_0^2-2r(w_0\sin\theta\cos(\phi-\phi_0)+z_0\cos\theta). \tag{13.66}$$

If we set $z_0=0$ and $\phi=0$, this simplifies to

$$R^2 = r^2+w_0^2-2rw_0\sin\theta\cos\phi_0. \tag{13.67}$$

Again, this expression is of limited use, and a more powerful formula [8] is given by

$$g(r,\theta|w_0,\phi_0) = \begin{cases} \dfrac{-jk}{4\pi}\displaystyle\sum_{n=0}^{\infty}(2n+1)h_n^{(2)}(kr)j_n(kw_0)P_n(\sin\theta\cos\phi_0), & w_0 \le r \\ \dfrac{-jk}{4\pi}\displaystyle\sum_{n=0}^{\infty}(2n+1)j_n(kr)h_n^{(2)}(kw_0)P_n(\sin\theta\cos\phi_0), & w_0 \ge r, \end{cases} \tag{13.68}$$

which is a modified form of the Gegenbauer addition theorem or multipole expansion. We shall use it to derive near-field expressions for axisymmetric planar sources.

Spherical-cylindrical coordinates—far-field. At a large distance r, the terms containing r in Eq. (13.66) dominate. Hence the remaining terms can be replaced with ones that enable R to be factorized as follows:

$$\begin{aligned} R^2 &= r^2 - 2r(w_0\sin\theta\cos(\phi-\phi_0) + z_0\cos\theta) + w_0^2 + z_0^2 \\ &\approx r^2 - 2r(w_0\sin\theta\cos(\phi-\phi_0) + z_0\cos\theta) \\ &\quad +(w_0\sin\theta\cos(\phi-\phi_0) + z_0\cos\theta)^2 \\ &= (r - w_0\sin\theta\cos(\phi-\phi_0) - z_0\cos\theta)^2. \end{aligned} \tag{13.69}$$

Thus we can write the far-field Green's function as

$$g(r,\theta,\phi|w_0,\phi_0,z_0)|_{r\to\infty} = \frac{e^{-jk(r-w_0\sin\theta\cos(\phi-\phi_0)-z_0\cos\theta)}}{4\pi r}. \tag{13.70}$$

We will use this formula to derive far-field expressions for axisymmetric planar sources.

13.5 BOUNDARY INTEGRAL METHOD CASE STUDY: RADIALLY PULSATING CAP IN A RIGID SPHERE

In this section, we shall apply the boundary integral method to a pulsating cap in a sphere in order to illustrate its application to an elementary acoustical problem which has already been treated in Sec. 12.6 using the boundary value method. The geometry of the problem is shown in Fig. 12.16. From Eq. (13.26), we can write the pressure field as a surface integral:

$$\begin{aligned} \tilde{p}(r,\theta) = &\int_0^{2\pi}\int_0^{\pi} g(r,\theta|r_0,\theta_0)|_{r_0=R}\frac{\partial}{\partial r_0}\tilde{p}(r_0,\theta_0)\Big|_{r_0=R}R^2\sin\theta_0 d\theta_0 d\phi_0 \\ &-\int_0^{2\pi}\int_0^{\pi}\tilde{p}(r_0,\theta_0)\Big|_{r_0=R}\frac{\partial}{\partial r_0}g(r,\theta|r_0,\theta_0)|_{r_0=R}R^2\sin\theta_0\, d\theta_0 d\phi_0, \end{aligned} \tag{13.71}$$

where the Green's function in axisymmetric spherical coordinates is given from Eq. (13.62) by

$$g(r,\theta|r_0,\theta_0)|_{r_0=R} = \frac{-jk}{4\pi}\sum_{n=0}^{\infty}(2n+1)P_n(\cos\theta_0)P_n(\cos\theta)j_n(kR)h_n^{(2)}(kr), \tag{13.72}$$

and its normal gradient is given by

$$\frac{\partial}{\partial r_0}g(r,\theta|r_0,\theta_0)|_{r_0=R} = \frac{-jk}{4\pi}\sum_{n=0}^{\infty}(2n+1)P_n(\cos\theta_0)P_n(\cos\theta)j_n'(kR)h_n^{(2)}(kr), \tag{13.73}$$

where the derivative of the spherical Bessel function is given by Eq. (12.31). We see from Eq. (13.71) that we have a superposition of two fields. The first integral (monopole) represents the incident sound field due to the velocity source, formed by the cap. The normal pressure gradient, or velocity distribution, is obtained from the boundary conditions at the surface of the sphere:

$$\frac{\partial}{\partial r_0}\tilde{p}(r_0,\theta_0)\Big|_{r_0=R} = \begin{cases} -jk\rho_0 c\tilde{u}_0, & 0\le\theta\le\alpha \\ 0, & \alpha<\theta\le\pi. \end{cases} \tag{13.74}$$

The second integral (dipole) represents the sound field reflected by the sphere. The surface pressure distribution, which is a function of θ_0, is not yet known and is thus represented as a Legendre series:

$$\tilde{p}(r_0,\theta_0)\Big|_{r_0=R} = \rho_0 c\tilde{u}_0\sum_{m=0}^{\infty}A_m P_m(\cos\theta_0), \tag{13.75}$$

where the unknown coefficients A_m have to be determined. Inserting Eqs. (13.72), (13.73), (13.74), and (13.75) into Eq. (13.71) yields

$$\begin{aligned}\tilde{p}(r,\theta) = {} & -k^2R^2\rho_0 c\tilde{u}_0\sum_{n=0}^{\infty}\left(n+\frac{1}{2}\right)P_n(\cos\theta)j_n(kR)h_n^{(2)}(kr)\int_0^{\alpha}P_n(\cos\theta_0)\sin\theta_0 d\theta_0 \\ & + jkR^2\rho_0 c\tilde{u}_0\sum_{n=0}^{\infty}\left(n+\frac{1}{2}\right)P_n(\cos\theta)j_n'(kR)h_n^{(2)}(kr)\sum_{m=0}^{\infty}A_m\int_0^{\pi}P_m(\cos\theta_0)P_n(\cos\theta_0)\sin\theta_0 d\theta_0,\end{aligned} \tag{13.76}$$

where the integrals can be solved using the identities of Eqs. (66) and (69) from Appendix II to give

$$\tilde{p}(r,\theta) = kR^2\rho_0 c\tilde{u}_0\sum_{n=0}^{\infty}P_n(\cos\theta)h_n^{(2)}(kr)\left(jA_n j_n'(kr) - k\left(n+\frac{1}{2}\right)j_n(kR)\sin\alpha\, P_n^{-1}(\cos\alpha)\right). \tag{13.77}$$

In order to solve for the unknown coefficients A_n, we apply the following boundary condition to the above pressure field:

$$\frac{\partial}{\partial r}\tilde{p}(r,\theta)\Big|_{r=R} = -jk\rho_0 c\tilde{u}(R,\theta) = \begin{cases} -j\rho_0 c\tilde{u}_0, & 0 \le \theta \le \alpha \\ 0, & \alpha < \theta \le \pi. \end{cases} \tag{13.78}$$

The surface velocity can be represented by the following Legendre series:

$$\tilde{u}(R,\theta) = \tilde{u}_0 \sum_{n=0}^{\infty} B_n P_n(\cos\theta), \tag{13.79}$$

where the coefficients B_n are found by multiplying through by the orthogonal function $P_m(\cos\theta)$ and integrating over the surface as follows:

$$\int_0^{\alpha} P_n(\cos\theta)\sin\theta\, d\theta = \sum_{n=0}^{\infty} B_n \int_0^{\pi} P_m(\cos\theta)P_n(\cos\theta)\sin\theta\, d\theta \tag{13.80}$$

and applying the identities of Eqs. (66) and (69) from Appendix II to yield

$$B_n = \left(n+\frac{1}{2}\right)\sin\alpha\, P_n^{-1}(\cos\alpha). \tag{13.81}$$

The coefficients are finally solved by applying Eq. (13.78) to Eq. (13.77) and equating the coefficients of $P_n(\cos\theta)$ to give

$$A_n = -\left(n+\frac{1}{2}\right)\sin\alpha\, P_n^{-1}(\cos\alpha)\frac{1+jkR^2 j_n(kR)h_n'^{(2)}(kR)}{R^2 j_n'(kR)h_n'^{(2)}(kR)}, \tag{13.82}$$

which, after inserting into Eq. (13.77), gives

$$\tilde{p}(r,\theta) = -jk\rho_0 c\tilde{u}_0 \sum_{n=0}^{\infty}\left(n+\frac{1}{2}\right)\sin\alpha\, P_n^{-1}(\cos\alpha)P_n(\cos\theta)\frac{h_n^{(2)}(kr)}{h_n'^{(2)}(kR)}. \tag{13.83}$$

This is exactly the same equation as would be obtained using the boundary value method described in Sec. 12.6. In the far field, applying the asymptotic expression for the spherical Hankel function from Eq. (12.18) gives

$$\tilde{p}(r,\theta) = -jk\rho_0 cS\frac{\tilde{u}_0}{4\pi r}e^{-jkr}D(\theta), \tag{13.84}$$

where the directivity function is given by

$$D(\theta) = \frac{\sin\alpha}{2k^2R^2\sin^2(\alpha/2)}\sum_{n=0}^{\infty}\frac{j^{n+1}(2n+1)^2 P_n^{-1}(\cos\alpha)P_n(\cos\theta)}{nh_{n-1}^{(2)}(kR)-(n+1)h_{n+1}^{(2)}(kR)} \tag{13.85}$$

and $S = 4\pi R^2 \sin^2 \alpha/2$. The radiation impedance is given by

$$\begin{aligned} Z_s &= \frac{\tilde{F}}{\tilde{U}_0} = \frac{2\pi R^2}{S\tilde{u}_0} \int_0^{\alpha} \tilde{p}(r,\theta)\sin\theta \, d\theta \\ &= -j\rho_0 c \frac{\sin^2\alpha}{\sin^2(\alpha/2)} \sum_{n=0}^{\infty} \frac{\left(n+\frac{1}{2}\right)^2 \left(P_n^{-1}(\cos\alpha)\right)^2 h_n^{(2)}(kR)}{nh_{n-1}^{(2)}(kR) - (n+1)h_{n+1}^{(2)}(kR)}. \end{aligned} \tag{13.86}$$

13.6 REFLECTION OF A POINT SOURCE FROM A PLANE

Here we consider what happens when a point source is placed near an infinite reflective planar boundary. Essentially, a hard reflecting surface is the acoustic equivalent to a mirror in optics whereby each reflecting element on its surface acts as a light source. A mirror can be regarded as a perfect hologram because it produces an intensity that varies with direction in accordance with the law of reflection. That is, the angle of reflection is equal to the angle of incidence. Hence, when you walk past a mirror, the view changes, whereas when you walk past a picture or video screen, it does not. This is because the latter provides only intensity information and no directional information. The directional information comes from the *phase* of each point source on the surface. For analytical purposes, it is often convenient to replace the reflecting plane with a transparent plane of symmetry which has a symmetrically identical source behind it as shown in Fig. 13.2.

This property of symmetry has already been applied in previous examples such as the domes in Secs. 12.9 and 12.10. The source and its image both have the same perpendicular distance d from the plane. With the image source present, the pressure fields with and without the reflecting plane can be shown to be identical if we consider that in both cases the field is symmetrical either side of the plane. Therefore, the pressures must be equal on opposite faces of the plane, in which case the pressure gradient in the plane must be zero. Since it takes a pressure gradient to generate a particle velocity, this also satisfies the boundary condition of zero particle velocity normal to the plane. Of course, there is no physical image source, so this model is only valid on the source side of the surface.

The principle can be expressed by the superposition of fields as follows. If the point source is located at a distance z_0 from an infinite screen at $z = 0$, there will be an extra field superimposed upon the original due to a virtual source behind the screen. Using Eqs. (13.2), (13.31), (13.48), and (13.49) for a point source, the field $\tilde{p}_S(w,\phi,z)$ produced by the source in cylindrical coordinates is given by

$$\tilde{p}_S(w,\phi,z) = -jk\rho_0 c\tilde{U}_S \frac{e^{-jkR_S}}{4\pi R_S}, \tag{13.87}$$

where

$$R_S = \sqrt{w^2 + w_0^2 - 2ww_0\cos(\phi-\phi_0) + (z+z_0)^2}. \tag{13.88}$$

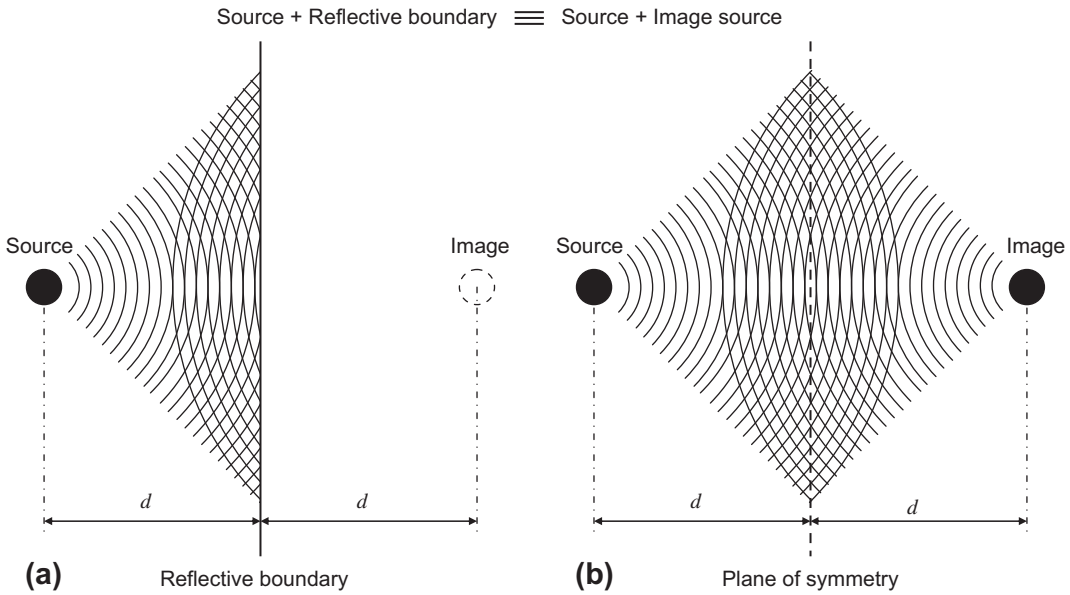

FIG. 13.2 Reflection of a point source from (*a*) a plane and (*b*) equivalent source and image.

The field $\tilde{p}_I(w, \phi, z)$ produced by the image is then

$$\tilde{p}_I(w, \phi, z) = -jk\rho_0 c\tilde{U}_S \frac{e^{-jkR_I}}{4\pi R_I}, \tag{13.89}$$

where

$$R_I = \sqrt{w^2 + w_0^2 - 2ww_0 \cos(\phi - \phi_0) + (z - z_0)^2}, \tag{13.90}$$

which produces a resultant field

$$\begin{aligned} \tilde{p}(w, \phi, z) &= \tilde{p}_S(w, \phi, z) + \tilde{p}_I(w, \phi, z) \\ &= -jk\rho_0 c\tilde{U}_S \left(\frac{e^{-jkR_S}}{4\pi R_S} + \frac{e^{-ikR_I}}{4\pi R_I} \right). \end{aligned} \tag{13.91}$$

Let us now recast this equation in the form

$$\tilde{p}(w, \phi, z) = -jk\rho_0 c\tilde{U}_S G(w, \phi, z|w_0, \phi_0, z_0), \tag{13.92}$$

where

$$G(w, \phi, z|w_0, \phi_0, z_0) = \frac{e^{-jkR_S}}{4\pi R_S} + \frac{e^{-ikR_I}}{4\pi R_I} \tag{13.93}$$

is a *bounded* Green's function. Notice that we use the upper case G. An interesting feature of this bounded Green's function is that its normal derivative with respect to the plane (i.e., with respect to z) is zero. Now suppose that part of the plane is in motion and radiating sound. Points on the plane can be represented by G if we let $z_0 \to 0$ so that the source and its image coalesce. Hence

$$G(w, \phi, z|w_0, \phi_0, 0) = \frac{e^{-jkR}}{2\pi R} = 2g(w, \phi, z|w_0, \phi_0, 0), \tag{13.94}$$

where

$$R = \sqrt{w^2 + w_0^2 - 2ww_0 \cos(\phi - \phi_0) + z^2}. \tag{13.95}$$

We can use this Green's function in the monopole Rayleigh integral to represent a planar source in an infinite baffle. Because the normal derivative of G is zero, the dipole Rayleigh integral vanishes and the point sources on the surface become monopole point sources of double strength.

PART XXXVI: RADIATION AND SCATTERING IN CYLINDRICAL-SPHERICAL COORDINATES

13.7 RADIATION FROM A RIGID CIRCULAR PISTON IN AN INFINITE BAFFLE

The simplest monopole planar source is the oscillating circular piston (or rigid disk) in an infinite baffle. The piston is assumed to be rigid so that all parts of its surface vibrate in phase and its velocity amplitude is independent of the mechanical or acoustic loading on its radiating surface. Remarkably, its radiation impedance was first derived by Rayleigh [9] before the direct radiator loudspeaker had even been invented [10], yet it has been widely accepted as an idealized model for such when mounted in an enclosure situated near a wall or, even better, mounted directly in a wall as commonly found in recording studios. The model is useful in the frequency range up to the first diaphragm break-up mode. It should be noted that here the term "infinite baffle" refers to an infinitely large plane rigid wall that surrounds the piston and not a finite sealed enclosure which is often referred to as an infinite baffle enclosure. The only thing they have in common is that they both block the transmission path between the back and the front of the radiating surface. However, the infinitely large wall model does not take into account reflections from the edges of a real finite enclosure. Also both sides of the radiating surface are open to half space so that the loading effects of a real finite enclosure such as compliance, standing waves, absorption, and wall vibration, etc. are ignored. The original derivation of the radiation impedance by Rayleigh over 100 years ago used the non-integral Green's function of Eq. (13.16) with an ingenious coordinate system. Here we shall follow the approach of King [11] using the integral Green's function in cylindrical coordinates given by Eq. (13.52).

Boundary conditions. The circular piston of radius a shown in Fig. 13.3 is mounted in an infinite baffle in the xy plane with its center at the origin and oscillates in the z direction with a harmonically

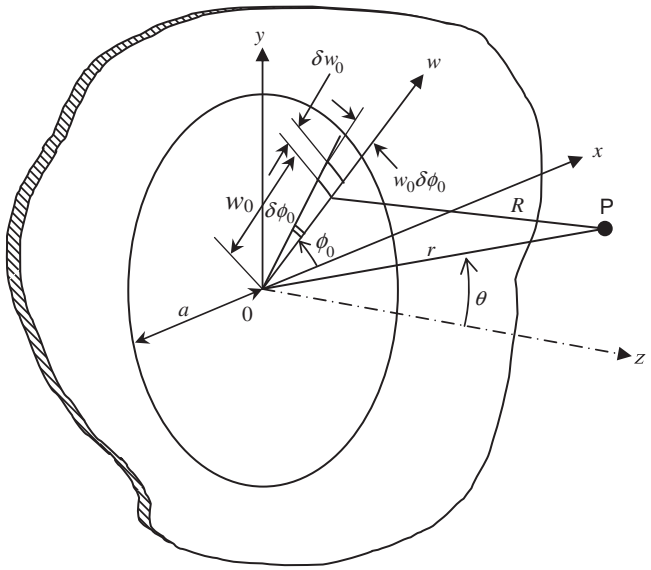

FIG. 13.3 Geometry of rigid circular piston in infinite baffle.

The point of observation P is located at a distance r and angle θ with respect to the origin at the center of the piston.

time dependent velocity $\tilde{u}_0$, thus radiating sound into a homogeneous loss-free medium. The area of each surface element is given by

$$\delta S_0 = w_0 \delta w_0 \delta\phi_0. \tag{13.96}$$

The monopole source elements shown in Fig. 13.4, together with their images, form the piston source. Since they are coincident in the plane of the baffle, they coalesce to form elements of double strength. Hence the piston in an infinite baffle can be modeled as a "breathing" disk in free space. It may also be considered as a pulsating sphere of the same radius compressed into the plane of the disk. Due to the symmetry of the pressure fields on either side of the baffle,

$$\tilde{p}(w, z) = \tilde{p}(w, -z). \tag{13.97}$$

Consequently, there is the following Neumann boundary condition on its surface:

$$\frac{\partial}{\partial z}\tilde{p}(w, z)\Big|_{z=0+} = 0, \qquad a < w \leq \infty, \tag{13.98}$$

which is satisfied automatically. On the surface of the disk there is the coupling condition

$$\frac{\partial}{\partial z}\tilde{p}(w, z)\Big|_{z=0+} = -jk\rho_0 c\tilde{u}_0, \qquad 0 \leq w \leq a \tag{13.99}$$

and k is the wave-number given by $k = \omega/c = 2\pi/\lambda$, ω is the angular frequency of excitation, ρ_0 is the density of the surrounding medium, c is the speed of sound in that medium, and λ is the wavelength.

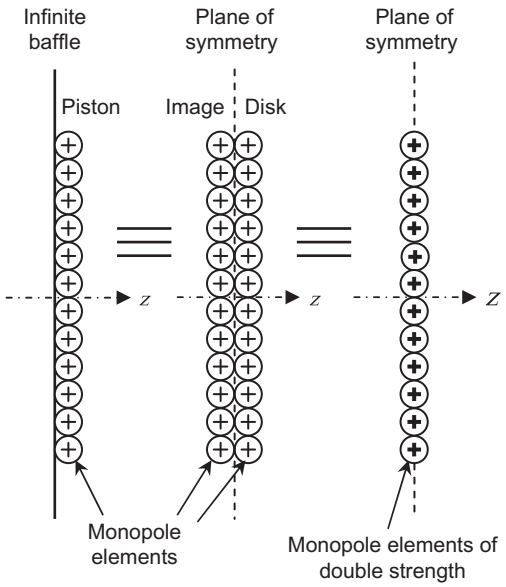

FIG. 13.4 Equivalence between circular piston in infinite baffle and double-sided monopole piston in free space or "breathing" disk in free space.

Far-field pressure. The far-field pressure distribution is given by Eq. (13.27) taking into account the double strength source:

$$\tilde{p}(r,\theta) = 2\int_0^{2\pi}\int_0^{a} g(r,\theta|w_0,\phi_0)\frac{\partial}{\partial z_0}\tilde{p}(w_0,z_0)\Big|_{z_0=0+} w_0 dw_0 d\phi_0, \tag{13.100}$$

where the far-field Green's function in spherical-cylindrical coordinates given by Eq. (13.70) is used. Inserting Eqs. (13.70) and (13.99) into Eq. (13.100) and integrating over the surface, using Eqs. (76) and (95) from Appendix II (with $z = kw_0 \sin\theta$, $b = k \sin\theta$, and letting $\phi = \pi/2$ so that $\cos(\phi - \phi_0) = \sin\phi_0$), gives

$$\tilde{p}(r,\theta) = -jka^2\rho_0 c\tilde{u}_0 \frac{e^{-jkr}}{2r} D(\theta), \tag{13.101}$$

where the directivity function $D(\theta)$ is given by

$$D(\theta) = \frac{2J_1(ka\sin\theta)}{ka\sin\theta}, \tag{13.102}$$

which is often referred to as the Fraunhofer or Airy diffraction pattern. The normalized directivity function $20\log_{10}|D(\theta)|$ is plotted in Fig. 13.5 for four values of $ka = 2\pi a/\lambda$, that is, for four values of the ratio of the circumference of the piston to the wavelength. When the circumference of the piston ($2\pi a$) is less than one-half wavelength, that is, $ka < 0.5$, the piston behaves essentially like a point source. When ka becomes greater than 3, the piston is highly directional.

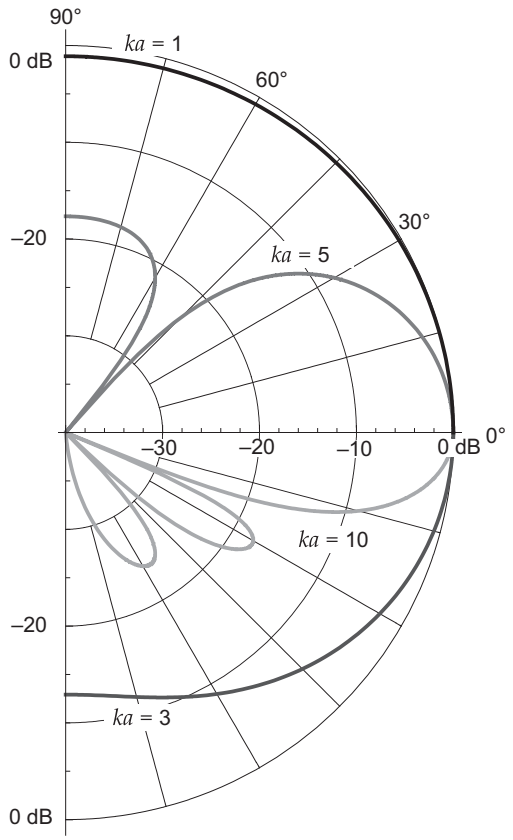

FIG. 13.5 Far-field directivity patterns for a rigid circular piston in an infinite baffle as a function of $ka = 2\pi a/\lambda = \omega/c$, where a is the radius of the piston.

The directivity index never becomes less than 3 dB, because the piston radiates only into half space.

The on-axis pressure is evaluated by setting $\theta = 0$ in Eq. (13.70) before inserting it in Eq. (13.100) and integrating over the surface to give

$$D(0) = 1 \tag{13.103}$$

which means that the on-axis far-field pressure is proportional to the piston *acceleration* at all frequencies and is often written

$$\tilde{p}(r,0) = -j\rho_0 f \tilde{U}_0 \frac{e^{-jkr}}{r}, \tag{13.104}$$

where $\tilde{U}_0 = \pi a^2 \tilde{u}_0$ is the total volume velocity. This is a general expression for a planar source in an infinite baffle and also applies to non-uniform velocity distributions where the volume velocity is the product of the average velocity and the radiating area, which can be of arbitrary shape.

Although the piston behaves as a more or less omnidirectional source for $ka \leq 1$, similar to a pulsating sphere, the output of the piston is 6 dB less than that of the pulsating sphere at very low frequencies. Because the piston is radiating into half space, its output per unit surface area is double that of the pulsating sphere, which is radiating into whole space. However, the sphere has four times the surface area of a piston of the same radius. Therefore it produces twice the output. Unlike the pulsating sphere, the on-axis response of the piston does not roll-off at high frequencies, which is a property of planar sources in general, as already discussed in Sec. 12.8 regarding a piston in a sphere. Unlike the piston in a sphere, there is no 6 dB level shift between low and high frequencies because the baffled piston effectively radiates into half space at all frequencies. As we shall see, its radiation impedance, like that of a pulsating sphere, is dominated by mass reactance at low frequencies and resistance at high frequencies.

In the low-frequency region, the radiated sound pressure and hence also intensity are held constant under constant piston acceleration. This is because the decreasing velocity is compensated for by the rising radiation resistance, as discussed in greater detail in Sec. 4.10.

At higher frequencies, where the impedance starts to become more resistive, the beam pattern, coincidentally, becomes increasingly narrow. This phenomenon compensates for the fall in on-axis output that would otherwise occur. Indeed, in the case of the pulsating sphere, the radiated sound pressure is proportional to the surface velocity in the region where the load is resistive and therefore falls under constant acceleration and falling velocity. It seems a remarkable coincidence of nature that this transition occurs so smoothly as to produce a completely flat on-axis response, although it does not seem so surprising when we consider that the on-axis response results from the sum of an array of point sources that are all in phase, where the field of each point source is frequency invariant under constant volume acceleration.

Near-field pressure. The near-field pressure distribution is given by the boundary integral of Eq. (13.27) taking into account the double-strength source:

$$\tilde{p}(r,\theta) = 2\int_0^{2\pi}\int_0^{a} g(r,\theta|w_0,\phi_0)\frac{\partial}{\partial z_0}\tilde{p}(w_0,z_0)\Big|_{z_0=0+} w_0 dw_0 d\phi_0, \tag{13.105}$$

where the Green's function in spherical-cylindrical coordinates given by Eq. (13.68) is used. Mast and Yu [12] show that inserting Eqs. (13.68) and (13.99) into Eq. (13.105) and integrating over the surface gives

$$\begin{aligned}\tilde{p}(r,\theta) = {} & 2\rho_0 c\tilde{u}_0 \sum_{n=0}^{\infty} \frac{(-1)^n \Gamma\left(n+1/2\right)}{\Gamma(n+2)\Gamma\left(2n+1/2\right)}\left(\frac{ka}{2}\right)^{2n+2} \\ & \times {}_1F_2\left(n+1; n+2, 2n+\frac{3}{2}; \frac{k^2a^2}{4}\right) h_{2n}^{(2)}(kr) P_{2n}(\cos\theta)\end{aligned} \tag{13.106}$$

which converges for $r > a$ but is generally used for $w \geq a$. The other part of the Green's function of Eq. (13.68) could be used to derive an expression for $r < a$ as was done previously by Stenzel [13]. However, a better expression is provided by Mast and Yu, [12] which is derived by moving the origin

of the coordinate system to a point on the z axis that lies in the same plane as the observation point to give

$$\tilde{p}(w,z) = \frac{\rho_0 c\tilde{u}_0}{\sqrt{\pi}} \sum_{n=0}^{\infty} (-1)^n (4n+1) \frac{\Gamma\left(n+1/2\right)}{\Gamma(n+1)} j_{2n}(kw) f_{2n}, \tag{13.107}$$

where f_{2n} is given by the following recursion formulas:

$$f_0 = e^{-jkz} - e^{-jkr_a}, \tag{13.108}$$

$$f_{2n} = -f_{2n-2} - kr_a h_{2n-1}^{(2)}(kr_a)(P_{2n}(z/r_a) - P_{2n-2}(z/r_a)), \tag{13.109}$$

and

$$r_a = \sqrt{z^2 + a^2}, \tag{13.110}$$

which converges for $w^2 < a^2 + z^2$ but is generally used for $w < a$ and is thus termed the *paraxial* solution. These equations are an elegant and important result for ultrasound since they eliminate the need for inefficient numerical integration at high frequencies. In particular, the number of terms needed for convergence in the paraxial expansion decreases linearly towards the z-axis until just a single term remains. This is the closed-form axial solution:

$$\tilde{p}(0,z) = \rho_0 c\tilde{u}_0 (e^{-jkz} - e^{-jkr_a}). \tag{13.111}$$

The first term represents a point source at the center of the piston and the second term radiation from the rim. The magnitude of the axial pressure is $|\tilde{p}(0,z)| = 2\rho_0 c|\tilde{u}_0 \sin k(r_a - z)/2|$. Near the surface of the piston, it is approximately $|\tilde{p}(0,z)| \approx \rho_0 ck a|\tilde{u}_0|\,/(1 + z/a)$ for $ka < 0.5$ and $z < 0.5a$. Hence, at low frequencies, the radiated sound pressure of a loudspeaker may be calculated from the diaphragm velocity [see Eq. (13.101)], which in turn may be measured using a probe microphone close to the center. The pressure field for three values of ka is plotted in Fig. 13.6 and for $ka = 12\pi$ in Fig. 13.7. From these figures, we can see the formation of the central and side lobes of the directivity patterns at the start of the far-field or Fraunhofer diffraction zone, where the waves are spherically diverging. The near-field or Fresnel region is dominated by non-propagating interference patterns due to the differences in path lengths from different parts of the radiating surface. However, in the immediate near field of Fig. 13.7, the pressure fluctuations are relatively small and we see here the formation of a plane wave which extends outwards with increasing frequency. The furthest axial peak is a focal point, which is useful for ultrasound applications. Also, we can make the following observations.

1. At low frequencies, where $ka < 3$, the on-axis pressure of Eq. (13.111) converges to the far-field approximation of Eq. (13.104) at around $z = \pi a/2$.
2. At high frequencies, where $ka > 3$, the on-axis pressure converges to the far-field approximation at around $z = ka^2/2$ which is known as the Rayleigh distance [14,15]. The on-axis near-field pressure is oscillatory and there are $ka/(2\pi)$ or a/λ cycles before it converges to the far-field response, where one cycle spans two magnitude peaks or two nulls. The pressure on the face of the piston also oscillates radially with a total of $ka/2\pi$ or a/λ cycles between the center and rim. Furthermore, if $ka = n\pi$ or $n\lambda = 2a$, where n is an integer, the pressure at the center of the piston is at a null for even n and at a peak for odd n.

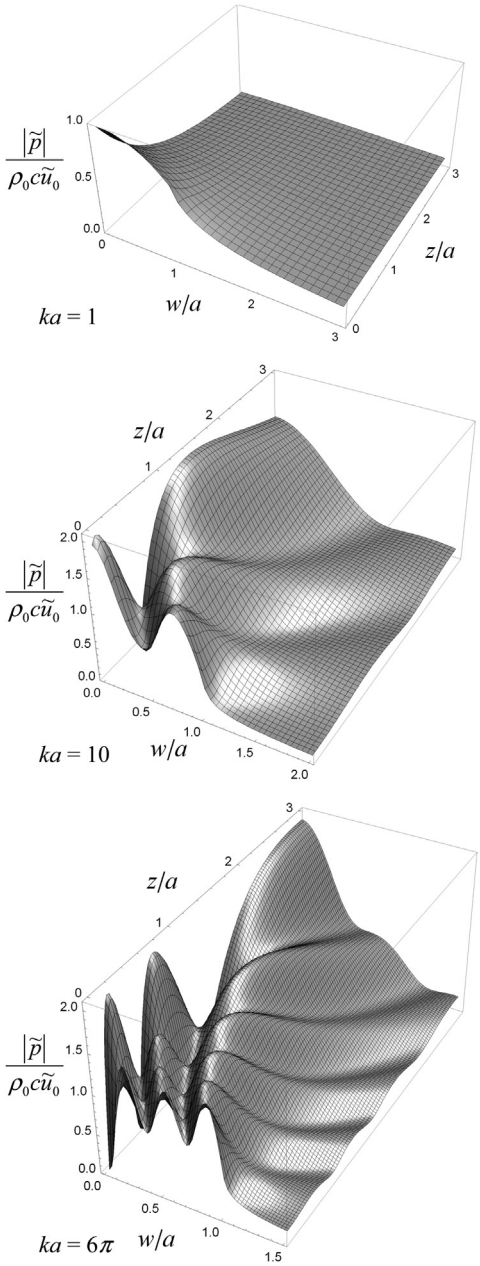

FIG. 13.6 Normalized near-field pressure plots for a rigid circular piston in an infinite baffle as a function of $ka = 2\pi a/\lambda = 2\pi fa/c$.

Where a is the radius of the piston, $|\tilde{p}|$ is the pressure magnitude, $\tilde{u}_0$ is the piston velocity, ρ_0 is the density of the acoustic medium, and c is the speed of sound in that medium.

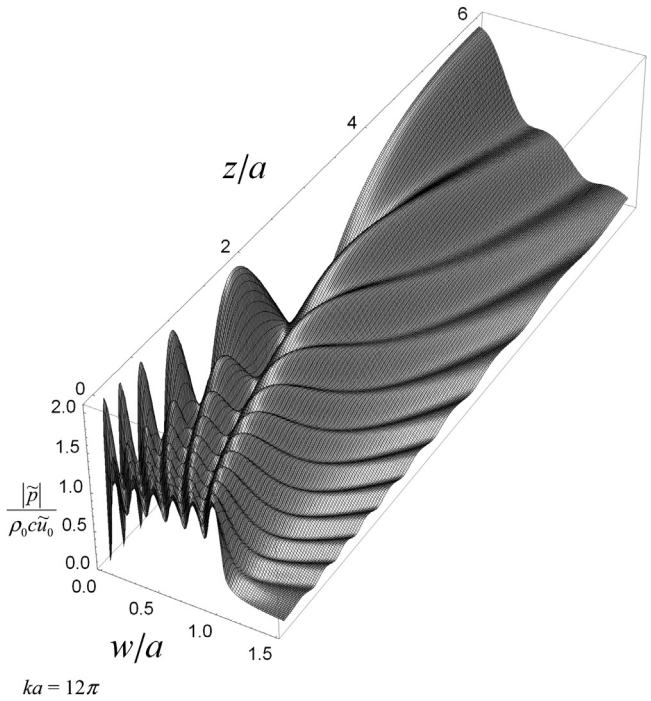

FIG. 13.7 Normalized near-field pressure plots for a rigid circular piston in an infinite baffle as a function of $ka = 2\pi a/\lambda = 2\pi fa/c$.

Where a is the radius of the piston, $|\tilde{p}|$ is the pressure magnitude, $\tilde{u}_0$ is the piston velocity, ρ_0 is the density of the acoustic medium, and c is the speed of sound in that medium.

3. The number of lobes in the directivity pattern corresponds to the number of axial peaks plus the number of peaks along the radius of the piston.

Radiation impedance and high-frequency asymptotic expression. The near-field pressure distribution is given by Eq. (13.27) taking into account the double-strength source:

$$\tilde{p}(w,z) = 2\int_0^{2\pi}\int_0^{a} g(w,z|w_0,z_0)\frac{\partial}{\partial z_0}\tilde{p}(w_0,z_0)\Big|_{z_0=0+} w_0 dw_0 d\phi_0, \tag{13.112}$$

where the Green's function in cylindrical coordinates given by Eq. (13.52) is used. In this form Eq. (13.112) is known as the monopole King integral [11]. Inserting Eqs. (13.52) and (13.99) into Eq. (13.112) and integrating over the surface gives

$$\tilde{p}(w,z) = -ka\rho_0 c\tilde{u}_0 \int_0^{\infty} J_0(k_w w)J_1(k_w a)\frac{1}{k_z}e^{-jk_z z}dk_w, \tag{13.113}$$

where we have used the integral solution of Eq. (95) from Appendix II and k_z is given by Eq. (13.51). In order to investigate the asymptotic high-frequency behavior, we let $k \to \infty$ in Eq. (13.113) to give

$$\begin{aligned}\tilde{p}(w,z)\Big|_{k\to\infty} &= -\rho_0 c\tilde{u}_0 e^{-jkz} a \int_0^\infty J_1(k_w a) J_0(k_w w) dk_w \\ &= \begin{cases} -\rho_0 c\tilde{u}_0 e^{-jkz}, & 0 \le w \le a \\ 0, & w > a. \end{cases}\end{aligned} \tag{13.114}$$

This slightly trivial solution describes the sound being radiated as a laser beam confined within the diameter of the piston. It can also be regarded as a virtual infinite tube or transmission line in space starting from the perimeter of the piston. At first sight, this may appear to contradict Eq. (13.111), because the axial nulls and peaks never actually disappear. On the contrary, they become more numerous and travel out further with increasing frequency. However, in the high frequency limit, the radial width of this range of hills and dales shrinks so much that they become insignificant.

The total radiation force is found by integrating the pressure from Eq. (13.113) over the surface of the piston and again using the integral of Eq. (95) from Appendix II to give

$$\begin{aligned}\tilde{F} &= -\int_0^{2\pi}\int_0^a \tilde{p}(w,z)\Big|_{z=0+} w dw d\phi \\ &= 2\pi k a^2 \rho_0 c\tilde{u}_0 \left(\int_0^k \frac{J_1^2(k_w a)}{k_w\sqrt{k^2 - k_w^2}} dk_w + j\int_k^\infty \frac{J_1^2(k_w a)}{k_w\sqrt{k_w^2 - k^2}} dk_w \right).\end{aligned} \tag{13.115}$$

King [11] shows the solution to be

$$Z_s = \frac{\tilde{F}}{\tilde{U}_0} = \boldsymbol{R}_s + jX_s, \tag{13.116}$$

where $\tilde{U}_0 = \pi a^2 \tilde{u}_0$ is the total volume velocity and $\boldsymbol{R}_s$ is the specific radiation resistance in $\mathrm{N\cdot s/m^3}$ (rayl) given by

$$\boldsymbol{R}_s = \rho_0 c\left(1 - \frac{J_1(2ka)}{ka}\right), \tag{13.117}$$

where the bold $\boldsymbol{R}$ indicates that the quantity varies with frequency. X_s is the specific radiation reactance in $\mathrm{N\cdot s/m^3}$ (rayl) given by

$$X_s = \rho_0 c\frac{\mathbf{H}_1(2ka)}{ka}, \tag{13.118}$$

where J_1 and $\mathbf{H}_1$ are Bessel and Struve functions respectively as defined by Eqs. (71) and (125) in Appendix II. Plots of the real and imaginary parts of

$$\frac{Z_s}{\rho_0 c} = \frac{\boldsymbol{R}_s + jX_s}{\rho_0 c} \tag{13.119}$$

are shown in Fig. 4.35 as a function of ka. Similar graphs of the real and imaginary parts of the specific admittance

$$Y_s\rho_0 c \;=\; \rho_0 c(\boldsymbol{G}_s + jB_s) \;=\; \rho_0 c\left(\frac{\boldsymbol{R}_s}{\boldsymbol{R}_s^2 + X_s^2} - j\frac{X_s}{\boldsymbol{R}_s^2 + X_s^2}\right) \tag{13.120}$$

are shown in Fig. 4.36. The specific admittance is in $\mathrm{m}^3\cdot\mathrm{N}^{-1}\cdot\mathrm{s}^{-1}$ (rayl^{-1}).

We see from Fig. 4.35 that, for $ka < 0.5$, the reactance varies as the first power of frequency while the resistance varies as the second power of frequency. At high frequencies, for $ka > 5$, the reactance becomes small compared with the resistance, and the resistance approaches a constant value.

The admittance, on the other hand, is better behaved. The conductance is constant for $ka < 0.5$, and it is also constant for $ka > 5$ although its value is larger.

13.8 RADIATION FROM A RESILIENT CIRCULAR DISK WITHOUT A BAFFLE [16]

The resilient circular disk in free space is the simplest dipole planar source and the dipole complement of the rigid circular piston in an infinite baffle. It can be used as an approximate model for unbaffled loudspeakers of the electrostatic or planar magnetic type, in which it is assumed that a perfectly uniform driving pressure is applied to a very light flexible membrane diaphragm in free space. Due to the dipole nature of the source, there is zero pressure in the plane of the disk extending beyond its rim. Walker [17] pointed out that such a source is acoustically transparent, in that it does not disturb the field around it, and used this idealized model to derive the far-field on-axis pressure response of an electrostatic loudspeaker, which provides a useful approximation over the loudspeaker's working range. However, it should be noted that the model assumes a freely suspended membrane, whereas in reality it is usually clamped at the rim, which effectively removes the singularity from the rim of the idealized model [18].

Boundary conditions. The basic configuration is shown in Fig. 13.8. The infinitesimally thin membrane-like resilient disk is assumed to be perfectly flexible, has zero mass, and is free at its perimeter. It is driven by a uniformly distributed harmonically varying pressure $\tilde{p}_0$ and thus radiates sound from both sides into a homogeneous loss-free acoustic medium. In fact, there need not be a disk present at all and instead the driving pressure could be acting upon the air particles directly. However, for expedience, the area over which this driving pressure is applied shall be referred to as a disk from here onwards. The pressure field on one side of the xy plane is the symmetrical "negative" of that on the other, so that

$$\tilde{p}(w, z) \;=\; -\tilde{p}(w, -z). \tag{13.121}$$

Consequently, there is a Dirichlet boundary condition in the plane of the disk where these equal and opposite fields meet.

$$\tilde{p}(w, 0) \;=\; 0, \qquad a < w \leq \infty\,. \tag{13.122}$$

On the front and rear surfaces of the disk, the pressures are $\tilde{p}_+$ and $\tilde{p}_-$ respectively, which are given by

$$\tilde{p}_+(w_0) \;=\; -\tilde{p}_-(w_0) \;=\; \tilde{p}_0/2, \qquad 0 \leq w_0 \leq a \tag{13.123}$$

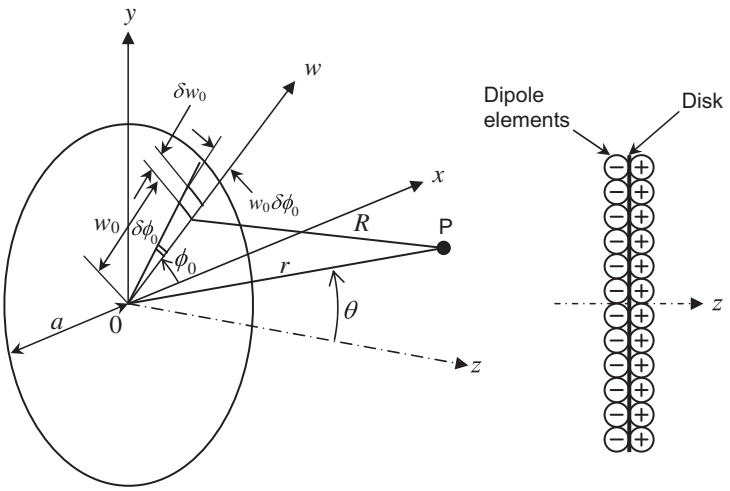

FIG. 13.8 Geometry of resilient circular disk in free space. The point of observation P is located at a distance *r* and angle θ with respect to the origin at the center of the disk.

and k is the wave-number given by $k = \omega/c = 2\pi/\lambda$, where ω is the angular frequency of excitation, ρ_0 is the density of the surrounding medium, c is the speed of sound in that medium, and λ is the wavelength.

Far-field pressure. The far-field pressure distribution is given by the dipole boundary integral of Eq. (13.28), taking into account the surface pressure on both sides:

$$\tilde{p}(r,\theta) = \int_0^{2\pi}\int_0^{a} (\tilde{p}_+(w_0) - \tilde{p}_-(w_0)) \frac{\partial}{\partial z_0} g(r,\theta|w_0,\phi_0)|_{z_0=0+} w_0 dw_0 d\phi_0, \tag{13.124}$$

where the far-field Green's function in spherical-cylindrical coordinates given by Eq. (13.70) is used. Inserting Eqs. (13.70), (13.121), and (13.123) into Eq. (13.124) and integrating over the surface, using Eqs. (76) and (95) from Appendix II [with $z = kw_0 \sin\theta$, $b = k \sin\theta$, and letting $\phi = \pi/2$ so that $\cos(\phi - \phi_0) = \sin\phi_0$], gives

$$\tilde{p}(r,\theta) = -ja\tilde{p}_0 \frac{e^{-jkr}}{4r} D(\theta), \tag{13.125}$$

where the directivity function $D(\theta)$ is given by

$$D(\theta) = \frac{2J_1(ka\sin\theta)}{\sin\theta}\cos\theta. \tag{13.126}$$

The on-axis pressure is evaluated by setting $\theta = 0$ in Eq. (13.70) before inserting it in Eq. (13.124) and integrating over the surface to give

$$D(0) = ka \tag{13.127}$$

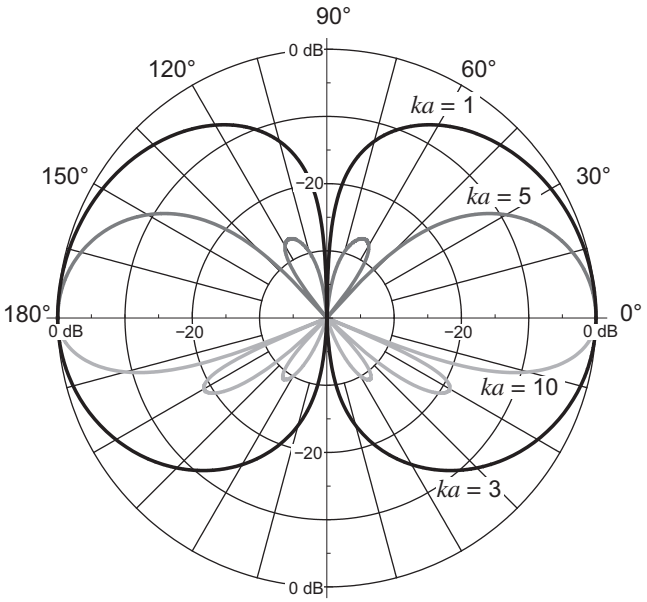

FIG. 13.9 Far-field directivity patterns for a resilient circular disk in free space as a function of $ka = 2\pi a/\lambda = \omega/c$, where a is the radius of the disk.

so that the on-axis response can be written as

$$\tilde{p}(r,0) = -jka^2\tilde{p}_0\frac{e^{-jkr}}{4r}, \tag{13.128}$$

which just gives a constant 6 dB/octave rising response at all frequencies for a given driving pressure. The normalized directivity function $20\log_{10}|D(\theta)/D(0)|$ is plotted in Fig. 13.9 for four values of $ka = 2\pi a/\lambda$, that is, for four values of the ratio of the circumference of the disk to the wavelength. *The directivity pattern is that of a rigid piston in an infinite baffle multiplied by* $\cos\theta$. When the circumference of the disk ($2\pi a$) is less than one-half wavelength, that is, $ka < 0.5$, the resilient disk behaves essentially like a dipole point source. When ka becomes greater than 3, the resilient disk is highly directional, like the piston in an infinite baffle. In fact, at very high frequencies, they both radiate sound as a narrow central lobe (Airy disk) accompanied by a number of very small side lobes, in which case the factor of $\cos\theta$ makes relatively little difference. In the case of a push-pull electrostatic loudspeaker,

$$\tilde{p}_0 = \frac{E_P}{d}\cdot\frac{2\tilde{I}_{in}}{j\omega\pi a^2}, \tag{13.129}$$

where E_P is the polarizing voltage, d is the membrane-electrode separation, and $\tilde{I}_{in}$ is the static input current to each electrode, assuming that the motional current is negligible in comparison. Substituting this in Eq. (13.128) yields

$$\tilde{p}(r,0) = -\frac{E_P}{d}\cdot\frac{\tilde{I}_{in}e^{-jkr}}{2\pi rc}, \tag{13.130}$$

which is Walker's equation, [17] albeit obtained by a slightly different method.

Near-field pressure. The near-field pressure distribution is given by Eq. (13.28) taking into account the surface pressure on both sides:

$$\tilde{p}(r,\theta) = 2\int_0^{2\pi}\int_0^{a}(\tilde{p}_+(w_0)-\tilde{p}_-(w_0))\frac{\partial}{\partial z_0}g(r,\theta|w_0,\phi_0)|_{z_0=0+}w_0 dw_0 d\phi_0, \tag{13.131}$$

where the Green's function in spherical-cylindrical coordinates given by Eq. (13.68) is used. It has been shown [16] that inserting Eqs. (13.68) and (13.123) into Eq. (13.131) and integrating over the surface gives

$$\begin{aligned}\tilde{p}(r,\theta) = -j\tilde{p}_0\sum_{n=0}^{\infty}\frac{(-1)^n\Gamma\left(n+3/2\right)}{\Gamma(n+2)\Gamma\left(2n+3/2\right)}\left(\frac{ka}{2}\right)^{2n+2}\\ \times{}_1F_2\left(n+1;n+2,2n+\frac{5}{2};-\frac{k^2a^2}{4}\right)h_{2n+1}^{(2)}(kr)P_{2n+1}(\cos\theta),\end{aligned} \tag{13.132}$$

which converges for $r > a$ but is generally used for $w \geq a$. The other part of the Green's function of Eq. (13.68) could be used to derive an expression for $r < a$. However, a better expression is provided by moving the origin of the coordinate system to a point on the z axis that lies the same plane as the observation point to give

$$\tilde{p}(w,z) = \frac{j\tilde{p}_0}{\sqrt{\pi}kw}\sum_{n=0}^{\infty}(-1)^n(4n+3)\frac{\Gamma\left(n+3/2\right)}{\Gamma(n+1)}j_{2n+1}(kw)f_{2n+1}, \tag{13.133}$$

where f_{2n+1} is given by the following recursion formulas:

$$f_1 = j\left(\frac{z}{r_a}e^{-jkr_a}-e^{-jkz}\right), \tag{13.134}$$

$$f_{2n+1} = -f_{2n-1}+kr_a h_{2n}^{(2)}(kr_a)(P_{2n+1}(z/r_a)-P_{2n-1}(z/r_a)), \tag{13.135}$$

and

$$r_a = \sqrt{z^2+a^2}, \tag{13.136}$$

which converges for $w^2 < a^2 + z^2$ but is generally used for $w < a$ and is thus termed the *paraxial* solution. The number of terms in the expansion needed for convergence decreases linearly towards the z-axis until just a single term is needed. This is the closed-form axial solution:

$$\tilde{p}(0,z) = \frac{\tilde{p}_0}{2}\left(e^{-jkz}-\frac{z}{\sqrt{z^2+a^2}}e^{-jk\sqrt{z^2+a^2}}\right). \tag{13.137}$$

The pressure field for three values of ka is plotted in Fig. 13.10. We can see that the plane wave region near the surface forms more readily than in the case of the rigid piston (see Fig. 13.6), no doubt aided by the uniform pressure distribution at the surface of the resilient disk. At $ka = 6\pi$, the pressure field fluctuations in the vicinity of the resilient disk are smaller than for the rigid piston. Furthermore, the axial pressure response of a rigid disk given by Eq. (13.111) has nulls, whereas the resilient disk axial response given by Eq. (13.137) is oscillatory but with decreasing magnitude towards the face of the disk.

Surface velocity. Using the solutions for the near-field pressure from Eqs. (13.133), (13.134), and (13.135), and taking the normal pressure gradient at the surface of the disk, the surface velocity is given by

$$\begin{aligned}\tilde{u}_0(w) &= \frac{j}{k\rho c}\frac{d}{dz}\tilde{p}(w,z)\Big|_{z=0+} \\ &= -\frac{\tilde{p}_0}{\rho c\sqrt{\pi}}\sum_{n=0}^{\infty}(-1)^n(4n+3)\frac{\Gamma\left(n+3/2\right)}{\Gamma(n+1)}f'_{2n}\frac{j_{2n+1}(kw)}{kw},\end{aligned} \tag{13.138}$$

where

$$f'_0 = 1 - j\frac{e^{-jka}}{ka}, \tag{13.139}$$

$$f'_{2n} = -f'_{2n-2} - h^{(2)}_{2n}(ka)((2n+1)P_{2n}(0) - (2n-1)P_{2n-2}(0)). \tag{13.140}$$

The magnitude and phase of the normalized velocity are shown in Fig. 13.11 and Fig. 13.12, respectively, for four values of ka. For small k, it can be shown to agree well with the asymptotic expression given by Eq. (13.144). We see that the velocity increases rapidly towards the rim, where it is singular. This is a feature of uniform pressure sources in general due to the discontinuity at the rim. However, it is exacerbated in this case by the acoustic short circuit between the front and rear surfaces of the dipole source.

Radiation admittance and low-frequency asymptotic surface velocity. The near-field pressure distribution is given by Eq. (13.28) taking into account the surface pressure on both sides:

$$\tilde{p}(w,z) = \int_0^{2\pi}\int_0^{a}(\tilde{p}_+(w_0) - \tilde{p}_-(w_0))\frac{\partial}{\partial z_0}g(w,z|w_0,z_0)|_{z_0=0+}w_0 dw_0 d\phi_0, \tag{13.141}$$

where the inregral Green's function in cylindrical coordinates given by Eq. (13.52) is used. In this form Eq. (13.141) is known as the dipole King integral. Inserting Eqs. (13.52), and (13.123) into Eq. (13.141) and integrating over the surface gives

$$\tilde{p}(w,z) = -ka\rho_0 c\tilde{u}_0\int_0^{\infty}J_0(k_w w)J_1(k_w a)\frac{1}{k_z}e^{-jk_z z}dk_w, \tag{13.142}$$

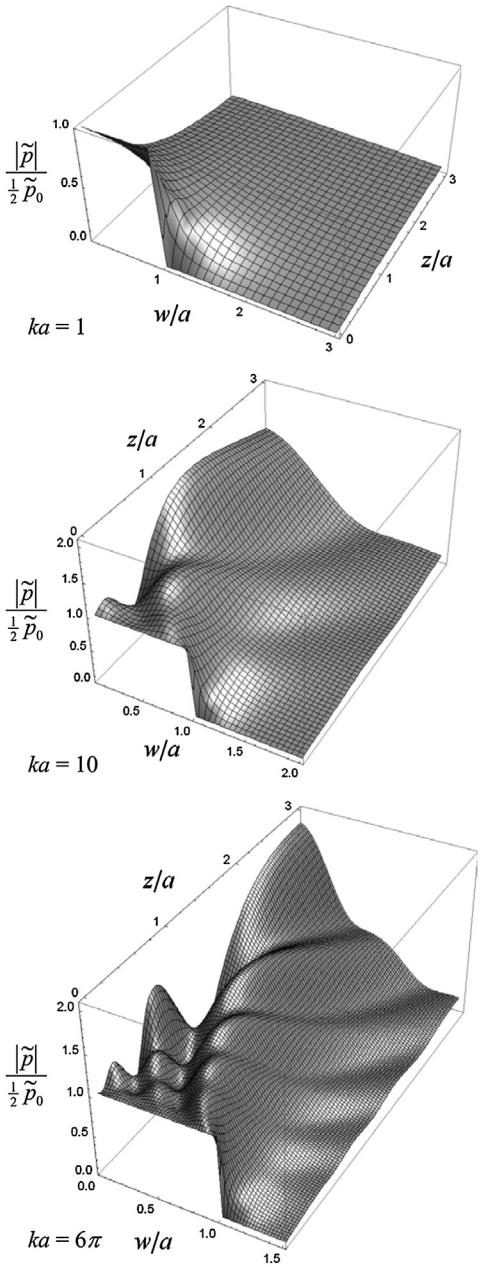

FIG. 13.10 Normalized near-field pressure plots for a resilient circular disk in free space as a function of $ka = 2\pi a/\lambda = 2\pi fa/c$, where a is the radius of the disk.

$|\tilde{p}|$ is the pressure magnitude, $\tilde{p}_0$ is the driving pressure.

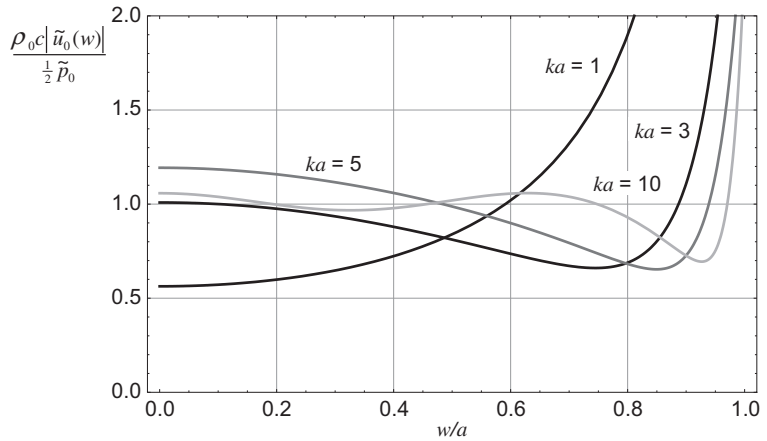

FIG. 13.11 Normalized surface velocity magnitude for a resilient circular disk in free space as a function of *w/a*, where *w* is the radial ordinate and $ka = 2\pi a/\lambda = \omega/c$, where *a* is the radius of the disk.

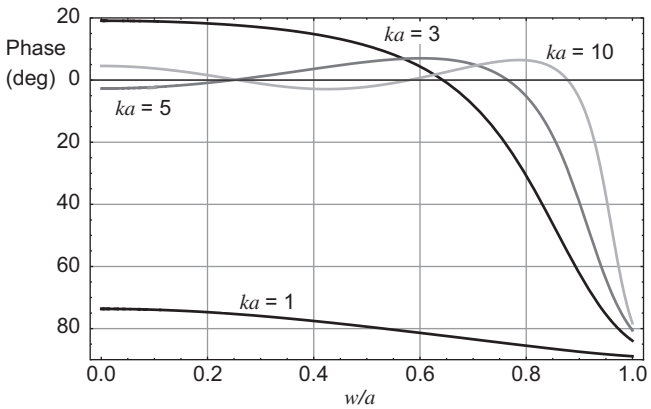

FIG. 13.12 Surface velocity phase for a resilient circular disk in free space as a function of *w/a*, where *w* is the radial ordinate and $ka = 2\pi a/\lambda = \omega/c$, where *a* is the radius of the disk.

where we have again used the integral of Eq. (95) from Appendix II and k_z is given by Eq. (13.51). The disk velocity $\tilde{u}_0(w)$ can be derived using the following relationship for the normal pressure gradient:

$$\begin{aligned}\tilde{u}_0(w) &= \frac{1}{-jk\rho_0 c}\frac{\partial}{\partial z}\tilde{p}(w,z)\Big|_{z=0+} \\ &= \frac{a\tilde{p}_0}{2k\rho_0 c}\int_0^\infty J_1(k_w a)J_0(k_w w)k_z dk_w.\end{aligned} \tag{13.143}$$

For small k, we obtain

$$\begin{aligned}\tilde{u}_0(w)\Big|_{k\to 0} &= \frac{ja\tilde{p}_0}{2k\rho_0 c}\int_0^\infty J_1(k_w a)J_0(k_w w)k_w dk_w \\ &= \frac{j\tilde{p}_0 \boldsymbol{E}(w^2/a^2)}{\pi ka\rho_0 c}\left(1-\frac{w^2}{a^2}\right)^{-1},\end{aligned} \tag{13.144}$$

where $\boldsymbol{E}$ is the complete elliptic integral of the second kind. Hence there is a singularity at the rim. The total volume velocity $\tilde{U}_0$ is found by integrating the velocity from Eq. (13.143) over the surface of the disk and again using the integral of Eq. (95) from Appendix II to give

$$\begin{aligned}\tilde{U}_0 &= \int_0^{2\pi}\int_0^a \tilde{u}_0(w)w\,dw\,d\phi \\ &= \frac{\pi a^2\tilde{p}_0}{k\rho_0 c}\left(\int_0^k J_1^2(k_w a)\frac{\sqrt{k^2-k_w^2}}{k_w}dk_w - j\int_k^\infty J_1^2(k_w a)\frac{\sqrt{k_w^2-k^2}}{k_w}dk_w\right),\end{aligned} \tag{13.145}$$

The solution [16,20] has been shown to be

$$Y_s = \frac{\tilde{U}_0}{S\tilde{p}_0} = \boldsymbol{G}_s + jB_s, \tag{13.146}$$

where $\tilde{U}_0 = \pi a^2\tilde{u}_0$ is the total volume velocity and $\boldsymbol{G}_s$ is the specific radiation conductance in $\mathrm{m^3\cdot N^{-1}\cdot s^{-1}}$ ($\mathrm{rayl^{-1}}$) given by

$$\begin{aligned}\boldsymbol{G}_s &= \frac{1}{\rho_0 c}\left(1+\frac{J_1(2ka)}{ka}-2J_0(2ka)-\pi(J_1(2ka)\mathbf{H}_0(2ka)-J_0(2ka)\mathbf{H}_1(2ka))\right) \\ &\approx \frac{1}{\rho_0 c}\cdot\frac{k^2a^2}{6}, \qquad ka<0.5,\end{aligned} \tag{13.147}$$

where the bold $\boldsymbol{G}$ indicates that the quantity varies with frequency. B_s is the specific radiation susceptance in $\mathrm{m^3\cdot N^{-1}\cdot s^{-1}}$ ($\mathrm{rayl^{-1}}$) given by

$$\begin{aligned}B_s &= -\frac{1}{\rho_0 c}\left(\frac{4}{\pi\, ka}-\frac{\mathbf{H}_1(2ka)}{ka}+\frac{4ka}{\pi}{}_2F_3\left(1,1;\frac{3}{2},\frac{3}{2},2;-k^2a^2\right)\right) \\ &\approx \frac{1}{\rho_0 c}\cdot\frac{4}{\pi ka}, \qquad ka<0.5,\end{aligned} \tag{13.148}$$

where J_n and $\mathbf{H}_n$ are Bessel and Struve functions respectively and ${}_2F_3$ is a hypergeometric function. Plots of the real and imaginary parts of

$$\rho_0 c Y_s = \rho_0 c(\boldsymbol{G}_s + jB_s) \tag{13.149}$$

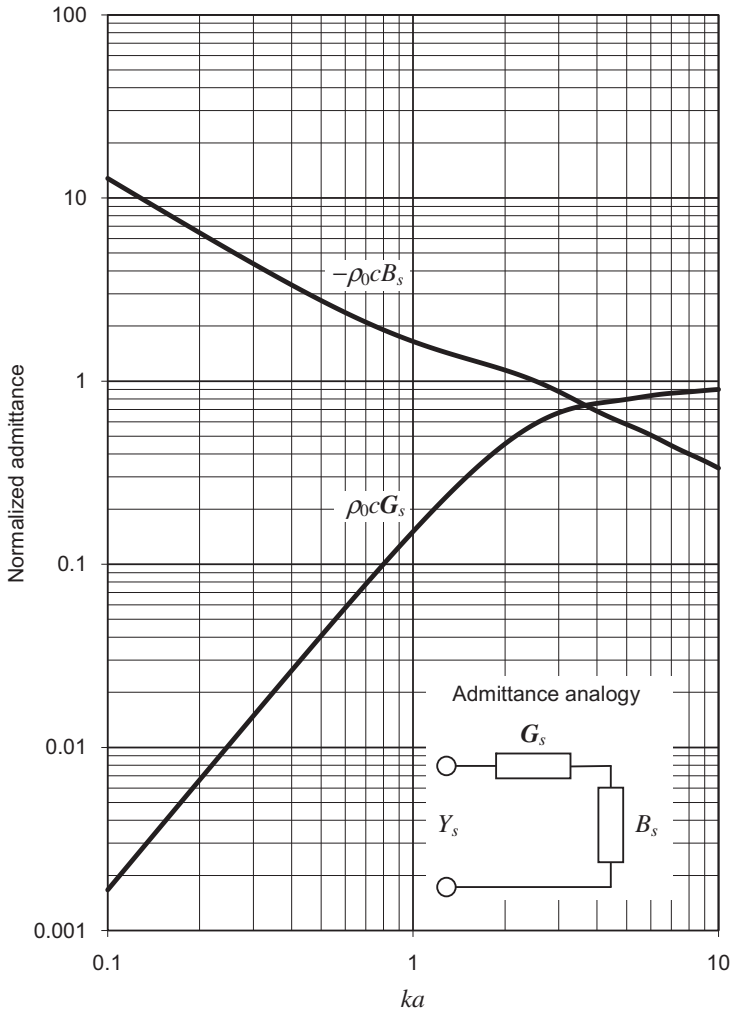

FIG. 13.13 Real and imaginary parts of the normalized specific radiation admittance $\rho_0 c Y_s$ of the air load on one side of a plane circular resilient disk of radius a in free space.

Frequency is plotted on a normalized scale, where $ka = 2\pi a/\lambda = 2\pi fa/c$.

are shown in Fig. 13.13 as a function of ka. Similar graphs of the real and imaginary parts of the specific impedance

$$\frac{Z_s}{\rho_0 c} = \frac{\boldsymbol{R}_s + jX_s}{\rho_0 c} = \frac{1}{\rho_0 c}\left(\frac{\boldsymbol{G}_s}{\boldsymbol{G}_s^2 + B_s^2} - j\frac{B_s}{\boldsymbol{G}_s^2 + B_s^2}\right) \tag{13.150}$$

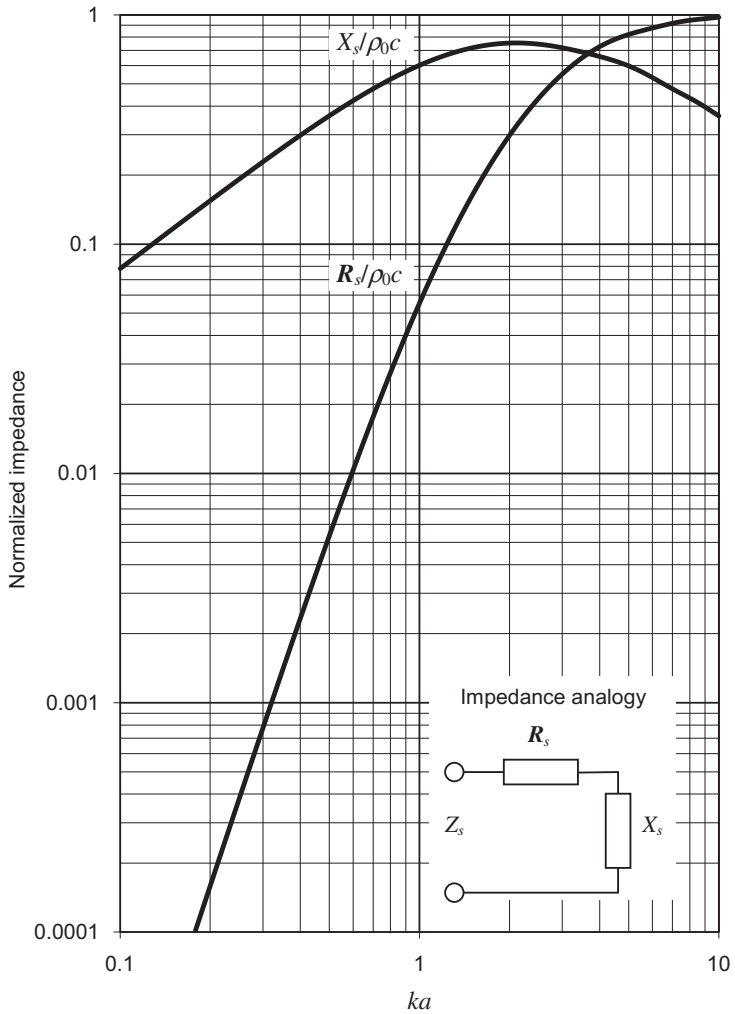

FIG. 13.14 Real and imaginary parts of the normalized specific radiation impedance $Z_s/\rho_0 c$ of the air load on one side of a plane circular resilient disk of radius a in free space.

Frequency is plotted on a normalized scale, where $ka = 2\pi a/\lambda = 2\pi fa/c$.

are shown in Fig. 13.14. The specific admittance is in $m^3 \cdot N^{-1} \cdot s^{-1}$ ($rayl^{-1}$). Whereas the impedance and admittance functions of the rigid disk in an infinite baffle show ripples (see Fig. 4.35 and Fig. 4.36 respectively), those of the resilient disk are smooth almost monotonic functions. We can see that at low frequencies the impedance and admittance curves are more reactive than those of a piston in an infinite baffle, so that less power is radiated. This is due to the cancellation of the acoustic output by the rear wave or acoustic "short circuit", which is generally the case with all dipole sources.

Relationship between a resilient disk in free space and a rigid piston in an infinite baffle. Suppose that the radiation resistance and reactance of a rigid disk in an infinite baffle are denoted by $\boldsymbol{R}_s$ and X_s respectively and $\boldsymbol{G}_s$ and B_s are the radiation conductance and susceptance respectively of a resilient disk in free space as defined in Eqs. (13.147) and (13.148), then

$$(\rho_0 c)^2 \frac{d}{d(ka)} ka\boldsymbol{G}_s(ka) = \boldsymbol{R}_s(ka) = \rho_0 c\left(1 - \frac{J_1(2ka)}{ka}\right), \tag{13.151}$$

or

$$\boldsymbol{G}_s(ka) = \frac{1}{ka(\rho_0 c)^2}\int \boldsymbol{R}_s(ka)d(ka), \tag{13.152}$$

and

$$(\rho_0 c)^2 \frac{d}{d(ka)} kaB_s(ka) = X_s(ka) = \rho_0 c\frac{\mathbf{H}_1(2ka)}{ka}, \tag{13.153}$$

or

$$B_s(ka) = \frac{1}{ka(\rho_0 c)^2}\left(\int X_s(ka)d(ka) + \frac{4}{\pi}\right), \tag{13.154}$$

13.9 RADIATION FROM A RESILIENT DISK IN AN INFINITE BAFFLE [19]

A resilient disk in an infinite baffle, like the previous example, represents a source with a uniform pressure distribution over its radiating surface, unlike the rigid piston where the velocity is uniform. This makes the problem slightly harder to solve because we have to include a trial function for the disk velocity distribution in the surface integral. The trial function is in the form of a series expansion, the unknown coefficients of which have to be calculated via a set of simultaneous equations. However, it is worth the effort because, as we shall see, this particular source represents the diffraction pattern due to a plane wave passing through a circular aperture in an infinite screen, which is an important result in optics too. The transmission coefficient, or radiation conductance, was first calculated by Bouwkamp [20] in his PhD dissertation using the boundary value method in the oblate-spheroidal coordinate system. Less than a decade later, Spence [21] calculated the surface velocity distribution and directivity pattern. However, oblate-spheroidal functions are rather complicated, so instead we shall use the boundary integral method with the Green's function in cylindrical coordinates and a trial function first used by Streng [22] for a membrane.

Boundary conditions. The configuration is the same as that shown in Fig. 13.3. The infinitesimally thin membrane-like resilient disk is mounted in an infinite baffle in the xy plane with its center at the origin. It is assumed to be perfectly flexible, has zero mass, and is free at its perimeter. It is driven by a uniformly distributed harmonically varying pressure $\tilde{p}_0$ and thus radiates sound from both sides into a homogeneous loss-free acoustic medium. In fact, there need not be a disk present at all and instead the driving pressure could be acting upon the air particles directly. However, for expedience, the area over which this driving pressure is applied shall be referred to as a disk from here onwards. As with the

rigid piston in an infinite baffle, we will model this as a "breathing" disk in free space. Due to the symmetry of the pressure fields on either side of the baffle

$$\tilde{p}(w,z) = \tilde{p}(w,-z). \tag{13.155}$$

Consequently, there is a Neumann boundary condition in the plane of the disk where these fields meet:

$$\frac{\partial}{\partial z}\tilde{p}(w,z)\Big|_{z=0} = 0, \quad a < w \leq \infty, \tag{13.156}$$

which is satisfied automatically. On the front and rear surfaces of the disk, the pressures are $\tilde{p}_+$ and $\tilde{p}_-$ respectively, which are given by

$$\tilde{p}_+(w_0) = \tilde{p}_-(w_0) = \tilde{p}_0/2, \quad 0 \leq w_0 \leq a. \tag{13.157}$$

The pressure gradient is given by

$$\frac{\partial}{\partial z_0}\tilde{p}(w_0,z_0)\Big|_{z_0=0+} = \begin{cases} -jk\rho_0 c\tilde{u}(w_0), & 0 \leq w_0 \leq a, \\ 0, & w_0 > a, \end{cases} \tag{13.158}$$

where $\tilde{u}(w_0)$ is the unknown surface velocity distribution and k is the wave-number given by $k = \omega/c = 2\pi/\lambda$, where ω is the angular frequency of excitation, ρ_0 is the density of the surrounding medium, c is the speed of sound in that medium, and λ is the wavelength. We will use the following trial function, which is itself a solution to the free-space Helmholtz wave equation in oblate-spheroidal coordinates, [20]

$$\tilde{u}_0(w_0) = \frac{\tilde{p}_0}{2\rho_0 c}\sum_{n=0}^{\infty} A_n\left(n+\frac{1}{2}\right)\left(1-\frac{w_0^2}{a^2}\right)^{n-\frac{1}{2}}, \tag{13.159}$$

where A_n are the as-yet unknown power series coefficients which will be evaluated by means of a set of simultaneous equations in matrix form. Note that the $n = 0$ term is singular when $w_0 = a$. This is due to the discontinuity at the rim, which is inherent in the problem. [2] Otherwise, if we were modelling a problem with zero velocity at the rim, such as a membrane with a clamped rim [18], we would replace $(n - ½)$ in the index with $(n + ½)$. Using a trial function, any velocity distribution is possible and this is not the only trial function which may be used [42],[43].

Solution of the power series coefficients. The near-field pressure distribution is given by Eq. (13.27) taking into account the double-strength source:

$$\tilde{p}(w,z) = 2\int_0^{2\pi}\int_0^{a} g(w,z|w_0,z_0)\frac{\partial}{\partial z_0}\tilde{p}(w_0,z_0)\Big|_{z_0=0} w_0 dw_0 d\phi_0, \tag{13.160}$$

where the integral Green's function in cylindrical coordinates given by Eq. (13.52) is used. In this form Eq. (13.160) is known as the monopole King integral. Inserting Eqs. (13.52), (13.158), and (13.159) into Eq. (13.160) and integrating over the surface using Eq. (96) from Appendix II gives

$$\tilde{p}(w,z) = ka\frac{\tilde{p}_0}{2}\sum_{n=0}^{\infty} A_n\Gamma\left(n+\frac{3}{2}\right)\int_0^{\infty}\left(\frac{2}{ak_w}\right)^{n-\frac{1}{2}} J_0(k_w w)J_{n+\frac{1}{2}}(k_w a)\frac{e^{-jk_z z}}{k_z}dk_w, \tag{13.161}$$

where k_z is given by Eq. (13.51). At the surface of the disk, we have the coupling condition

$$\tilde{p}(w,z)\Big|_{z=0+} = \frac{\tilde{p}_0}{2}, \qquad 0 \le w \le a, \tag{13.162}$$

which leads to the following equation:

$$\sum_{n=0}^{\infty} A_n I_n(w) = \Phi(w), \tag{13.163}$$

where

$$\Phi(w) = 1, \qquad 0 \le w \le a, \tag{13.164}$$

which is to be solved for the power series coefficients A_n. The integral $I_n(w)$ can be split into two parts:

$$I_n(w) = I_{nR}(w) + jI_{nI}(w), \tag{13.165}$$

where the real part is given by

$$I_{nR}(w) = ka\Gamma\left(n+\frac{3}{2}\right)\int_0^k \left(\frac{2}{k_w a}\right)^{n-\frac{1}{2}} J_{n+\frac{1}{2}}(k_w a)J_0(k_w w)\frac{1}{\sqrt{k^2-k_w^2}}dk_w \tag{13.166}$$

and the imaginary part is given by

$$I_{nI}(w) = ka\Gamma\left(n+\frac{3}{2}\right)\int_k^\infty \left(\frac{2}{k_w a}\right)^{n-\frac{1}{2}} J_{n+\frac{1}{2}}(k_w a)J_0(k_w w)\frac{1}{\sqrt{k_w^2-k^2}}dk_w. \tag{13.167}$$

These integrals can be shown [19] to be given by

$$I_{nR}(w) = \sqrt{\pi}\sum_{m=0}^{\infty}\sum_{r=0}^{\infty}\frac{(-1)^{m+r}\Gamma\left(n+\frac{3}{2}\right)\Gamma(m+r+1)}{(m!)^2 r!\,\Gamma\left(r+n+\frac{3}{2}\right)\Gamma\left(m+r+\frac{3}{2}\right)}\left(\frac{ka}{2}\right)^{2(m+r+1)}\left(\frac{w}{a}\right)^{2m}, \tag{13.168}$$

$$I_{nI}(w) = \sqrt{\pi}\sum_{m=0}^{\infty}\sum_{r=0}^{\infty}\frac{(-1)^{m+r+n}\Gamma\left(n+\frac{3}{2}\right)\Gamma\left(m+r-n+\frac{1}{2}\right)}{(m!)^2 r!\Gamma\left(r-n+\frac{1}{2}\right)\Gamma(m+r-n+1)}\left(\frac{ka}{2}\right)^{2(m+r-n)+1}\left(\frac{w}{a}\right)^{2m}, \tag{13.169}$$

which are both expansions in $(w/a)^{2m}$. We also note that

$$\Phi(w) = \sum_{m=0}^{\infty}\delta_{m0}\left(\frac{w}{a}\right)^{2m}, \qquad 0 \le w \le a, \tag{13.170}$$

where δ_{m0} is the Kronecker delta function. Inserting Eqs. (13.165), (13.168), (13.169), and (13.170) in Eq. (13.163) and equating the coefficients of $(w/a)^{2m}$ yields the following $(N+1) \times (N+1)$ matrix equation:

$$\mathbf{M}\cdot\mathbf{a} = \mathbf{b} \Rightarrow \mathbf{a} = \mathbf{M}^{-1}\cdot\mathbf{b}, \tag{13.171}$$

where the matrix $\mathbf{M}$ and vectors $\mathbf{a}$ and $\mathbf{b}$ are given by

$$\mathbf{M}(m+1,n+1) = {}_n\mathbf{P}_m(ka) + j_n\mathbf{T}_m(ka), \qquad \begin{cases} m = 0,1,\cdots,N \\ n = 0,1,\cdots,N, \end{cases} \tag{13.172}$$

$$\mathbf{b}(m+1) = \delta_{m0}, \qquad m = 0,1,\cdots,N, \tag{13.173}$$

$$\mathbf{a}(n+1) = A_n, \qquad n = 0,1,\cdots,N, \tag{13.174}$$

and the infinite power series limits have been truncated to order N. The monopole cylindrical wave functions ${}_n\mathbf{P}_m$ and ${}_n\mathbf{T}_m$ are named the Spence and Stenzel functions respectively in tribute to their pioneering work and are defined by

$${}_n\mathbf{P}_m(ka) = \sqrt{\pi}\sum_{r=0}^{N}\frac{(-1)^{m+r}\Gamma\left(n+\frac{3}{2}\right)\Gamma(m+r+1)}{(m!)^2 r!\Gamma\left(r+n+\frac{3}{2}\right)\Gamma\left(m+r+\frac{3}{2}\right)}\left(\frac{ka}{2}\right)^{2(m+r+1)}, \tag{13.175}$$

$${}_n\mathbf{T}_m(ka) = \sqrt{\pi}\sum_{r=0}^{N}\frac{(-1)^{m+r+n}\Gamma\left(n+\frac{3}{2}\right)\Gamma\left(m+r-n+\frac{1}{2}\right)}{(m!)^2 r!\Gamma\left(r-n+\frac{1}{2}\right)\Gamma(m+r-n+1)}\left(\frac{ka}{2}\right)^{2(m+r-n)+1}. \tag{13.176}$$

Now that we have the surface velocity series coefficients A_n, we can derive some radiation characteristics for the resilient disk.

Far-field pressure. The far-field pressure distribution is given by Eq. (13.27) taking into account the double-strength source:

$$\tilde{p}(r,\theta) = 2\int_0^{2\pi}\int_0^{a} g(r,\theta|w_0,\phi_0)\frac{\partial}{\partial z_0}\tilde{p}(w_0,z_0)\Big|_{z_0=0+} w_0 dw_0 d\phi_0, \tag{13.177}$$

where the far-field Green's function in spherical-cylindrical coordinates given by Eq. (13.70) is used. Inserting Eqs. (13.70), (13.158), and (13.159) into Eq. (13.177) and integrating over the surface, using Eqs. (76) and (96) from Appendix II [with $z = kw_0 \sin\theta$, $b = k\sin\theta$, and letting $\phi = \pi/2$ so that $\cos(\phi - \phi_0) = \sin\phi_0$], gives

$$\tilde{p}(r,\theta) = -ja\tilde{p}_0\frac{e^{-jkr}}{4r}D(\theta), \tag{13.178}$$

where the directivity function $D(\theta)$ is given by

$$D(\theta) = ka \sum_{n=0}^{N} A_n \Gamma\left(n + 3/2\right) \left(\frac{2}{ka \sin\theta}\right)^{n+\frac{1}{2}} J_{n+\frac{1}{2}}(ka \sin\theta). \tag{13.179}$$

The on-axis pressure is evaluated by setting $\theta = 0$ in Eq. (13.70) before inserting it in Eq. (13.177) and integrating over the surface to give

$$D(0) = ka \sum_{n=0}^{N} A_n \approx \begin{cases} 4j/\pi, & ka < 0.5 \\ ka, & ka > 2. \end{cases} \tag{13.180}$$

It is worth noting that $D(0)$ is simply the normalized radiation admittance, that is

$$D(0) = (\boldsymbol{G}_s + jB_s)/(\rho_0 c)$$

where $\boldsymbol{G}_s$ and B_s are given by Eq. (13.193) and (13.194) respectively. The asymptotic expression for low-frequency on-axis pressure is then simply

$$\tilde{p}(r, 0) \approx \frac{a}{\pi r} \tilde{p}_0 e^{-jkr}, \quad ka < 0.5 \tag{13.181}$$

and at high frequencies

$$\tilde{p}(r, 0) \approx j \frac{ka^2}{4r} \tilde{p}_0 e^{-jkr}, \quad ka > 2, \tag{13.182}$$

which is the same as for a resilient disk in free space at all frequencies. The on-axis response is shown in Fig. 13.15, calculated from the magnitude of $D(0)$. The normalized directivity function

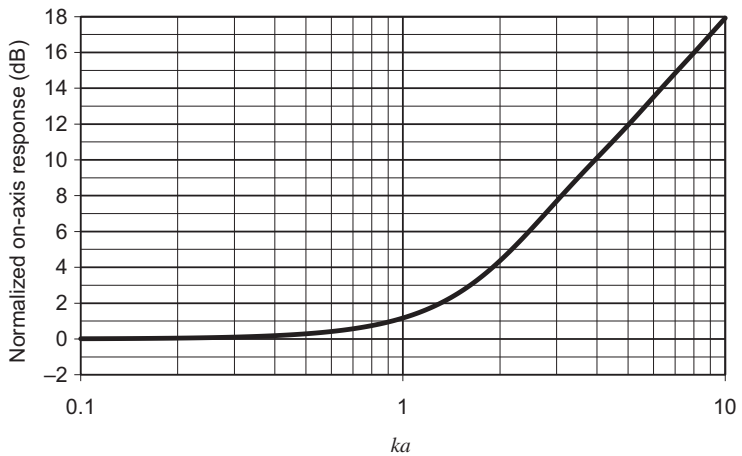

FIG. 13.15 Plot of 20 $\log_{10}(D(0))$ where $D(\theta)$ is the directivity function of a resilient disk of radius a in an infinite baffle. The uniform driving pressure is constant.

Frequency is plotted on a normalized scale, where $ka = 2\pi a/\lambda = 2\pi fa/c$.

$20\log_{10}|D(\theta)/D(0)|$ is plotted in Fig. 13.16 for four values of $ka = 2\pi a/\lambda$, that is, for four values of the ratio of the circumference of the piston to the wavelength. When the circumference of the piston ($2\pi a$) is less than one-half wavelength, that is, $ka < 0.5$, the disk behaves essentially like a point source. When ka becomes greater than 3, the resilient disk is highly directional, rather like the rigid piston in an infinite baffle except without the nulls.

Near-field pressure. The near-field pressure distribution is given by Eq. (13.27) taking into account the surface pressure on both sides:

$$\tilde{p}(r,\theta) = 2\int_0^{2\pi}\int_0^{a} g(r,\theta|w_0,\phi_0)\frac{\partial}{\partial z_0}\tilde{p}(w_0,z_0)\Big|_{z_0=0+} w_0 dw_0 d\phi_0, \tag{13.183}$$

where the Green's function in spherical-cylindrical coordinates given by Eq. (13.68) is used. It has been shown [19] that inserting Eqs. (13.68), (13.158), and (13.159) into Eq. (13.183) and integrating over the surface gives

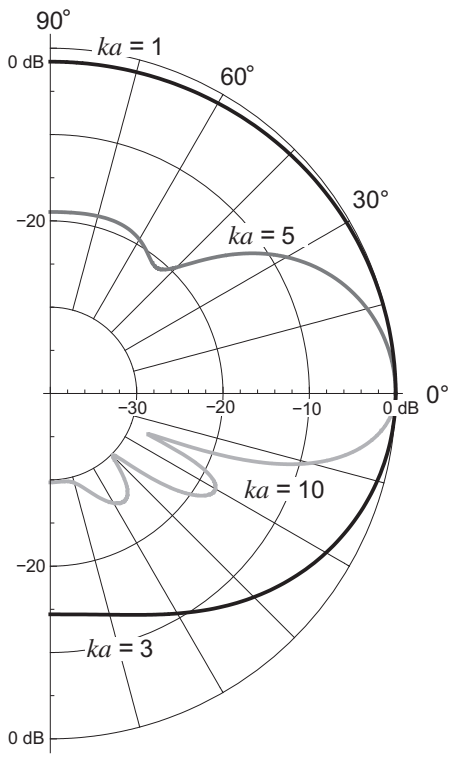

FIG. 13.16 Far-field directivity patterns for a resilient disk in an infinite baffle as a function of $ka = 2\pi a/\lambda = \omega/c$, where a is the radius of the disk.

$$p(r,\theta) = -\tilde{p}_0 \sum_{n=0}^{N} A_n \sum_{p=0}^{P} \frac{(-1)^p \Gamma\left(p+1/2\right)\Gamma\left(n+3/2\right) h_{2p}^{(2)}(kr) P_{2p}(\cos\theta)}{\Gamma\left(2p+1/2\right)\Gamma\left(p+n+3/2\right)} \times \left(\frac{ka}{2}\right)^{2p+2} {}_1F_2\left(p+1; p+n+\frac{3}{2}, 2p+\frac{3}{2}; \frac{k^2a^2}{4}\right), \tag{13.184}$$

which converges for $r > a$. For $r \leq a$, we derive a suitable expression from Eq. (13.161), which is weakly singular at $k_w = k$. However, we can remove this singularity as follows: First, we substitute

$$k_w = k\sqrt{1-t^2} \text{ for } k_w \leq k$$

and

$$k_w = k\sqrt{1+t^2} \text{ for } k_w > k$$

in Eq. (13.161) to obtain

$$\tilde{p}(w,z) = \tilde{p}_0 \sum_{n=0}^{\infty} A_n \Gamma\left(n+\frac{3}{2}\right)(I_{Fin} + jI_{Inf}), \tag{13.185}$$

where

$$I_{Fin} = \left(\frac{2}{ka}\right)^{n-\frac{3}{2}} \int_0^1 \left(\frac{1}{1-t^2}\right)^{\frac{n}{2}+\frac{1}{4}} J_{n+\frac{1}{2}}\left(ka\sqrt{1-t^2}\right) J_0\left(kw\sqrt{1-t^2}\right) e^{-jkzt} dt, \tag{13.186}$$

$$I_{Inf} = \left(\frac{2}{ka}\right)^{n-\frac{3}{2}} \int_0^\infty \left(\frac{1}{1+t^2}\right)^{\frac{n}{2}+\frac{1}{4}} J_{n+\frac{1}{2}}\left(ka\sqrt{1+t^2}\right) J_0\left(kw\sqrt{1+t^2}\right) e^{-kzt} dt. \tag{13.187}$$

We then apply the expansion or Eq. (109) from Appendix II to give

$$I_{Fin} + jI_{Inf} = \sum_{p=0}^{\infty} \frac{(-1)^p}{p!\Gamma\left(n+p+3/2\right)} \left(\frac{ka}{2}\right)^{2p+2} {}_2F_1\left(-p, -n-p-\frac{1}{2}; 1; \frac{w^2}{a^2}\right) \times \left(\int_0^1 (1-t^2)^p e^{-jkzt} dt + j\int_0^\infty (1+t^2)^p e^{-kzt} dt\right), \tag{13.188}$$

which, after integrating, yields

$$I_{Fin} = \frac{\sqrt{\pi}}{2}\sum_{p=0}^{\infty}\frac{(-1)^p}{\Gamma\left(n+p+\frac{3}{2}\right)}\left(\frac{ka}{2}\right)^{2p+2}{}_2F_1\left(-p,-n-p-\frac{1}{2};1;\frac{w^2}{a^2}\right) \times\left(\frac{2}{kz}\right)^{p+\frac{1}{2}}\left(J_{p+\frac{1}{2}}(kz)-j\mathbf{H}_{p+\frac{1}{2}}(kz)\right), \tag{13.189}$$

$$I_{Inf} = \frac{\sqrt{\pi}}{2}\sum_{p=0}^{\infty}\frac{(-1)^p}{\Gamma\left(n+p+3/2\right)}\left(\frac{ka}{2}\right)^{2p+2}{}_2F_1\left(-p,-n-p-\frac{1}{2};1;\frac{w^2}{a^2}\right) \times\left(\frac{2}{kz}\right)^{p+\frac{1}{2}}\left(\mathbf{H}_{p+\frac{1}{2}}(kz)-Y_{p+\frac{1}{2}}(kz)\right). \tag{13.190}$$

Equation (13.189) converges everywhere and is therefore suitable for $r < a$. Unfortunately, Eq. (13.190) only converges for $z^2 > w^2 + a^2$ and is therefore not suitable. However, Eq. (13.187) converges everywhere and can be calculated numerically without problem and is therefore suitable for $r < a$. Using the Babinet–Bouwkamp principle, this represents the field scattered by a hole in an infinite screen in the presence of an incident plane wave, as plotted in Fig. 13.39 for three values of ka.

Surface velocity. The magnitude and phase of the normalized velocity from Eq. (13.159) are shown in Fig. 13.17 and Fig. 13.18, respectively, for four values of ka. We see that the velocity increases rapidly

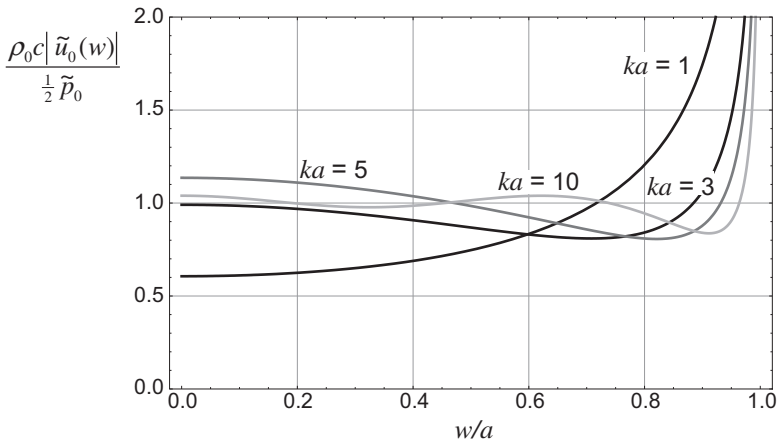

FIG. 13.17 Normalized surface velocity magnitude for a resilient circular disk in an infinite baffle as a function of *w/a* where *w* is the radial ordinate and $ka = 2\pi a/\lambda = \omega/c$, where *a* is the radius of the disk.

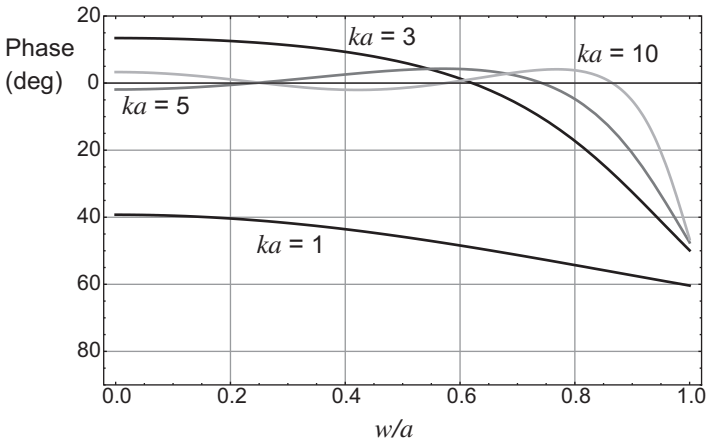

FIG. 13.18 Surface velocity phase for a resilient circular disk in an infinite baffle as a function of *w/a* where *w* is the radial ordinate and $ka = 2\pi a/\lambda = \omega/c$, where *a* is the radius of the disk.

towards the rim where it is singular. This is a feature of uniform pressure sources in general due to the discontinuity at the rim.

Radiation admittance. The total volume velocity $\tilde{U}_0$ is found by integrating the velocity from Eq. (13.159) over the surface of the disk to give

$$\tilde{U}_0 = \int_0^{2\pi}\int_0^{a} \tilde{u}_0(w_0) w_0 dw_0 d\phi_0 = \frac{\pi a^2 \tilde{p}_0}{2\rho_0 c} \sum_{n=0}^{N} A_n. \tag{13.191}$$

The specific radiation admittance is then given by

$$Y_s = \frac{\tilde{U}_0}{S\,\tilde{p}_0} = \boldsymbol{G}_s + jB_s, \tag{13.192}$$

where $\tilde{U}_0$ is the total volume velocity and $\boldsymbol{G}_s$ is the specific radiation conductance in $\mathrm{m}^3\cdot\mathrm{N}^{-1}\cdot\mathrm{s}^{-1}$ (rayl^{-1}) given by

$$\begin{aligned} \boldsymbol{G}_s &= \frac{1}{\rho_0 c}\Re\left(\sum_{n=0}^{N} A_n\right) \\ &\approx \frac{1}{\rho_0 c}\cdot\frac{8}{\pi^2}, \qquad ka < 0.5, \end{aligned} \tag{13.193}$$

where the bold $\boldsymbol{G}$ indicates that the quantity varies with frequency. B_s is the specific radiation susceptance in $\mathrm{m}^3\cdot\mathrm{N}^{-1}\cdot\mathrm{s}^{-1}$ (rayl^{-1}) given by

$$B_s = \frac{1}{\rho_0 c}\Im\left(\sum_{n=0}^{N} A_n\right) \approx \frac{1}{\rho_0 c}\cdot\frac{4}{\pi ka}, \qquad ka < 0.5. \tag{13.194}$$

Plots of the real and imaginary parts of

$$\rho_0 c Y_s = \rho_0 c(\mathbf{G}_s + jB_s) \tag{13.195}$$

are shown in Fig. 13.19 as a function of ka. Similar graphs of the real and imaginary parts of the specific impedance

$$\frac{Z_s}{\rho_0 c} = \frac{\boldsymbol{R}_s + jX_s}{\rho_0 c} = \frac{1}{\rho_0 c}\left(\frac{\boldsymbol{G}_s}{\boldsymbol{G}_s^2 + B_s^2} - j\frac{\boldsymbol{B}_s}{\boldsymbol{G}_s^2 + B_s^2}\right) \tag{13.196}$$

are shown in Fig. 13.20. The specific admittance is in $\mathrm{m}^3\cdot\mathrm{N}^{-1}\cdot\mathrm{s}^{-1}$ (rayl^{-1}). Whereas the impedance and admittance functions of the rigid disk in an infinite baffle show ripples (see Fig. 4.35 and Fig. 4.36 respectively), those of the resilient disk are smooth, almost monotonic functions.

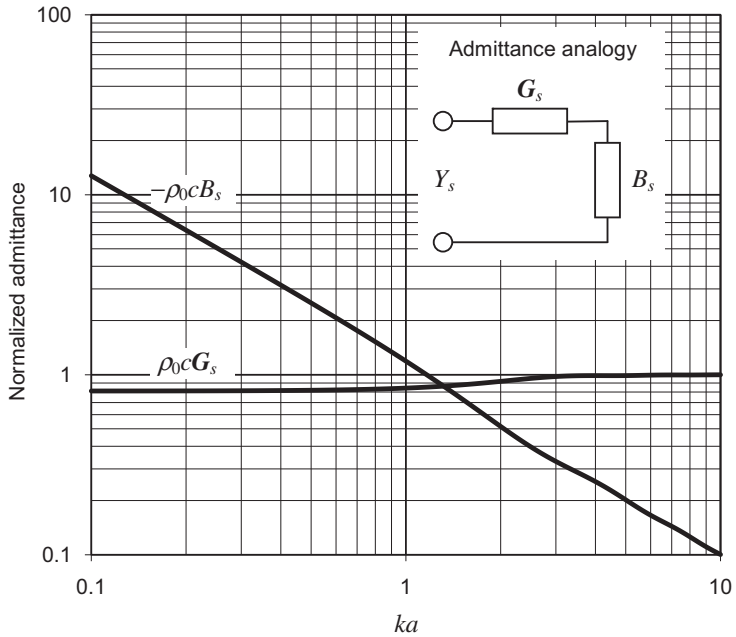

FIG. 13.19 Real and imaginary parts of the normalized specific radiation admittance $\rho_0 c Y_s$ of the air load on one side of a plane circular resilient disk of radius a in an infinite baffle.

Frequency is plotted on a normalized scale, where $ka = 2\pi a/\lambda = 2\pi fa/c$.

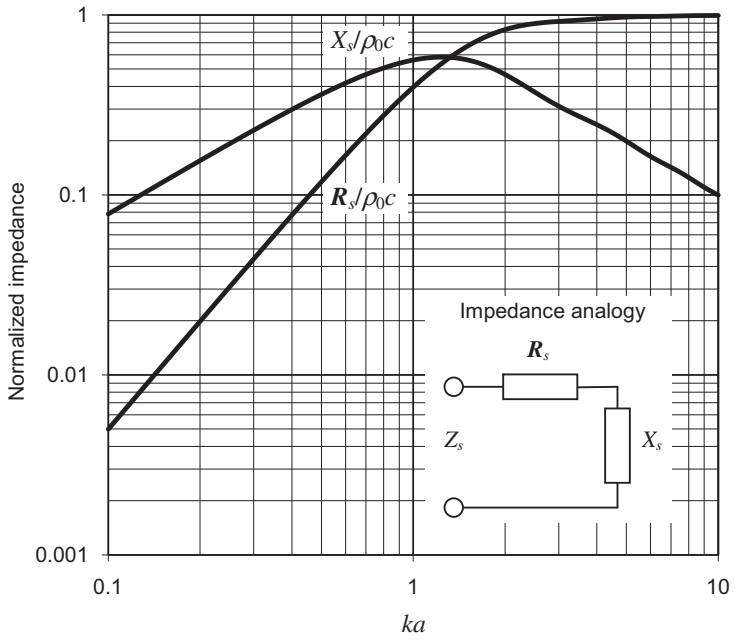

FIG. 13.20 Real and imaginary parts of the normalized specific radiation impedance $Z_s/\rho_0 c$ of the air load on one side of a plane circular resilient disk of radius a in an infinite baffle.

Frequency is plotted on a normalized scale, where $ka = 2\pi a/\lambda = 2\pi fa/c$.

13.10 RADIATION FROM A RIGID CIRCULAR PISTON IN A FINITE CIRCULAR OPEN BAFFLE [23, 24]

A disk in a circular baffle is a useful model for an open-baffle type loudspeaker and in the limiting case a loudspeaker without a baffle of any sort. Loudspeaker drive units are often measured in a finite baffle such as the rectangular IEC 268-5 baffle. See IEC 60268-5, ed. 3.1, "Sound system equipment - Part 5: Loudspeakers," available from http://webstore.iec.ch/. For example, for a nominal 8-in (200 mm) diameter loadspeaker, the baffle size would be 1.65 m long by 1.35 m wide, with the loadspeaker offset from the center by 22.5 cm lengthways and 15 cm widthways. If we have a rigorous model of the baffle, we can subtract its diffraction effects from the measurement in order to reveal the true response of the drive unit. The problem was first solved by Nimura and Watanabe [25] using the boundary value method in the oblate-spheroidal coordinate system. However, oblate-spheroidal functions are rather complicated, so instead we shall use the boundary integral method with the Green's function in cylindrical coordinates and a trial function first used by Streng [22] for a membrane. Previous solutions for the limiting case of a disk in free space have been obtained by Bouwkamp [20] using the boundary value method and Sommerfeld [26] using the boundary integral method in cylindrical coordinates. Meixner and Fritze [27] plotted the near-field pressure, a formidable task without the benefit of modern computing power, and Wiener [28] plotted the far-field directivity pattern.

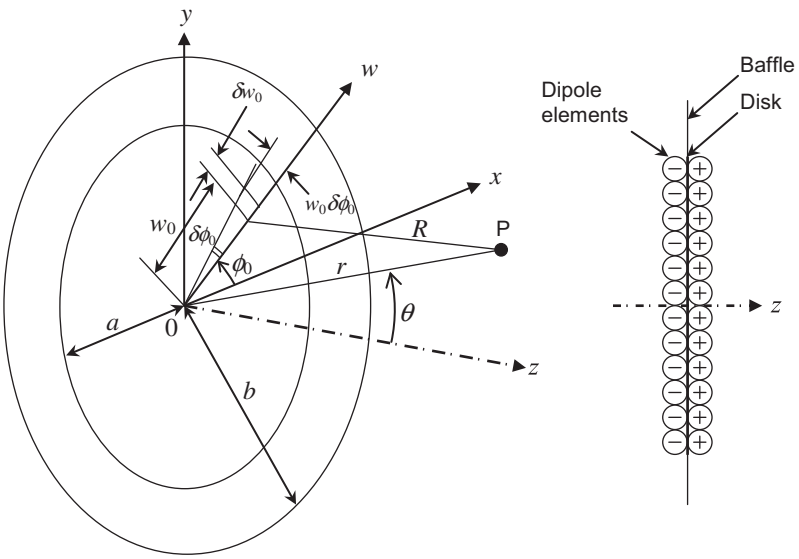

FIG. 13.21 Geometry of rigid circular piston in finite baffle.

The point of observation P is located at a distance r and angle θ with respect to the origin at the center of the piston.

Boundary conditions. The circular piston of radius a shown in Fig. 13.21 is mounted in a finite circular baffle of radius b in the xy plane with its center at the origin and oscillates in the z direction with a harmonically time-dependent velocity $\tilde{u}_0$, thus radiating sound from both sides into a homogeneous loss-free medium. The dipole source elements shown in Fig. 13.21 form the piston source. The area of each surface element is given by

$$\delta S_0 = w_0 \delta w_0 \delta\phi_0. \tag{13.197}$$

The pressure field on one side of the xy plane is the symmetrical "negative" of that on the other, so that

$$\tilde{p}(w,z) = -\tilde{p}(w,-z). \tag{13.198}$$

Consequently, there is a Dirichlet boundary condition in the plane of the disk where these equal and opposite fields meet:

$$\tilde{p}(w,0) = 0, \qquad b < w \leq \infty, \tag{13.199}$$

which is satisfied automatically. On the front and rear surfaces of the baffle, there is a Neumann boundary condition

$$\frac{\partial}{\partial z}\tilde{p}(w,z)\Big|_{z=0\pm} = 0, \qquad a < w \leq b. \tag{13.200}$$

Also, on the front and rear surfaces of the disk, there is the coupling condition

$$\frac{\partial}{\partial z}\tilde{p}(w,z)\Big|_{z=0\pm} = -jk\rho_0 c\tilde{u}_0, \qquad 0 \leq w \leq a, \tag{13.201}$$

where k is the wave-number given by $k = \omega/c = 2\pi/\lambda$, ω is the angular frequency of excitation, ρ_0 is the density of the surrounding medium, c is the speed of sound in that medium, and λ is the wavelength. In order to tackle this problem, we shall use the *dipole* surface integral of Eq. (13.28). However, some prior expression for the frontal surface pressure distribution $\tilde{p}_+(w_0)$ is needed. Also, because the disk can radiate from both sides, the rear surface pressure distribution $\tilde{p}_-(w_0)$ must be included too, where $\tilde{p}_+(w_0) = -\tilde{p}_-(w_0)$. Streng [22] showed that the surface pressure distribution for any flat axially-symmetric unbaffled source (or sink), based upon Bouwkamp's solution [20] to the free-space wave equation in oblate-spheroidal coordinates, could be written as

$$\tilde{p}_+(w_0) = -\tilde{p}_-(w_0) = kb\rho_0 c\tilde{u}_0 \frac{a^2}{b^2} \sum_{n=0}^{\infty} A_n \left(n + \frac{3}{2}\right) \left(1 - \frac{w_0^2}{b^2}\right)^{n+\frac{1}{2}}, \qquad 0 \le w_0 \le b. \tag{13.202}$$

where A_n are the as-yet unknown power series coefficients which will be evaluated by means of a set of simultaneous equations in matrix form.

Formulation of the coupled equation. The near-field pressure distribution is given by the boundary integral of Eq. (13.28) taking into account the surface pressure on both sides:

$$\tilde{p}(w,z) = \int_0^{2\pi} \int_0^b (\tilde{p}_+(w_0) - \tilde{p}_-(w_0)) \frac{\partial}{\partial z_0} g(w,z|w_0,z_0)|_{z_0=0+} w_0 dw_0 d\phi_0, \tag{13.203}$$

where the integral Green's function in cylindrical coordinates given by Eq. (13.52) is used. In this form Eq. (13.203) is known as the dipole King integral. Inserting Eqs. (13.52), (13.198), and (13.202) into Eq. (13.203) and integrating over the surface of the piston and baffle using Eq. (96) from Appendix II gives

$$\tilde{p}(w,z) = -ka^2\rho_0 c\tilde{u}_0 \sum_{n=0}^{\infty} A_n \Gamma\left(n + \frac{5}{2}\right) \int_0^{\infty} \left(\frac{2}{k_w b}\right)^{n+\frac{1}{2}} J_0(k_w w) J_{n+\frac{3}{2}}(k_w b) e^{-jk_z|z|} dk_w, \tag{13.204}$$

where k_z is given by Eq. (13.51). At the surface of the disk, we have the coupling condition

$$\frac{\partial}{\partial z}\tilde{p}(w,z)\Big|_{z=0} = -jk\rho_0 c\tilde{u}_0 \Phi(w) \tag{13.205}$$

where $\Phi(w)$ is a dimensionless function of the surface velocity distribution. We will use different expressions for $\Phi(w)$ when considering a piston in free space and a piston or point source in a circular baffle This leads to the following coupled equation:

$$\sum_{n=0}^{\infty} A_n I_n(w) = -\Phi(w), \tag{13.206}$$

which is to be solved for the power series coefficients A_n. The integral $I_n(w)$ can be split into two parts:

$$I_n(w) = I_{nR}(w) - jI_{nI}(w), \tag{13.207}$$

where the real part is given by

$$I_{nR}(w) = a^2\Gamma\left(n+\frac{5}{2}\right)\int_0^k \left(\frac{2}{k_w b}\right)^{n+\frac{1}{2}} J_{n+\frac{3}{2}}(k_w b)J_0(k_w w)\sqrt{k^2-k_w^2}\,dk_w \tag{13.208}$$

and the imaginary part is given by

$$I_{nI}(w) = a^2\Gamma(n+\frac{5}{2})\int_k^\infty \left(\frac{2}{k_w b}\right)^{n+\frac{1}{2}} J_{n+\frac{3}{2}}(k_w b)J_0(k_w w)\sqrt{k_w^2-k^2}\,dk_w. \tag{13.209}$$

These integrals can be shown [29,23] to be given by

$$I_{nR}(w) = \sqrt{\pi}\,\frac{a^2}{b^2}\sum_{m=0}^{\infty}\sum_{r=0}^{\infty}\frac{(-1)^{m+r}\Gamma\left(n+\frac{5}{2}\right)\Gamma(m+r+1)}{(m!)^2 r!\Gamma\left(r+n+\frac{5}{2}\right)\Gamma\left(m+r+\frac{5}{2}\right)}\left(\frac{kb}{2}\right)^{2(m+r)+3}\left(\frac{w}{b}\right)^{2m}, \tag{13.210}$$

$$I_{nI}(w) = \sqrt{\pi}\,\frac{a^2}{b^2}\sum_{m=0}^{\infty}\sum_{r=0}^{\infty}\frac{(-1)^{m+r+n}\Gamma\left(n+\frac{5}{2}\right)\Gamma\left(m+r-n-\frac{1}{2}\right)}{(m!)^2 r!\Gamma\left(r-n-\frac{1}{2}\right)\Gamma(m+r-n+1)}\left(\frac{kb}{2}\right)^{2(m+r-n)}\left(\frac{w}{b}\right)^{2m}. \tag{13.211}$$

Solution of the power series coefficients for a piston in free space. Equations (13.210) and (13.211) are both expansions in $(w/b)^{2m}$. Hence, in order to solve for the expansion coefficients, it is useful to express the disk and baffle velocity distribution $\Phi(w)$ as a function of $(w/b)^{2m}$. In the case of a disk in free space where $b = a$, we have

$$\Phi(w)|_{b=a} = 1 = \sum_{m=0}^{\infty}\delta_{m0}\left(\frac{w}{a}\right)^{2m}, \qquad 0 \le w \le a, \tag{13.212}$$

where δ_{m0} is the Kronecker delta function. Inserting Eqs. (13.207), (13.210), (13.211), and (13.212) in Eq. (13.206) and equating the coefficients of $(w/a)^{2m}$ yields the $(N+1)\times(N+1)$ matrix equation

$$\mathbf{M}\cdot\mathbf{a} = \mathbf{b}, \tag{13.213}$$

where the matrix $\mathbf{M}$ and vectors $\mathbf{a}$ and $\mathbf{b}$ are given by

$$\mathbf{M}(m+1,n+1) = {}_n\mathbf{B}_m(ka) - j_n\mathbf{S}_m(ka), \qquad \begin{cases} m = 0,1,\cdots,N \\ n = 0,1,\cdots,N \end{cases}, \tag{13.214}$$

$$\mathbf{b}(m+1) = -\delta_{m0}, \qquad m = 0,1,\cdots,N, \tag{13.215}$$

$$\mathbf{a}(n+1) = A_n, \qquad n = 0,1,\cdots,N, \tag{13.216}$$

and the infinite power series limits have been truncated to order N. The dipole cylindrical wave functions ${}_n\mathbf{B}_m$ and ${}_n\mathbf{S}_m$ are named the Bouwkamp and Streng functions respectively in tribute to their pioneering work and are defined by

$$ {}_n\mathbf{B}_m(ka) \;=\; \sqrt{\pi}\sum_{r=0}^{N}\frac{(-1)^{m+r}\Gamma\left(n+\frac{5}{2}\right)\Gamma(m+r+1)}{(m!)^2 r!\Gamma\left(r+n+\frac{5}{2}\right)\Gamma\left(m+r+\frac{5}{2}\right)}\left(\frac{ka}{2}\right)^{2(m+r)+3}, \tag{13.217} $$

$$ {}_n\mathbf{S}_m(ka) \;=\; \sqrt{\pi}\sum_{r=0}^{N}\frac{(-1)^{m+r+n}\Gamma\left(n+\frac{5}{2}\right)\Gamma\left(m+r-n-\frac{1}{2}\right)}{(m!)^2 r!\Gamma\left(r-n-\frac{1}{2}\right)\Gamma(m+r-n+1)}\left(\frac{ka}{2}\right)^{2(m+r-n)}. \tag{13.218} $$

Solution of the power series coefficients for a piston in a circular baffle. For a finite baffle, where $b \neq a$, we can employ the following *least-mean-squares* (LMS) algorithm. From Eq. (13.206), let an error function be defined by

$$ E(A_n) \;=\; \int_0^b \left|\sum_{n=0}^{N} A_n I_n(w) + \Phi(w)\right|^2 w dw. \tag{13.219} $$

where

$$ \Phi(w) \;=\; \begin{cases} 1, & 0 \le w \le a \\ 0, & a < w \le b, \end{cases} \tag{13.220} $$

In order to find the values of A_n that minimize the error, we take the derivative of E with respect to A_n and equate the result to zero:

$$ \frac{\partial}{\partial A_n}E(A_n) \;=\; 2\int_0^b I_m^*(w)\left(\sum_{n=0}^{N} A_n I_n(w) + \Phi(w)\right) w dw \;=\; 0, \tag{13.221} $$

which, after truncating the infinite series limit to order N, yields the following set of $N+1$ simultaneous equations:

$$ \sum_{n=0}^{\infty} A_n \int_0^b I_m^*(w) I_n(w) w dw \;=\; -\int_0^a I_m^*(w) w dw, \qquad m \;=\; 0, 1, \cdots N, \tag{13.222} $$

where

$$ I_m^*(w) \;=\; \frac{a^2}{b^2}\sum_{p=0}^{P}\left({}_m\boldsymbol{B}_p(kb) + j_m\mathbf{S}_p(kb)\right)\left(\frac{w}{b}\right)^{2p}, \tag{13.223} $$

$$I_n(w) = \frac{a^2}{b^2}\sum_{q=0}^{Q}\left({}_n\mathbf{B}_q(kb) - j_n\mathbf{S}_q(kb)\right)\left(\frac{w}{b}\right)^{2q}. \tag{13.224}$$

Integrating over w yields the following $(N+1)\times(N+1)$ matrix equation:

$$\mathbf{M}\cdot\mathbf{a} = \mathbf{b}, \tag{13.225}$$

where the matrix $\mathbf{M}$ and vectors $\mathbf{a}$ and $\mathbf{b}$ are given by

$$\begin{aligned}\mathbf{M}(m+1,n+1) = &\sum_{p=0}^{P}\sum_{q=0}^{Q}\frac{\left({}_m\boldsymbol{B}_p(kb) + j\,{}_mS_p(kb)\right)}{p+q+1}\\ &\times\left({}_n\mathbf{B}_q(kb) - j_n\mathbf{S}_q(kb)\right), \quad \begin{cases} m = 0,1,\cdots,N \\ n = 0,1,\cdots,N \end{cases},\end{aligned} \tag{13.226}$$

$$\mathbf{b}(m+1) = -\sum_{p=0}^{P}\frac{\left({}_mB_p(kb) + j\,{}_m\boldsymbol{S}_p(kb)\right)}{p+1}\left(\frac{a}{b}\right)^{2p}, \qquad m = 0,1,\cdots,N, \tag{13.227}$$

$$\mathbf{a}(n+1) = A_n, \qquad n = 0,1,\cdots,N. \tag{13.228}$$

Solution of the power series coefficients for a point or ring source in a circular baffle. In the case of a ring source of radius a in a circular baffle, we have

$$\Phi(w) = \frac{a}{2}\delta(w-a), \tag{13.229}$$

where δ is the Dirac delta function. Inserting this into Eq. (13.221) and truncating the infinite series limit to order N, yields the following set of $N + 1$ simultaneous equations:

$$\sum_{n=0}^{N}A_n\int_0^b I_m(w)I_n(w)wdw = -\frac{a}{2}\int_0^b \delta(w-a)I_m(w)wdw, \qquad m = 0,1,\cdots N, \tag{13.230}$$

where $I_m(w)$ and $I_n(w)$ are given by Eqs. (13.223) and (13.224) respectively. Integrating over w and using the property of the Dirac delta function yields the same matrix equations as Eqs. (13.225) to (13.228) except that

$$\mathbf{b}(m+1) = -\sum_{p=0}^{P}\left({}_m\boldsymbol{B}_p(kb) + j\,{}_m\boldsymbol{S}_p(kb)\right)\left(\frac{a}{b}\right)^{2p}. \tag{13.231}$$

In the limiting case of a point source at the center of a circular baffle, we let $a \to 0$ so that

$$\mathbf{b}(m+1) = -{}_m\mathbf{B}_0(kb) - j_m\mathbf{S}_0(kb). \tag{13.232}$$

Now that we have the surface velocity series coefficients A_n, we can derive some radiation characteristics for the disk in free space or open circular baffle or a point source in a circular baffle.

Far-field pressure. The far-field pressure distribution is given by the dipole boundary integral of Eq. (13.28), taking into account the surface pressure on both sides:

$$\tilde{p}(r,\theta) = \int_0^{2\pi}\int_0^{b}\left(\tilde{p}_+(w_0)-\tilde{p}_-(w_0)\right)\frac{\partial}{\partial z_0}g(r,\theta|w_0,\phi_0)|_{z_0=0+}w_0 dw_0 d\phi_0, \tag{13.233}$$

where the far-field Green's function in spherical-cylindrical coordinates given by Eq. (13.70) is used. Inserting Eqs. (13.70), (13.198), and (13.202) into Eq. (13.233) and integrating over the surface, using Eqs. (76) and (96) from Appendix II [with $z = kw_0 \sin\theta$, $b = k \sin\theta$, and letting $\phi = \pi/2$ so that $\cos(\phi - \phi_0) = \sin\phi_0$], gives

$$\tilde{p}(r,\theta) = -jka^2\rho_0 c\tilde{u}_0\frac{e^{-jkr}}{2r}D(\theta), \tag{13.234}$$

where the directivity function $D(\theta)$ is given by

$$D(\theta) = kb\cos\theta\sum_{n=0}^{N}A_n\Gamma\left(n+\frac{5}{2}\right)\left(\frac{2}{kb\sin\theta}\right)^{n+\frac{3}{2}}J_{n+\frac{3}{2}}(kb\sin\theta). \tag{13.235}$$

The on-axis pressure is evaluated by setting $\theta = 0$ in Eq. (13.70) before inserting it into Eq. (13.233) and integrating over the surface to give

$$D(0) = kb\sum_{n=0}^{N}A_n, \tag{13.236}$$

so that the on-axis response can be written as

$$\tilde{p}(r,0) = -j\rho_0 f\tilde{U}_0\frac{e^{-jkr}}{r}kb\sum_{n=0}^{N}A_n. \tag{13.237}$$

where $\tilde{U}_0 = \pi a^2\tilde{u}_0$ is the total volume velocity. It is worth noting that in the unbaffled case, where $b = a$, $D(0)$ is simply the normalized radiation impedance, that is $D(0) = (\boldsymbol{R}_s + jX_s)/(\rho_0 c)$ where $\boldsymbol{R}_s$ and X_s are given by Eq. (13.249) and (13.250) respectively. Using standard curve-fitting methods, the following asymptotic expression can be written:

$$D(0) \approx j0.66\left(\frac{b}{a}-0.3\right)ka, \qquad kb < 0.5. \tag{13.238}$$

The on-axis response for five values of b is shown in Fig. 13.22, calculated from the magnitude of $D(0)$. We can see from Fig. 13.22 that, in the case of an unbaffled piston ($b = a$) radiating from both sides, the on-axis sound pressure falls at 6 dB/octave for small values of ka due to the decreasing path difference (as a proportion of wavelength λ) between the anti-phase rear radiation and the front radiation, which it partially cancels. This is also true of the oscillating sphere (see Fig. 4.26), but the attenuation is not as great due to the longer path difference around the sphere.

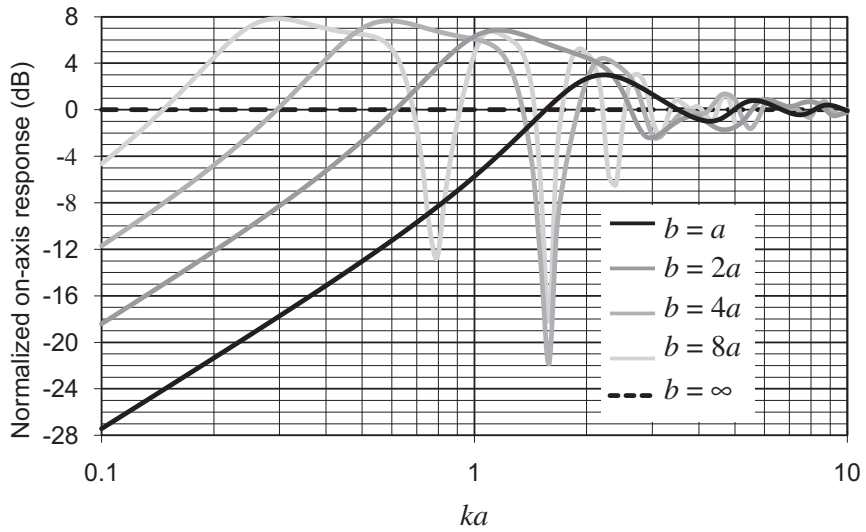

FIG. 13.22 Plot of 20 $\log_{10}(D(0))$ where $D(\theta)$ is the directivity function of a plane circular piston of radius a in a flat open circular baffle of radius b.

When $b = a$ (solid black curve), there is no baffle and the piston is radiating from both sides in free space. When $b = \infty$ (dotted black curve), the piston is in an infinite baffle. The axial acceleration of the piston is constant. Frequency is plotted on a normalized scale, where $ka = 2\pi a/\lambda = 2\pi fa/c$.

At larger values of ka, the rear radiation moves in and out of phase with that from the front. However, the comb-filter effect is fairly "smeared," the largest peak being 3 dB at $ka = \pi/\sqrt{2}$ (or $\lambda = 2\sqrt{2}\ a$), the reason being that rear radiation is due to the sum of many ring sources spread over the radius of the piston, each with a different path length to the front, so that at no particular frequency do they combine to produce a source that is either directly in phase or out of phase with that from the front. Unlike the oscillating sphere, the on-axis response does not roll-off at high frequencies, which is a property of planar sources, as already discussed in Sec. 12.8.

By contrast, when we include a circular baffle and increase its size, the actual radiating area decreases in proportion to the total so that it behaves more like a coherent point source at the center. Hence, when $b = 4a$, a deep null can be seen at $ka = \pi/2$ or $\lambda = 4a$, which is the distance from the center to the edge. Of course, a piston at the center of a circular baffle is the "worst case" and it would be interesting to compare these results with those of an offset piston in a circular, rectangular, or elliptical baffle, for example, in order to "smear" the path difference effect.

The normalized directivity function $20\ \log_{10}|D(\theta)/D(0)|$ for a piston in free space is plotted in Fig. 13.23 for four values of $ka = 2\pi a/\lambda$, that is, for four values of the ratio of the circumference of the disk to the wavelength. When the circumference of the piston ($2\pi a$) is less than one-half wavelength, that is, $ka < 0.5$, it behaves essentially like a dipole point source. In fact, to a first approximation, an unbaffled thin piston is simply a doublet, because an axial movement in one direction compresses the air on one side of it and causes a rarefaction of the air on the other side. When ka becomes greater than 3, the piston is highly directional, like the piston in an infinite baffle. Also, the directivity function for

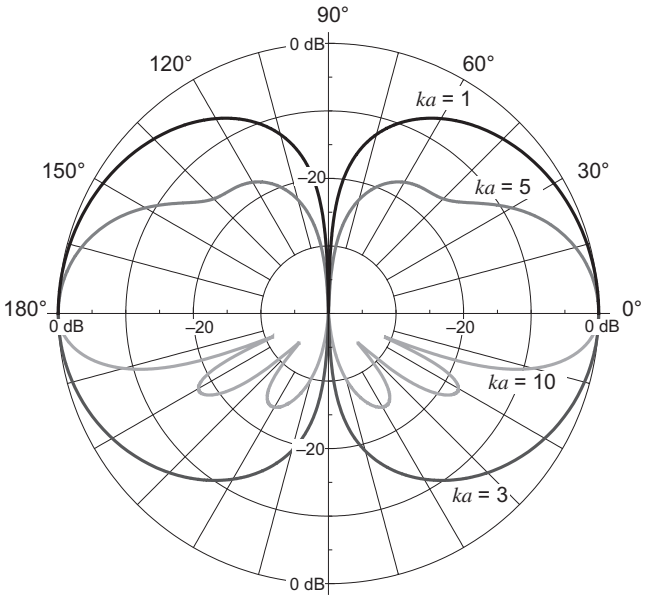

FIG. 13.23 Far-field directivity patterns for a plane circular piston radiating from both sides into free space as a function of $ka = 2\pi a/\lambda = \omega/c$, where a is the radius of the piston.

a piston in a finite open baffle is plotted in Fig. 13.24 for four values of ka with $b = 2a$ and in Fig. 13.25 for four values of b.

Near-field pressure. The near-field pressure distribution is given by Eq. (13.28) taking into account the surface pressure on both sides:

$$\tilde{p}(r,\theta) = \int_0^{2\pi}\int_0^{b} (\tilde{p}_+(w_0) - \tilde{p}_-(w_0)) \frac{\partial}{\partial z_0} g(r,\theta|w_0,\phi_0)|_{z_0=0+} w_0 dw_0 d\phi_0, \tag{13.239}$$

where the Green's function in spherical-cylindrical coordinates given by Eq. (13.68) is used. It has been shown [16] that inserting Eqs. (13.68), (13.198), and (13.202) into Eq. (13.239) and integrating over the surface gives

$$\tilde{p}(r,\theta) = 2jkb\rho_0 c\tilde{u}_0 \frac{a^2}{b^2} \sum_{n=0}^{N} A_n \sum_{p=0}^{P} \frac{(-1)^p \Gamma\left(p+\frac{3}{2}\right)\Gamma\left(n+\frac{5}{2}\right) h_{2p+1}^{(2)}(kr) P_{2p+1}(\cos\theta)}{\Gamma\left(2p+\frac{3}{2}\right)\Gamma\left(p+n+\frac{5}{2}\right)} \tag{13.240}$$

$$\times \left(\frac{kb}{2}\right)^{2p+2} {}_1F_2\left(p+1; p+n+\frac{5}{2}, 2p+\frac{5}{2}; -\frac{k^2b^2}{4}\right),$$

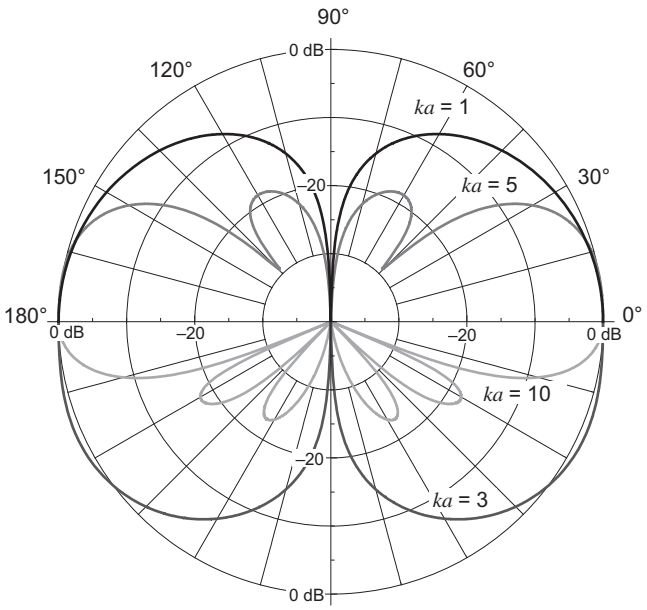

FIG. 13.24 Far-field directivity patterns for a circular piston in a plane open circular baffle as a function of $ka = 2\pi a/\lambda = \omega/c$, where a is the radius of the piston and $b = 2a$ is the radius of the baffle.

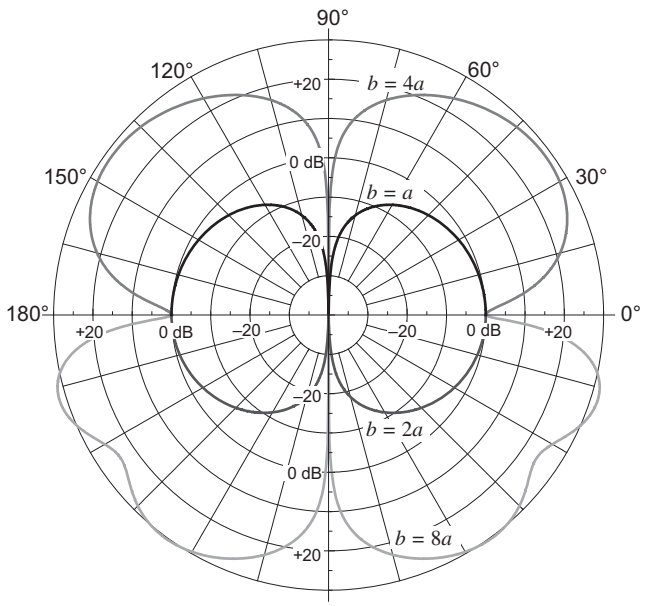

FIG. 13.25 Far-field directivity patterns for a circular piston in a plane open circular baffle as a function of b at $ka = \pi/2$ or $\lambda = 4a$, where a is the radius of the piston and b is the radius of the baffle.

which converges for $r > b$. For $r \leq b$, we derive a suitable expression from Eq. (13.204), which is weakly singular at $k_w = k$. However, we can remove this singularity as follows: Firstly, we substitute

$$k_w = k\sqrt{1-t^2} \text{ for } k_w \leq k$$

and

$$k_w = k\sqrt{1+t^2} \text{ for } k_w > k$$

in Eq. (13.204) to obtain

$$\tilde{p}(w,z) = k^2 a^2 \rho_0 c \tilde{u}_0 \sum_{n=0}^{\infty} A_n \Gamma\left(n+\frac{5}{2}\right)(I_{Fin}+I_{Inf}), \tag{13.241}$$

where

$$I_{Fin} = -\left(\frac{2}{kb}\right)^{n+\frac{1}{2}} \int_0^1 \left(\frac{1}{1-t^2}\right)^{\frac{n}{2}+\frac{3}{4}} J_{n+\frac{3}{2}}\left(kb\sqrt{1-t^2}\right) J_0\left(kw\sqrt{1-t^2}\right) e^{-jkzt} t dt, \tag{13.242}$$

$$I_{Inf} = -\left(\frac{2}{kb}\right)^{n+\frac{1}{2}} \int_0^{\infty} \left(\frac{1}{1+t^2}\right)^{\frac{n}{2}+\frac{3}{4}} J_{n+\frac{3}{2}}\left(kb\sqrt{1+t^2}\right) J_0\left(kw\sqrt{1+t^2}\right) e^{-kzt} t dt. \tag{13.243}$$

We then apply the expansion of Eq. (109) from Appendix II to give

$$\begin{aligned} I_{Fin}+I_{Inf} = &-\sum_{p=0}^{\infty} \frac{(-1)^p}{p!\Gamma\left(n+p+\frac{5}{2}\right)}\left(\frac{kb}{2}\right)^{2p+1} {}_2F_1\left(-p,-n-p-\frac{3}{2};1;\frac{w^2}{b^2}\right) \\ &\times\left(\int_0^1 (1-t^2)^p e^{-jkzt} t dt + \int_0^{\infty} (1+t^2)^p e^{-kzt} t dt\right), \end{aligned} \tag{13.244}$$

which after integrating yields

$$\begin{aligned} I_{Fin} = &\frac{\sqrt{\pi}}{2} \sum_{p=0}^{\infty} \frac{(-1)^p}{\Gamma\left(n+p+\frac{5}{2}\right)}\left(\frac{kb}{2}\right)^{2p+1} {}_2F_1\left(-p,-n-p-\frac{3}{2};1;\frac{w^2}{b^2}\right) \\ &\times\left\{\left(\frac{2}{kz}\right)^{p+\frac{1}{2}}\left(jJ_{p+\frac{3}{2}}(kz)+\mathbf{H}_{p+\frac{3}{2}}(kz)\right)-\frac{1}{\sqrt{\pi}(p+1)!}\right\}, \end{aligned} \tag{13.245}$$

$$I_{Inf} = \frac{\sqrt{\pi}}{2}\sum_{p=0}^{\infty}\frac{(-1)^p}{p!\Gamma\left(n+p+\frac{5}{2}\right)}\left(\frac{kb}{2}\right)^{2p+1}{}_2F_1\left(-p,-n-p-\frac{3}{2};1;\frac{w^2}{b^2}\right) \times\left\{\left(\frac{2}{kz}\right)^{p+\frac{1}{2}}\left(Y_{p+\frac{3}{2}}(kz)-\mathbf{H}_{p+\frac{3}{2}}(kz)\right)+\frac{1}{\sqrt{\pi}(p+1)!}\right\}. \tag{13.246}$$

Equation (13.245) converges everywhere and is therefore suitable for $r < b$. Unfortunately, Eq. (13.246) only converges for $z^2 > w^2 + b^2$ and is therefore not suitable. However, Eq. (13.243) converges everywhere and can be calculated numerically without problem and is therefore suitable for $r < b$. The pressure field of a rigid piston in free space is plotted in Fig. 13.26 for three values of ka. At $ka = 6\pi$, the sound field of the unbaffled piston shows similar characteristics to the baffled one, except that the radial pressure beyond its rim is zero, as with any planar dipole source. This suggests that, at high frequencies, objects either side of the source have less effect upon the sound field, except that the axial nulls are not as deep and the peaks are slightly higher. It can be shown that at low frequencies, where $ka < 1$, the on-axis pressure converges to the far-field approximation at increasingly greater distances due to the proximity effect (bass tip-up). The pressure field of a rigid piston in a circular baffle of radius $b = 2a$ is plotted in Fig. 13.27 for two values of ka.

Radiation impedance of a piston in a circular baffle. The total radiation force is found by integrating the pressure from Eq. (13.202) over the surface of the disk on both sides to give

$$\begin{aligned}\tilde{F} &= -\int_0^{2\pi}\int_0^{a}\left(\tilde{p}_+(w_0)-\tilde{p}_-(w_0)\right)w\,dw\,d\phi \\ &= -2\pi a^2\rho_0 c\tilde{u}_0\sum_{n=0}^{N}A_n\left\{1-\left(1-\frac{a^2}{b^2}\right)^{n+\frac{3}{2}}\right\}.\end{aligned} \tag{13.247}$$

The specific radiation impedance Z_s is then given by

$$Z_s = \frac{\tilde{F}}{\tilde{U}_0} = \boldsymbol{R}_s + jX_s, \tag{13.248}$$

where $\tilde{U}_0 = \pi a^2\tilde{u}_0$ is the total volume velocity and $\boldsymbol{R}_s$ is the specific radiation resistance in $\mathrm{N\cdot s/m^3}$ (rayl) given by

$$\boldsymbol{R}_s = kb\rho_0 c\Re\left(\sum_{n=0}^{N}A_n\left\{1-\left(1-\frac{a^2}{b^2}\right)^{n+\frac{3}{2}}\right\}\right), \tag{13.249}$$

where the bold $\boldsymbol{R}$ indicates that the quantity varies with frequency and X_s is the specific radiation reactance in $\mathrm{N\cdot s/m^3}$ (rayl) given by

$$X_s = kb\rho_0 c\Im\left(\sum_{n=0}^{N}A_n\left\{1-\left(1-\frac{a^2}{b^2}\right)^{n+\frac{3}{2}}\right\}\right). \tag{13.250}$$

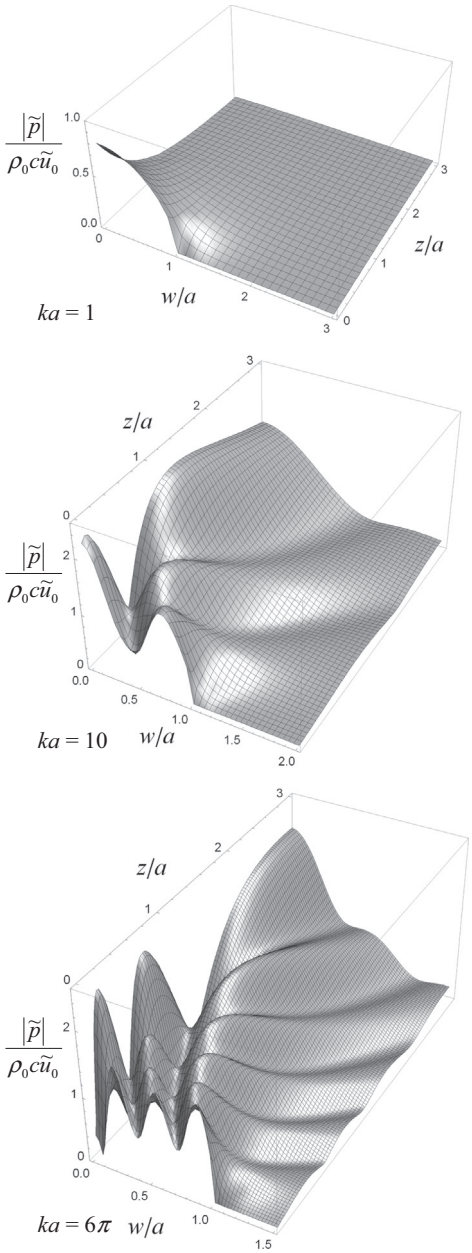

FIG. 13.26 Normalized near-field pressure plots for a rigid circular piston in free space as a function of $ka = 2\pi a/\lambda = 2\pi fa/c$, where a is the radius of the piston.

$|\tilde{p}|$ is the pressure magnitude, $\tilde{u}_0$ is the piston velocity, ρ_0 is the density of the acoustic medium, and c is the speed of sound in that medium.

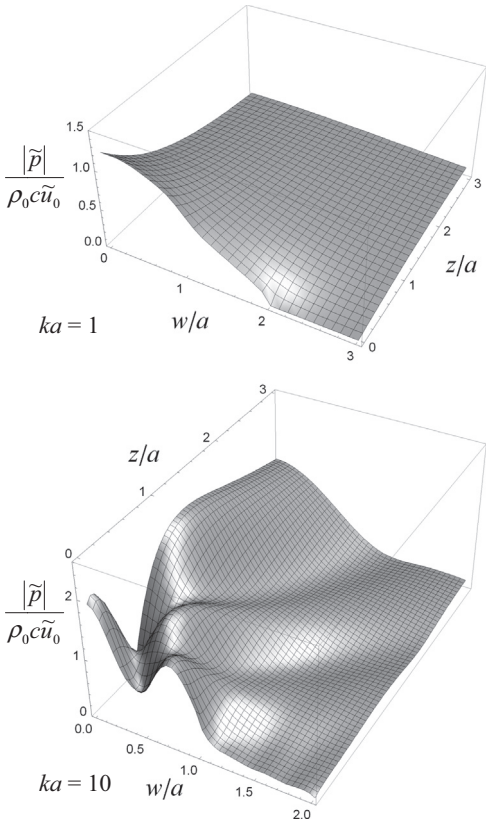

FIG. 13.27 Normalized near-field pressure plots for a rigid circular piston in a finite open circular baffle of radius $b = 2a$ as a function of $ka = 2\pi a/\lambda = 2\pi fa/c$, where a is the radius of the piston.

$|\tilde{p}|$ is the pressure magnitude, $\tilde{u}_0$ is the piston velocity, ρ_0 is the density of the acoustic medium, and c is the speed of sound in that medium.

Plots of the real and imaginary parts of

$$\frac{Z_s}{\rho_0 c} = \frac{\boldsymbol{R}_s + jX_s}{\rho_0 c} \tag{13.251}$$

are shown in Fig. 13.28 as a function of ka.

The data of Fig. 13.28 are used in dealing with impedance analogies. The complex admittance can be obtained by taking the reciprocal of the complex impedance.

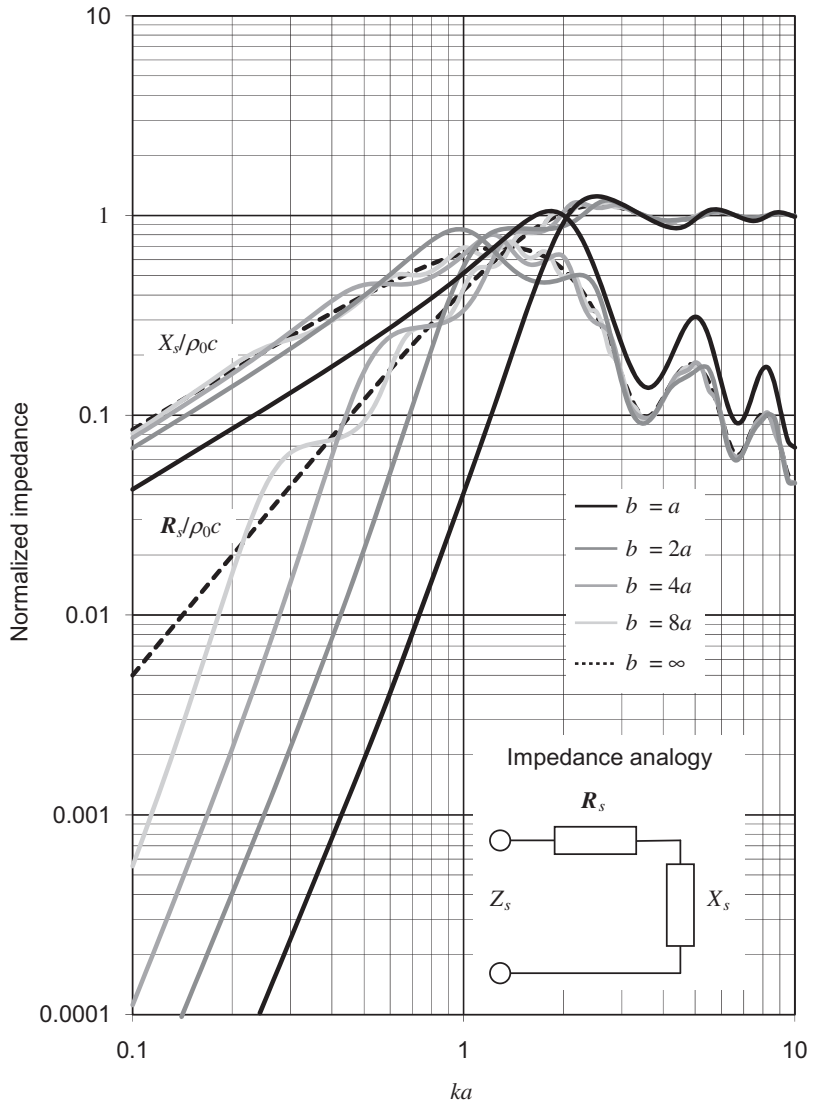

FIG. 13.28 Real and imaginary parts of the normalized specific radiation impedance $Z_s/\rho_0 c$ of the air load on one side of a plane circular piston of radius a in a flat circular open baffle of radius b.

When $b = a$ (solid black curve), there is no baffle and the piston is radiating from both sides into free space. When $b = \infty$ (dotted black curve), the piston is in an infinite baffle. Frequency is plotted on a normalized scale, where $ka = 2\pi a/\lambda = 2\pi fa/c$.

13.11 RADIATION FROM A RIGID CIRCULAR PISTON IN A FINITE CIRCULAR CLOSED BAFFLE [30] (ONE-SIDED RADIATOR)

The configuration is the same as that shown in Fig. 13.21 for a piston in an open baffle except that the velocity on the rear of the piston is zero. We can achieve this boundary condition by superposition of fields (or Gutin concept) whereby we combine the field of a piston in an open finite baffle with that of a piston in an infinite baffle. The former has negative velocity $-\tilde{u}_0$ on its rear surface whereas the latter, if treated as a "breathing" disk in free space, has positive velocity $\tilde{u}_0$ on its rear surface. Hence, when the two fields are combined, their rear surface velocities cancel to produce a zero velocity boundary condition as illustrated in Fig. 13.29. However, if we wish the front velocity to be $\tilde{u}_0$ and not $2\tilde{u}_0$, we must halve the result.

Although the piston and baffle are both infinitesimally thin in this model, it can be used to model a finite cylindrical enclosure with reasonably accuracy. In fact, the radiation characteristics of the single-sided piston without a baffle ($b = a$) are remarkably similar to those of a piston at the end of an infinite tube [31]. In the case of a finite cylinder, there will be secondary reflections from the far end but they will be considerably weaker than the primary ones from the rim of the baffle.

Far-field pressure. The directivity function $D(\theta)$ is half the sum of that from Eq. (13.102) for a piston in an infinite baffle and that from Eq. (13.235) for a piston in a finite open baffle:

$$D(\theta) = \frac{J_1(ka\sin\theta)}{ka\sin\theta} + \frac{kb}{2}\cos\theta\sum_{n=0}^{N} A_n\Gamma\left(n+\frac{5}{2}\right)\left(\frac{2}{kb\sin\theta}\right)^{n+\frac{3}{2}} J_{n+\frac{3}{2}}(kb\sin\theta). \tag{13.252}$$

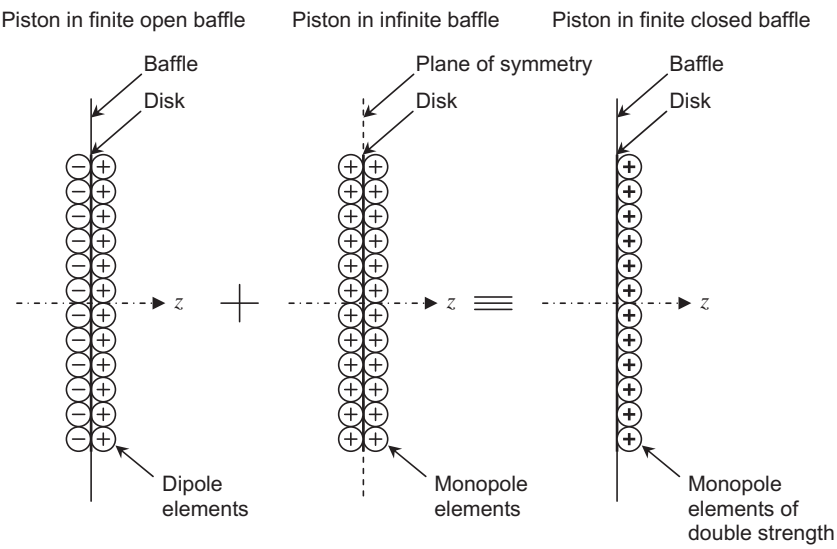

FIG. 13.29 Gutin concept: By superposition of fields, a one-sided piston in a finite closed baffle is equivalent to the sum of a double-sided dipole piston in a finite open baffle and a monopole piston in an infinite baffle. Also see Fig. 13.4 for the monopole piston model.

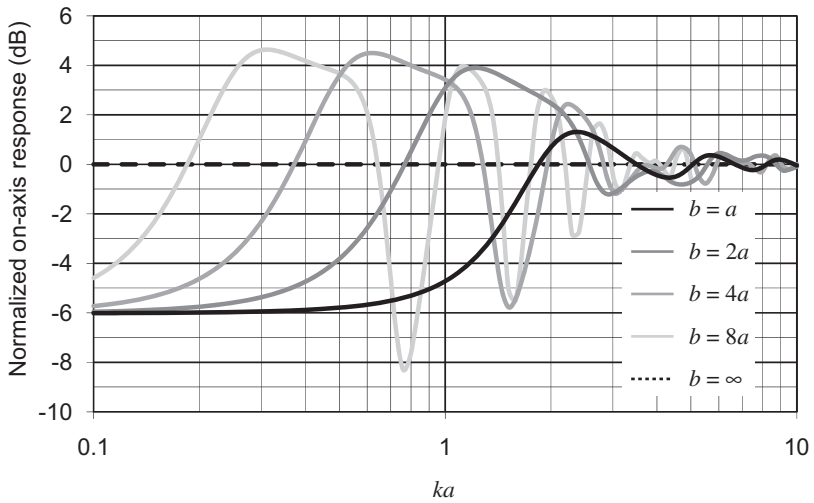

FIG. 13.30 Plot of 20 $\log_{10}(D(0))$ where $D(\theta)$ is the directivity function of a plane circular piston of radius a in a plane closed circular baffle of radius b.

When $b = a$ (solid black curve), there is no baffle and the piston is radiating from one side only in free space. When $b = \infty$ (dotted black curve), the piston is in an infinite baffle. The axial acceleration of the piston is constant. Frequency is plotted on a normalized scale, where $ka = 2\pi a/\lambda = 2\pi fa/c$.

Similarly, the on-axis pressure is obtained from Eqs. (13.103) and (13.236) to give

$$D(0) = \frac{1}{2}\left(1 + kb\sum_{n=0}^{N} A_n\right). \tag{13.253}$$

The on-axis response for five values of b is shown in Fig. 13.30, calculated from the magnitude of $D(0)$. The normalized directivity function $20\log_{10}|D(\theta)/D(0)|$ for a one-sided piston in free space is plotted in Fig. 13.31 for four values of $ka = 2\pi a/\lambda$, that is, for four values of the ratio of the circumference of the disk to the wavelength. Also, the directivity function for a piston in a finite closed baffle is plotted in Fig. 13.32 for four values of ka with $b = 2a$ and in Fig. 13.33 for four values of b.

Near-field pressure. The near-field pressure is simply the average of the pressures from Eqs. (13.106) and (13.240) for $r > a$ or Eqs. (13.107) and (13.241) for $r \leq a$. The pressure field for a one-sided piston in free space is plotted in Fig. 13.34 for three values of ka. The pressure response on the shadow side of the one-sided radiator is interesting not only for what it reveals about the diffraction effects around an infinitesimally thin edge, but also for the fact that this pressure field is actually the difference between the baffled (monopole) and unbaffled (dipole) responses of the rigid piston. In particular, the differences persist into the high-frequency range. The pressure field for a rigid circular piston in a closed circular baffle of radius $b = 2a$ is plotted in Fig. 13.35 for two values of ka.

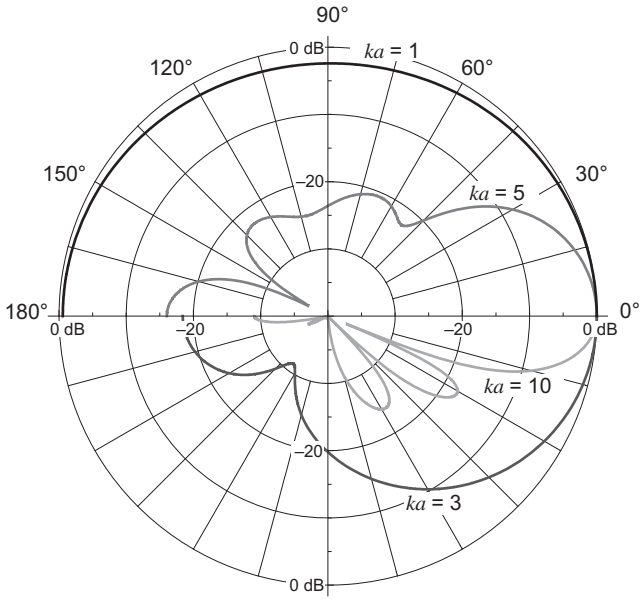

FIG. 13.31 Far-field directivity patterns for a plane circular piston radiating from one side only into free space as a function of $ka = 2\pi a/\lambda = \omega/c$, where a is the radius of the piston.

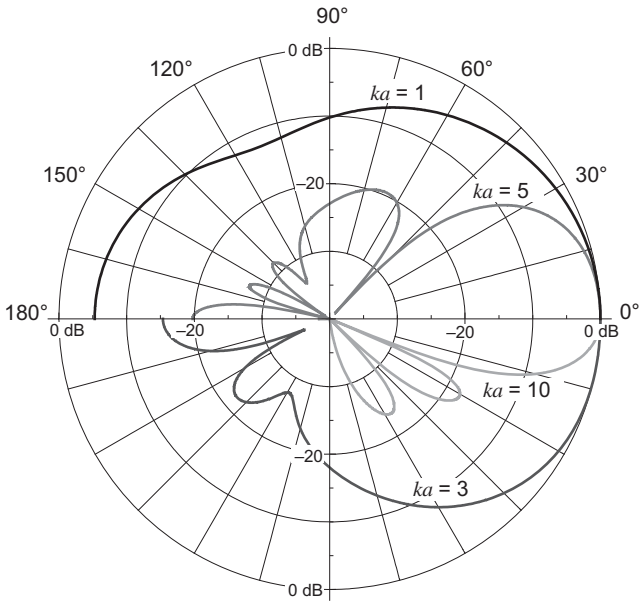

FIG. 13.32 Far-field directivity patterns for a circular piston in a plane closed circular baffle as a function of $ka = 2\pi a/\lambda = \omega/c$, where a is the radius of the piston and $b = 2a$ is the radius of the baffle.

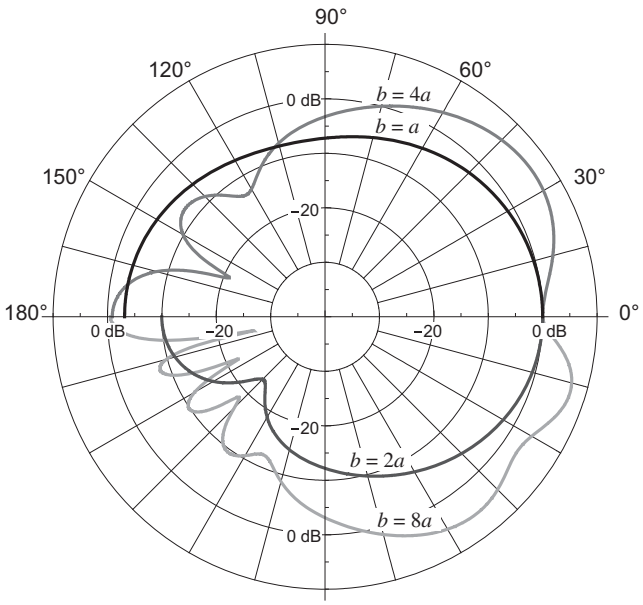

FIG. 13.33 Far-field directivity patterns for a circular piston in a plane closed circular baffle as a function of b at $ka = \pi/2$ or $\lambda = 4a$, where a is the radius of the piston and b is the radius of the baffle.

Radiation impedance. The same principle can also be applied to the radiation impedance, which is proportional to the sum of the surface pressures of a piston in a finite baffle and an infinite baffle. Hence the real part can be obtained from Eqs. (13.117) and (13.249) as follows:

$$\boldsymbol{R}_s = \frac{\rho_0 c}{2}\left\{1 - \frac{J_1(2ka)}{ka} + kb\Re\left(\sum_{n=0}^{N} A_n\left\{1 - \left(1 - \frac{a^2}{b^2}\right)^{n+\frac{3}{2}}\right\}\right)\right\}. \tag{13.254}$$

Likewise, the imaginary part can be obtained from Eqs. (13.118) and (13.250) as follows:

$$X_s = \frac{\rho_0 c}{2}\left\{\frac{\mathbf{H}_1(2ka)}{ka} + kb\Im\left(\sum_{n=0}^{N} A_n\left\{1 - \left(1 - \frac{a^2}{b^2}\right)^{n+\frac{3}{2}}\right\}\right)\right\}. \tag{13.255}$$

Plots of the real and imaginary parts of

$$\frac{Z_s}{\rho_0 c} = \frac{\boldsymbol{R}_s + jX_s}{\rho_0 c} \tag{13.256}$$

are shown in Fig. 13.36 as a function of ka.

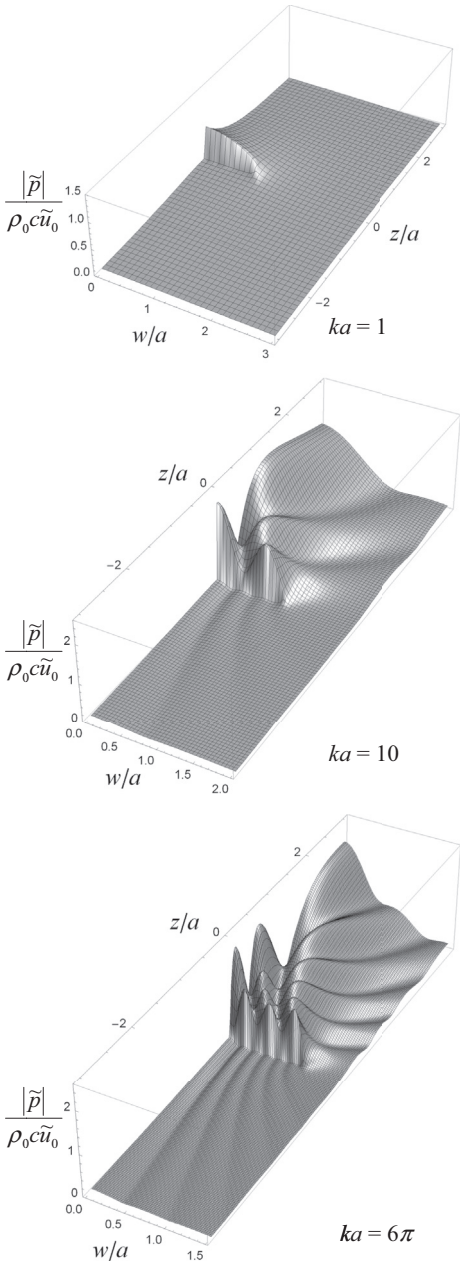

FIG. 13.34 Normalized near-field pressure plots for a rigid circular piston radiating from one side only into free space as a function of $ka = 2\pi a/\lambda = 2\pi fa/c$, where a is the radius of the piston.

$|\tilde{p}|$ is the pressure magnitude, $\tilde{u}_0$ is the piston velocity, ρ_0 is the density of the acoustic medium, and c is the speed of sound in that medium.

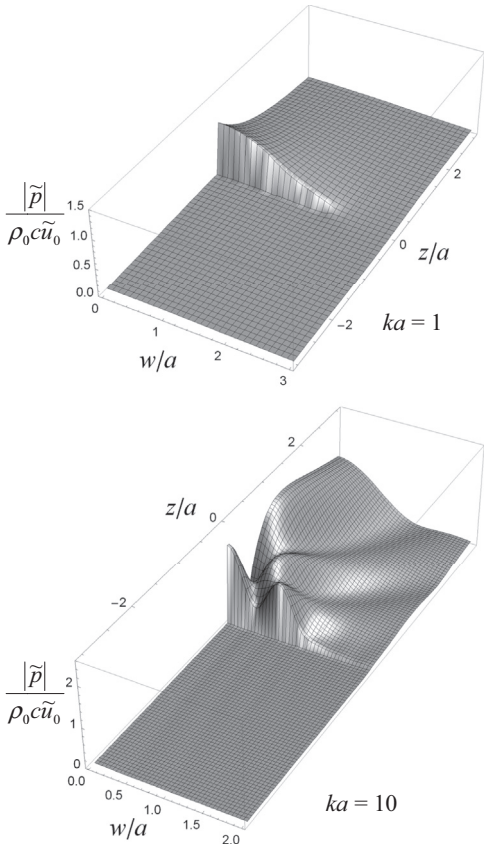

FIG. 13.35 Normalized near-field pressure plots for a rigid circular piston in a closed circular baffle of radius $b = 2a$ as a function of $ka = 2\pi a/\lambda = 2\pi fa/c$, where a is the radius of the piston.

$|\tilde{p}|$ is the pressure magnitude, $\tilde{u}_0$ is the piston velocity, ρ_0 is the density of the acoustic medium, and c is the speed of sound in that medium.

13.12 THE BABINET–BOUWKAMP PRINCIPLE

Kirchhoff theory. In its original form, Babinet's principle [32] simply states that the diffraction pattern resulting from the transmission of a plane wave through an aperture in an infinite screen is equivalent to that produced by the scattering of the same incident wave by the complementary disk. In the Kirchhoff theory of diffraction [33], it is assumed that the screen and complementary disk are either both rigid or both resilient, in which case the field scattered by an aperture in a rigid screen or complementary rigid disk can be represented by radiation from a rigid piston in an infinite baffle. Similarly, the field scattered by an aperture in a resilient screen or complementary resilient disk can be represented by radiation from a resilient disk in free space. If this were true, it would make life much simpler as everything could be calculated from closed-form solutions. The problem is that the former

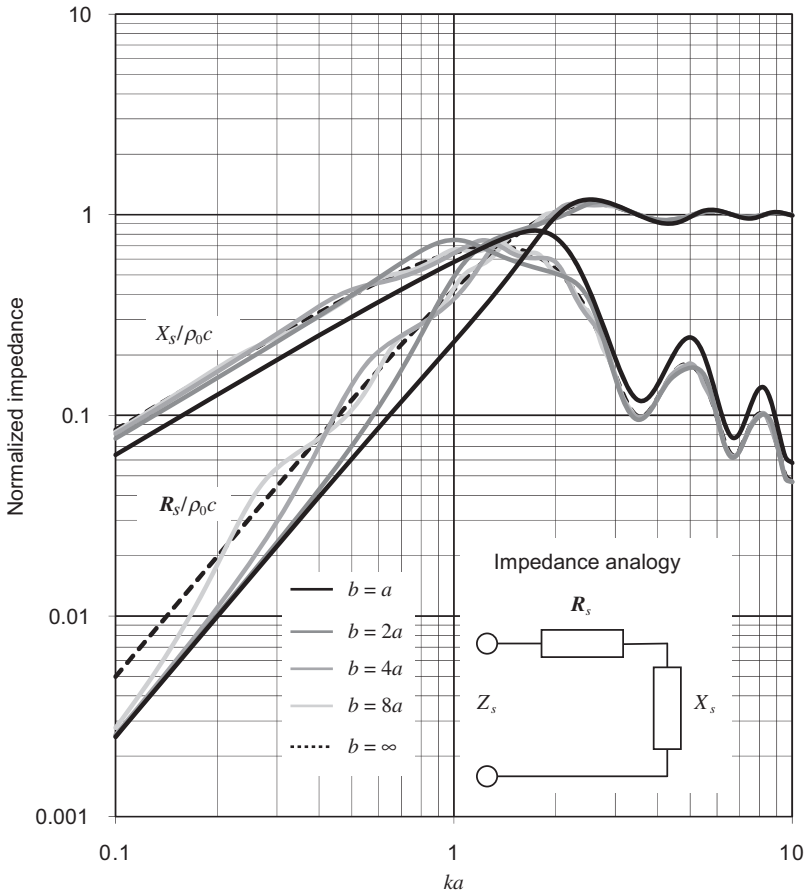

FIG. 13.36 Real and imaginary parts of the normalized specific radiation impedance $Z_s/\rho_0 c$ of the air load on one side of a plane circular piston of radius a in a flat circular closed baffle of radius b.

When $b = a$ (solid black curve), there is no baffle and the piston is radiating from one side only into free space. When $b = \infty$ (dotted black curve), the piston is in an infinite baffle. Frequency is plotted on a normalized scale, where $ka = 2\pi a/\lambda = 2\pi fa/c$.

assumes that the velocity of the scattered wave at the aperture or complementary rigid disk is the same as that of the incident wave, as if it were unaffected by the presence of the scattering object. Similarly, the latter assumes that the pressure of the scattered wave at the aperture or complementary resilient disk is the same as that of the incident wave. At best, this is an approximation [21] that can only be used when the wavelength is much smaller than the aperture or disk.

Bouwkamp theory. Bouwkamp's modified version [20] of Babinet's principle states that the diffraction pattern resulting from the transmission of a plane wave through an aperture in an infinite *rigid* screen (see Fig. 13.37c) is equivalent to that produced by the scattering of the same incident wave by the complementary *resilient* disk (see Fig. 13.37f). Also, the flip side of this is that the diffraction

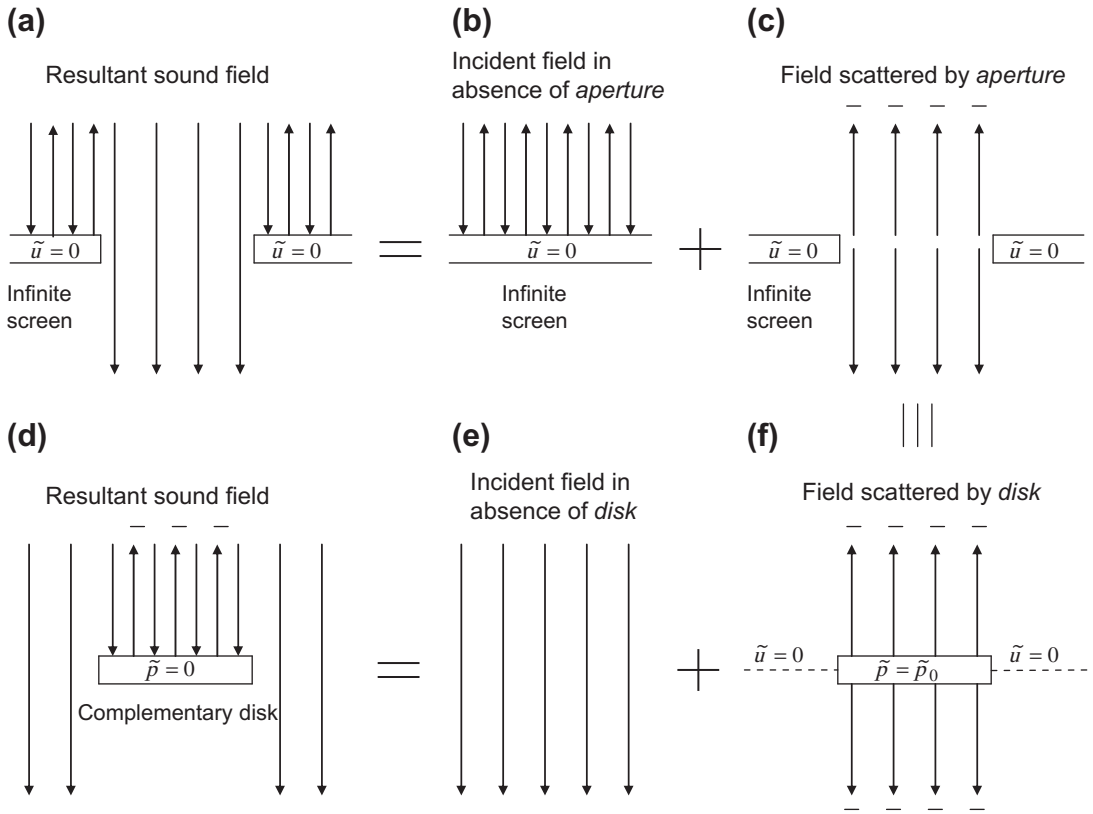

FIG. 13.37 The Babinet–Bouwkamp principle for a circular aperture in an infinite *rigid* screen.

pattern resulting from the transmission of a plane wave through an aperture in an infinite *resilient* screen (see Fig. 13.38c) is equivalent to that produced by the scattering of the same incident wave by the complementary *rigid* disk (see Fig. 13.38f). Furthermore, Bouwkamp states that:

- The sound field scattered by a *rigid* disk is equivalent to that produced if the disk itself were radiating in *free space*, provided that the *velocity* at the surface of the disk is equal to that of the incident plane wave in the absence of any scattering obstacle.
- The sound field scattered by a *resilient* disk is equivalent to that produced if the disk itself were radiating in *an infinite rigid baffle*, provided that the *pressure* at the surface of the disk is equal to that of the incident plane wave in the absence of any scattering obstacle.

The general principle is illustrated in Fig. 13.37 and Fig. 13.38, but before we discuss apertures, we will consider the scattering from plane objects.

Reflection from plane rigid objects [34]. We have already discussed the radiation of sound from moving surfaces using the boundary integral method. It often happens in acoustics that once you have found a solution for one problem, you get another for free. This is certainly the case with reflection

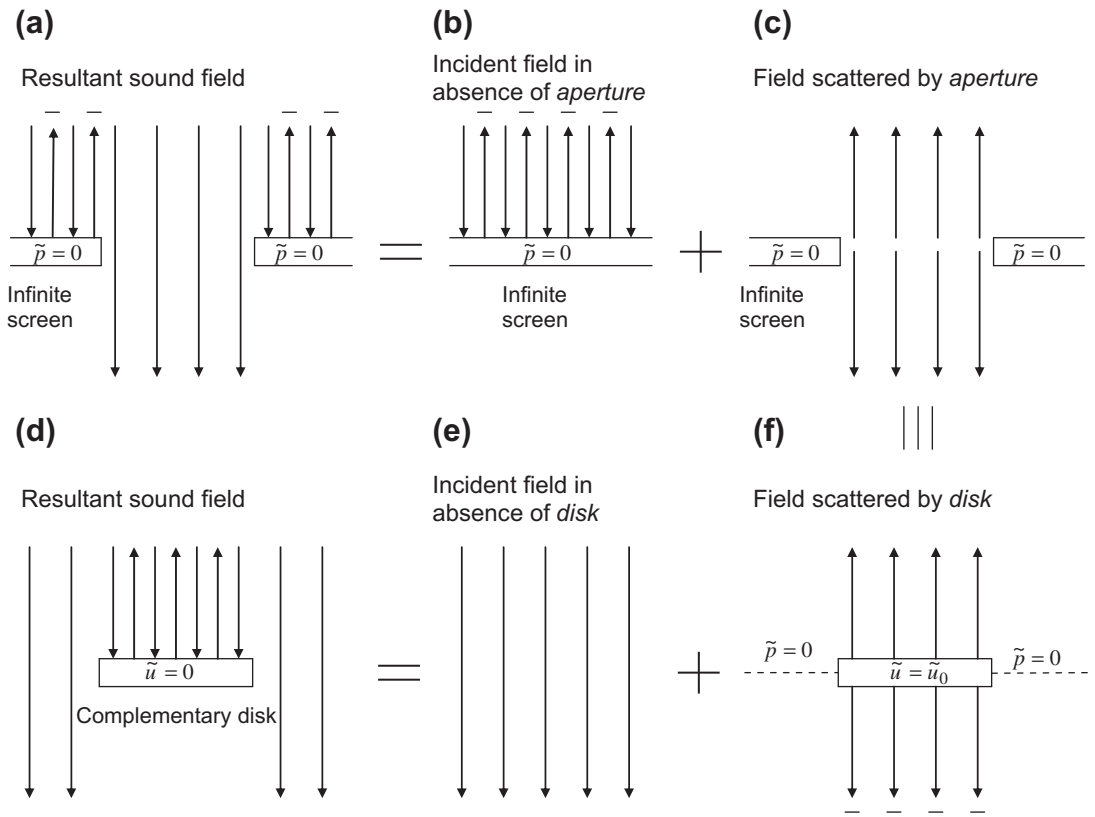

FIG. 13.38 The Babinet–Bouwkamp principle for a circular aperture in an infinite *resilient* screen.

from plane objects and here it will be shown how. Imagine a plane wave being reflected from an arbitrary rigid surface. At the surface, the normal velocity is zero. Now we let the resulting pressure field $\tilde{p}(\mathbf{r})$ comprise two components as follows:

$$\tilde{p}(\mathbf{r}) \;=\; \tilde{p}_I(\mathbf{r}) + \tilde{p}_S(\mathbf{r}), \tag{13.257}$$

where $\tilde{p}_I(\mathbf{r})$ is the incident wave in the absence of any obstacles and $\tilde{p}_S(\mathbf{r})$ is the scattered wave. In order to satisfy the boundary condition of zero normal velocity at the surface, the normal velocity of the surface producing the scattered wave must be equal and opposite to the component of the velocity of the incident wave that is normal to the surface. This is easiest to illustrate with a planar obstacle such as a circular disk in free space, as shown in Fig. 13.8 except that in this case it is perfectly rigid. Let $\tilde{p}_{ID}(z)$ be a simple plane incident wave travelling along the disk's axis of symmetry, which in this case is defined as the z-axis, and let the disk be located at $z = 0$. At the disk, the velocity, and hence also the gradient of the resultant field $\tilde{p}_D(z)$, are both zero:

$$\tilde{u}_0 \;=\; -ik\rho_0 c \frac{\partial}{\partial z}\tilde{p}_D(w,z)\Big|_{z=0} \;=\; 0, \qquad 0 \le w \le a, \tag{13.258}$$

where w is the radial ordinate and a is the radius of the disk. Also, from Eq. (13.257) and to preserve continuity, the resultant pressure gradient is the sum of the incident and scattered pressure gradients:

$$\frac{\partial}{\partial z}\tilde{p}_D(w,z)\Big|_{z=0} = \frac{\partial}{\partial z}\tilde{p}_{ID}(w,z)\Big|_{z=0} + \frac{\partial}{\partial z}\tilde{p}_{SD}(w,z)\Big|_{z=0} = 0, \qquad 0 \le w \le a. \tag{13.259}$$

Hence, the velocity $\tilde{u}_0$ of the disk is equal and opposite to the velocity $\tilde{u}_{ID}$ of the incident wave in the absence of any scattering obstacles:

$$\tilde{u}_0 = -ik\rho_0 c\frac{\partial}{\partial z}\tilde{p}_{SD}(w,z)\Big|_{z=0} = ik\rho_0 c\frac{\partial}{\partial z}\tilde{p}_{ID}(w,z)\Big|_{z=0} = -\tilde{u}_{ID}, \qquad 0 \le w \le a. \tag{13.260}$$

Therefore, the scattered field $\tilde{p}_{SD}(w,z)$ is that which would be produced if the disk were oscillating back and forth with the same velocity as the incident wave, but with opposite phase, and the resultant field $\tilde{p}_D(w,z)$ is the sum of the incident and scattered fields:

$$\tilde{p}_D(w,z) = \tilde{p}_{ID}(w,z) + \tilde{p}_{SD}(w,z), \tag{13.261}$$

as expressed in Fig. 13.38d, e, and f. However, we have to ask whether scattered field $\tilde{p}_{SD}(w,z)$ is the same as that of a disk in free space or one in an infinite baffle. In order to answer that, we have to consider another boundary condition, which lies in the plane of the disk beyond its rim. We can already assume that the field on one side of this plane will be the symmetrical negative of that on the other. This can be explained by the fact that on the "bright" side (facing the incident wave), the radiated sound represents the reflected sound, whereas on the "dark" side, it is of opposite phase and therefore cancels the incident wave that would otherwise be present in the absence of the disk. However, in a baffle, these equal and opposite pressure values either side of the baffle would produce a discontinuous field when added to the original incident wave. Therefore, the disk must behave as though it is oscillating in free space, thus producing a continuous field with zero pressure in the plane beyond its rim as shown in Fig. 13.38f. Hence, the resultant pressure in that region is simply that of the incident wave in the absence of any obstacles. The scattered field $\tilde{p}_{SD}(w,z)$ is that of a rigid disk oscillating in free space, which has already been evaluated in Sec. 13.10, using the dipole part of the Kirchhoff–Helmholtz boundary integral.

Reflection from plane resilient objects. In the case of a resilient disk in the presence of an incident plane wave traveling towards it along its axis of symmetry, the boundary condition at its surface is that of zero pressure:

$$\tilde{p}_D(w,z)\Big|_{z=0} = \tilde{p}_{ID}(w,z)\Big|_{z=0} + \tilde{p}_{SD}(w,z)\Big|_{z=0} = 0, \qquad 0 \le w \le a. \tag{13.262}$$

Hence, the pressure of the scattered field at the surface must be equal and opposite to the pressure of the incident wave in the absence of any scattering obstacles:

$$\tilde{p}_0 = \tilde{p}_{SD}(w,z)\Big|_{z=0} = -\tilde{p}_{ID}(w,z)\Big|_{z=0}, \qquad 0 \le w \le a. \tag{13.263}$$

Therefore, the scattered field $\tilde{p}_{SD}(w,z)$ is that which would be produced if the disk were in motion with the same pressure as the incident wave, but opposite phase, and the resultant field $\tilde{p}_D(w,z)$ is the sum of the incident and scattered fields:

$$\tilde{p}_D(w,z) = \tilde{p}_{ID}(w,z) + \tilde{p}_{SD}(w,z), \tag{13.264}$$

as expressed in Fig. 13.37d, e, and f. Furthermore, the scattered fields on each side of the disk are symmetrical and both of opposite polarity to the incident wave. This has the effect of creating a shadow on the "dark" side and reversing the phase of the reflected wave on the "bright" side due to the boundary condition of zero pressure, as opposed to zero velocity. If the boundary condition in the plane beyond the rim of the disk were one of zero pressure, the velocities on each side would be equal and opposite thus adding to and subtracting from the velocity of the incident wave on consecutive sides. This would in turn lead to a discontinuity in the velocity distribution of the resultant field at the plane. Hence, the scattered field is that of a resilient disk in an infinite baffle with symmetrical fields on each side, or a "breathing" resilient disk, which we have already evaluated in Sec. 13.9, using the monopole part of the Kirchhoff–Helmholtz boundary integral.

The Babinet–Bouwkamp principle for diffraction through a circular aperture in a rigid screen. Essentially, the boundary conditions for a circular aperture in an infinite rigid screen are the same as those for the complementary rigid disk in free space above and Fig. 13.38d, except that they are interchanged as shown in Fig. 13.37a. Hence, the resultant velocity is zero at the screen, which is the scattering obstacle, and the pressure in the aperture is the same as that of the incident wave in the absence of any scattering obstacles. However, whereas the rigid disk itself was treated as the source of the scattered wave, it is not so convenient to treat the infinite rigid screen as such. Instead, the aperture is treated as the source whereby the pressure is uniform everywhere within it and the aperture acts as a pressure source, namely a resilient disk in an infinite baffle, which we have already evaluated in Sec. 13.9, using the monopole part of the Kirchhoff–Helmholtz boundary integral, and satisfies the boundary condition of zero velocity on the screen. In order to calculate the resultant field on *both* sides of the screen, we simply add the scattered field to the incident field in the absence of an aperture, i.e., the incident plane wave plus its reflection from a continuous infinite rigid screen plus the radiation from the resilient disk. This is illustrated in Fig. 13.37a, b, and c. For clarity, the diagram portrays the scattering of a sound wave at some very high frequency where there is minimal diffraction. However, the principle applies at all frequencies. In general, for diffraction through a circular aperture in a rigid screen,

$$\tilde{p}_{IH}(z) = \begin{cases} \tilde{p}_0(e^{ikz} + e^{-ikz}), & \text{bright side of rigid screen} \\ 0, & \text{dark side of rigid screen} \\ \tilde{p}_0 e^{ikz}, & \text{without disk (or screen)} \end{cases} \tag{13.265}$$

and

$$\tilde{p}_{SH}(z) = \begin{cases} \tilde{p}_0, & z = 0+ \\ -\tilde{p}_0 & z = 0- . \end{cases} \tag{13.266}$$

These expressions are plotted in Fig. 13.39 for $ka = 1$, 5, and 10.

The Babinet–Bouwkamp principle for diffraction through a circular aperture in a resilient screen. Here we interchange the boundary conditions for a resilient disk in free space, described above. Hence, the resultant pressure is zero at the screen, which is the scattering obstacle, and the velocity in the aperture is the same as that of the incident wave in the absence of any scattering obstacles. The aperture is treated as the source, namely a rigid disk in free space, which we have

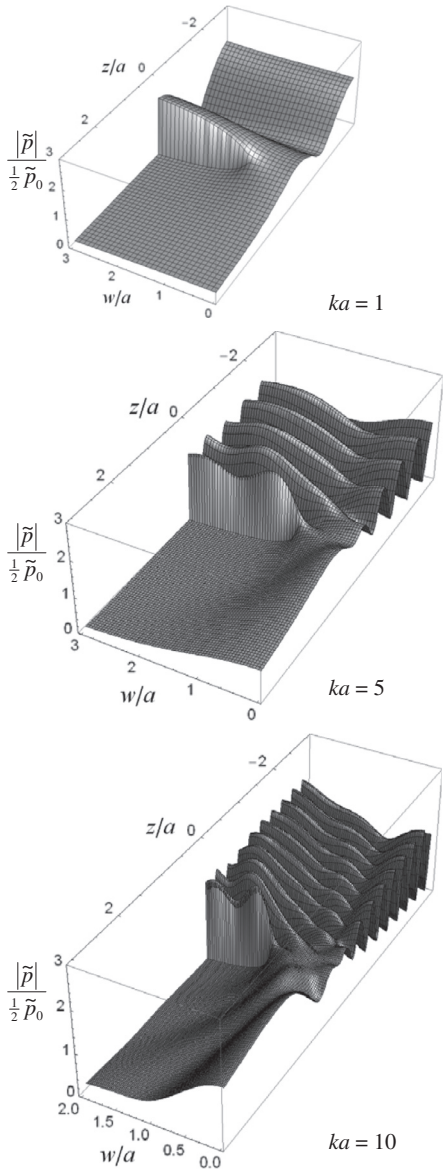

FIG. 13.39 Normalized plots of pressure field due to a plane wave diffracted through a circular hole in an infinite rigid screen as a function of $ka = 2\pi a/\lambda = 2\pi fa/c$, where a is the radius of the hole.

$|\tilde{p}|$ is the pressure magnitude, $\tilde{p}_0$ is the incident pressure at the hole in the absence of a screen, ρ is the density of the acoustic medium, and c is the speed of sound in that medium.

already evaluated in Sec. 13.10, using the dipole part of the Kirchhoff–Helmholtz boundary integral, and satisfies the boundary condition of zero pressure on the screen. In order to calculate the resultant field on *both* sides of the screen, we simply add the scattered field to the incident field in the absence of an aperture, i.e., the incident plane wave plus its reflection from a continuous infinite resilient screen plus the radiation from the rigid disk. This is illustrated in Fig. 13.38a, b, and c. For clarity, the diagram portrays the scattering of a sound wave at some very high frequency where there is minimal diffraction. However, the principle applies at all frequencies. In general, for diffraction through a circular aperture in a resilient screen,

$$\tilde{p}_{IH}(z) = \begin{cases} \tilde{p}_0(e^{ikz} - e^{-ikz}), & \text{bright side of resilient screen} \\ 0, & \text{dark side of resilient screen} \\ \tilde{p}_0 e^{ikz}, & \text{without disk (or screen)} \end{cases} \tag{13.267}$$

and

$$-ik\rho_0 c \left.\frac{\partial}{\partial z}\tilde{p}_{SH}(z)\right|_{z=0} = \tilde{u}_0. \tag{13.268}$$

PART XXXVII: RADIATION THEOREMS, RADIATION IN RECTANGULAR-SPHERICAL COORDINATES, MUTUAL IMPEDANCE

13.13 THE BOUWKAMP IMPEDANCE THEOREM [35]

In order to find the radiation impedance of a piston in an infinite baffle, we used an expression for the near-field pressure and integrated the pressure over the surface of the piston in order to find the total force. However, the far-field pressure is generally given by a much simpler expression. According to Bouwkamp's impedance theorem, if the acoustic medium is loss free, we can integrate the far-field pressure over a hemispherical surface (or spherical in the case of a whole-space radiator) and let the radius tend to infinity in order to obtain the radiation resistance. In general, the far-field pressure is given in spherical coordinates (r, θ, ϕ) by

$$\tilde{p}(r, \theta, \phi) = \frac{-jk\rho_0 c\tilde{U}_0}{2\pi r} D(\theta, \phi) \tag{13.269}$$

although, in the case of an axisymmetric source such as the circular piston, there is no ϕ dependency. The total radiated power W is given by

$$W = \frac{\left|\tilde{U}_0\right|^2}{2}\boldsymbol{R}_{AR} = \frac{1}{\rho_0 c}\int_0^{2\pi}\int_0^{\frac{\pi}{2}} \frac{\left|\tilde{p}(r, \theta, \phi)\right|^2}{2} r^2 \sin\theta \, d\theta \, d\phi\big|_{r\to\infty}, \tag{13.270}$$

where $\boldsymbol{R}_{AR}$ is the acoustic radiation impedance of the source and $\tilde{U}_0$ is its total volume velocity. Hence the specific radiation resistance is given by

$$\boldsymbol{R}_s = S\boldsymbol{R}_{AR} = \frac{k^2\rho_0 cS}{4\pi^2}\int_0^{2\pi}\int_0^{\frac{\pi}{2}} |D(\theta,\phi)|^2 \sin\theta \, d\theta \, d\phi. \tag{13.271}$$

Also, the specific radiation reactance is given by

$$X_s = SX_{AR} = -j\frac{k^2\rho_0 cS}{4\pi^2}\int_0^{2\pi}\int_{\frac{\pi}{2}+j0}^{\frac{\pi}{2}+j\infty} |D(\theta,\phi)|^2 \sin\theta \, d\theta \, d\phi. \tag{13.272}$$

It is fairly straightforward to verify this result by inserting the directivity function of Eq. (13.102) together with $k_w = k \sin\theta$ into Eqs. (13.271) and (13.272). In this way, the expressions for the radiation impedance given by Eqs. (13.118) and (13.117) can be duplicated, bearing in mind that $\sin(\pi/2+j\infty) = \cos j\infty = \cosh \infty = \infty$. Of course, this theorem is not limited to radiators with uniform surface velocity. Bouwkamp's expression [35] includes the square of average surface velocity divided by the square of the velocity at some reference point, although we have omitted this here. We will use this theorem to derive an expression for the radiation impedance of a rectangular piston in an infinite baffle.

13.14 RADIATION FROM AN INFINITELY LONG OSCILLATING STRIP IN AN INFINITE BAFFLE [36,37]

Boundary conditions. Essentially this is the limiting case of a rectangular piston as one of its dimensions tends to infinity. The infinitely long strip of width d shown in Fig. 13.40 is mounted in an infinite baffle in the xy plane and oscillates in the z direction with a harmonically time dependent velocity $\tilde{u}_0$. As with the circular piston in an infinite baffle, the monopole source elements, together with their images, coalesce to form elements of double strength. Due to the symmetry of the pressure fields on either side of the baffle, there is the following Neumann boundary condition on its surface:

$$\frac{\partial}{\partial z}\tilde{p}(x,z)\Big|_{z=0+} = 0, \qquad \begin{cases} -\infty \le x < -\dfrac{d}{2} \\ -\dfrac{d}{2} < x \le \infty \end{cases}, \tag{13.273}$$

which is satisfied automatically. On the surface of the strip there is the coupling condition

$$\frac{\partial}{\partial z}\tilde{p}(x,y)\Big|_{z=0+} = -jk\rho_0 c\tilde{u}_0, \qquad -\frac{d}{2} \le x \le \frac{d}{2}, \tag{13.274}$$

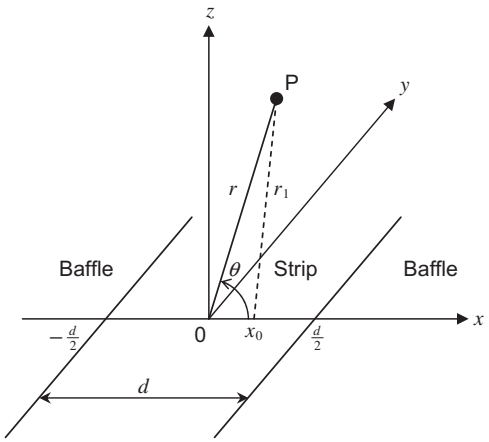

FIG. 13.40 Geometry of infinitely long rigid strip in infinite baffle. The point of observation P is located at position (*x,y,z*) in rectangular coordinates.

where ρ_0 is the density of air or any other surrounding medium, c is the speed of sound in that medium and $k = 2\pi/\lambda = \omega/c$ is the wave-number.

Far-field pressure. The pressure at point P due to a single line source at x_0 is obtained from Eq. (12.6) to give

$$\tilde{p}(r,\theta) = \frac{\rho_0 c(\tilde{U}_0/l)}{2}\sqrt{\frac{k}{2\pi r_1}}e^{-j\left(kr_1-\frac{\pi}{4}\right)}, \tag{13.275}$$

where $(\tilde{U}_0/l)$ is the volume velocity per unit length, $k = \omega/c = 2\pi/\lambda$ is the wave-number and

$$r_1^2 = r^2\cos^2\theta + (r\sin\theta - x_0)^2. \tag{13.276}$$

Hence, the pressure due to the strip is the integral across its width of Eq. (13.275) for a single line source taking into account the double strength sources and letting $\tilde{U}_0 = ld\tilde{u}_0$ as follows:

$$\tilde{p}(r,\theta) = \rho_0 c\tilde{u}_0 \int_{-\frac{d}{2}}^{\frac{d}{2}} \sqrt{\frac{k}{2\pi r_1}}e^{-j\left(kr_1-\frac{\pi}{4}\right)}dx_0. \tag{13.277}$$

At a large distance r, the terms containing r in Eq. (13.276) dominate. Hence the remaining terms can be replaced with ones that enable r_1 to be factorized as follows

$$\begin{aligned} r_1^2 &= r^2 + x_0^2 - 2rx_0\sin\theta \\ &\approx r^2 + x_0^2\sin^2\theta - 2rx_0\sin\theta \\ &= (r - x_0\sin\theta)^2, \end{aligned} \tag{13.278}$$

which after inserting into Eq. (13.277) gives

$$\begin{aligned}\tilde{p}(r,\theta) &= \rho_0 c\tilde{u}_0\sqrt{\frac{k}{2\pi r}}e^{-j\left(kr-\frac{\pi}{4}\right)}\int_{-\frac{d}{2}}^{\frac{d}{2}} e^{jkx_0\sin\theta}dx_0 \\ &= \frac{kd\rho_0 c\tilde{u}_0}{2}\sqrt{\frac{d}{\pi r}}e^{-j\left(kr-\frac{\pi}{4}\right)}D(\theta),\end{aligned} \tag{13.279}$$

where the directivity function $D(\theta)$ is given by

$$D(\theta) = \frac{\sin\left(\frac{1}{2}kd\sin\theta\right)}{\left(\frac{1}{2}kd\right)^{3/2}\sin\theta}, \tag{13.280}$$

which is the same as that of a finite line source of length d in its plane, as given by Eq. (4.89). The directivity pattern is shown in Fig. 4.18. The on-axis pressure is given by

$$D(0) = 1/\sqrt{\frac{1}{2}kd}.$$

In Sec. 2.1, we saw that in the case of a piston radiating into an infinitely long tube, the pressure $\tilde{p}$ along the tube is directly proportional to the piston velocity $\tilde{u}_0$. Assuming the tube is much narrower than the wavelength, this represents a one-dimensional system. In three-dimensional space, such as that of a piston in an infinite baffle radiating into free space, the radiated pressure is proportional to the acceleration of the piston $j\omega\tilde{u}_0$. Not surprisingly, in the two-dimensional space of an infinite strip we find that the pressure is proportional to $\sqrt{j\omega}\tilde{u}_0$.

Radiation impedance. Using the Bouwkamp impedance theorem (see Sec. 13.13), the radiated power per unit length l is given by

$$W = \left|\frac{\tilde{U}_0}{\sqrt{2}}\right|^2 \boldsymbol{R}_{AR} = \frac{l}{\rho_0 c}\int_{-\frac{\pi}{2}}^{\frac{\pi}{2}}\left|\frac{\tilde{p}(r,\theta)}{\sqrt{2}}\right|^2 rd\theta\big|_{r\to\infty}, \tag{13.281}$$

where the integration is taken over a half-cylindrical surface in the extreme far field. Using the pressure from Eq. (13.279) we obtain the real and imaginary parts of the impedance as follows:

$$\boldsymbol{R}_s = ld\boldsymbol{R}_{AR} = \rho_0 c\frac{kd}{\pi}\int_0^{\frac{\pi}{2}} D^2(\theta)d\theta, \tag{13.282}$$

$$X_s = ldX_{AR} = \rho_0 c \frac{kd}{\pi} \int_{\frac{\pi}{2}+j0}^{\frac{\pi}{2}+j\infty} D^2(\theta) d\theta, \tag{13.283}$$

where $\boldsymbol{R}_s$ is the specific radiation resistance in $\mathrm{N \cdot s/m^3}$ (rayl), where the bold $\boldsymbol{R}$ indicates that the quantity varies with frequency, and X_s is the specific radiation reactance in $\mathrm{N \cdot s/m^3}$ (rayl). Substituting $t = \sin\theta$ yields

$$\begin{aligned} \boldsymbol{R}_s = ld\boldsymbol{R}_{AR} &= \rho_0 c \frac{kd}{\pi} \int_0^1 \left(\frac{\sin\left(\frac{kd}{2}t\right)}{\frac{kd}{2}t} \right)^2 \frac{dt}{\sqrt{1-t^2}} \\ &= \rho_0 c \frac{kd}{2} {}_1F_2\left(\frac{1}{2}; \frac{3}{2}, 2; -\frac{k^2d^2}{4}\right) \\ &\approx \rho_0 c \frac{kd}{2}, \qquad kd < 0.5, \end{aligned} \tag{13.284}$$

$$\begin{aligned} X_s = ldX_{AR} &= \rho_0 c \frac{kd}{\pi} \int_1^\infty \left(\frac{\sin\left(\frac{kd}{2}t\right)}{\frac{kd}{2}t} \right)^2 \frac{dt}{\sqrt{t^2-1}} \\ &= \rho_0 c \frac{1}{kd} G^{2,1}_{2,4}\left(\frac{k^2d^2}{4} \middle| \begin{matrix} 1, \frac{3}{2} \\ 1, 1, 0, \frac{1}{2} \end{matrix} \right) \\ &\approx \rho_0 c \frac{kd}{\pi} \left(\frac{3}{2} - \gamma - \ln\left(\frac{kd}{2}\right) \right), \qquad kd < 0.5, \end{aligned} \tag{13.285}$$

where F is the hypergeometric function, G is the Meijer G function, and $\gamma = 0.5772$ is Euler's constant. Separate plots of $\boldsymbol{R}_s/\rho_0 c$ and $X_s/\rho_0 c$ are shown in Fig. 13.43 and Fig. 13.44, respectively, as a function of kd.

13.15 THE FAR-FIELD PRESSURE DISTRIBUTION AS A SPATIAL FREQUENCY SPECTRUM OF THE SOURCE VELOCITY DISTRIBUTION

Two-dimensional system. In a two-dimensional system with a planar source, the far-field pressure distribution is given by a generalized version of Eq. (13.279), where $\tilde{u}_0(x_0)$ is the source velocity distribution:

$$\begin{aligned}\tilde{p}(r,\theta) &= \rho_0 c\sqrt{\frac{k}{2\pi r}}e^{-j\left(kr-\frac{\pi}{4}\right)}\int_{-\infty}^{\infty}\tilde{u}_0(x)e^{jkx_0\sin\theta}dx_0 \\ &= -j\frac{e^{-j\left(kr+\frac{\pi}{4}\right)}}{\sqrt{2\pi kr}}\tilde{F}(k_x),\end{aligned} \tag{13.286}$$

where

$$\tilde{F}(k_x) = \int_{-\infty}^{\infty}\tilde{f}(x_0)e^{jk_x x_0}dx_0, \tag{13.287}$$

which is simply the Fourier transform or spatial frequency spectrum of the normal pressure gradient distribution $\tilde{f}(x_0)$ in the xy plane:

$$\tilde{f}(x_0) = -\frac{\partial}{\partial z_0}\tilde{p}(x_0,z_0)\Big|_{z_0=0} = jk\rho_0 c\tilde{u}(x_0), \tag{13.288}$$

where k_x is the spatial frequency of the component of a wave in the x direction given by

$$k_x = k\sin\theta. \tag{13.289}$$

In the case of a strip of infinite extent in the y direction, the velocity distribution is just a step function in the x direction:

$$f(x_0) = \begin{cases} 0, & x < -\dfrac{d}{2} \\ 1, & -\dfrac{d}{2} \le x \le \dfrac{d}{2} \\ 0, & x > -\dfrac{d}{2}. \end{cases} \tag{13.290}$$

By inspection of Eq. (13.279) we see that

$$D(k_x) = \frac{2\pi}{jkd\rho_0 c\tilde{u}_0}F(k_x) = \frac{\sin\left(\frac{1}{2}k_x d\right)}{\frac{1}{2}k_x d}. \tag{13.291}$$

Now let us convert from polar coordinates in r and θ to rectangular coordinates in x and z, using

$$r = \sqrt{z^2 + x^2}, \tag{13.292}$$

$$\sin\theta = \frac{x}{\sqrt{z^2 + x^2}} \tag{13.293}$$

and project the polar directivity pattern onto a distant parallel screen. Hence, the spatial frequency k_x at a point on the screen a horizontal distance x from the z axis is scaled by

$$k_x = k\sin\theta = \frac{kx}{\sqrt{z^2 + x^2}}. \tag{13.294}$$

At a given frequency $\omega = kc$, only the spectrum up to spatial frequency $k_x = k$ is displayed on the screen as θ varies from 0 to $\pi/2$. As the frequency is increased, more of the spectrum is shown but never the whole spectrum. We also note that the amplitude of the spectrum is scaled by $(z^2 + x^2)^{-1/4}$ due to the $1/\sqrt{r}$ term in Eq. (13.279).

Three-dimensional system. Here we consider a three-dimensional system in rectangular coordinates (x,y,z) with an arbitrary source velocity distribution in an infinite baffle in the xy plane, which radiates into half space. The pressure field is given by the Rayleigh integral of Eq. (13.6) using the Green's function given by Eq. (13.4), which for $z_0 = 0$ can be written

$$g(x, y, z|x_0, y_0, 0) = \frac{e^{-jkr_1}}{4\pi r_1}, \tag{13.295}$$

where

$$r_1^2 = (x - x_0)^2 + (y - y_0)^2 + z^2. \tag{13.296}$$

If we let $x = r\sin\theta_x$, $y = r\sin\theta_y$ and $z^2 = r^2 - x^2 - y^2$, then

$$\begin{aligned} r_1^2 &= r^2 - 2rx_0\sin\theta_x - 2ry_0\sin\theta_y + x_0^2 + y_0^2 \\ &\approx (r - x_0\sin\theta_x - y_0\sin\theta_y)^2, \qquad r^2 \gg x_0^2 + y_0^2, \end{aligned} \tag{13.297}$$

where θ_x is the angle of elevation subtended with the z axis in the x direction and θ_y is that subtended with the z axis in the y direction as follows:

$$\sin\theta_x = \frac{x}{\sqrt{x^2 + y^2 + z^2}} = \frac{x}{r}, \tag{13.298}$$

$$\sin\theta_y = \frac{y}{\sqrt{x^2 + y^2 + z^2}} = \frac{y}{r}. \tag{13.299}$$

Alternatively, in cylindrical coordinates we have $\sin\theta_x = \sin\theta\ \cos\phi$ and $\sin\theta_y = \sin\theta\sin\phi$. Inserting the Green's function of Eq. (13.295) into the Rayleigh integral of Eq. (13.6), whilst doubling the source strength due to half-space radiation, yields

$$\begin{aligned}\tilde{p}(x,y,z) &= jk\rho_0 c\frac{e^{-jkr}}{2\pi r}\int_{-\infty}^{\infty}\int_{-\infty}^{\infty}\tilde{u}(x_0,y_0)e^{jk(x_0\sin\theta_x+y_0\sin\theta_y)}dx_0dy_0 \\ &= \frac{e^{-jkr}}{2\pi r}\tilde{F}(k_x,k_y),\end{aligned} \tag{13.300}$$

where

$$\tilde{F}(k_x,k_y) = \int_{-\infty}^{\infty}\int_{-\infty}^{\infty}\tilde{f}(x_0,y_0)e^{j(k_xx_0+k_yy_0)}dx_0dy_0, \tag{13.301}$$

which is simply the Fourier transform or spatial frequency spectrum of the normal pressure gradient distribution $\tilde{f}(x_0,y_0)$ in the xy plane:

$$\tilde{f}(x_0,y_0) = -\frac{\partial}{\partial z_0}\tilde{p}(x_0,y_0,z_0)\Big|_{z_0=0} = jk\rho_0 c\tilde{u}(x_0,y_0), \tag{13.302}$$

where k_x and k_y are the spatial frequencies given by

$$k_x = k\sin\theta_x, \tag{13.303}$$

$$k_y = k\sin\theta_y, \tag{13.304}$$

and the amplitude in the distant plane is scaled by $(x^2+y^2+z^2)^{-1/2}$.

Axisymmetric three-dimensional system. In an axisymmetric system with a planar source, such as a piston in an infinite baffle, the pressure distribution is given by the Rayleigh integral of Eq. (13.6) using the Green's function given by Eq. (13.70), which for $z_0 = 0$ and $\phi = \pi/2$ can be written

$$\begin{aligned}p(r,\theta) &= jk\rho_0 c\frac{e^{jkr}}{2\pi r}\int_0^{2\pi}\int_0^{\infty}\tilde{u}(w_0)e^{jkw_0\sin\theta\sin\phi_0}w_0dw_0\phi_0 \\ &= \frac{e^{jkr}}{r}\int_0^{\infty}\tilde{f}(w_0)J_0(kw_0\sin\theta)w_0dw_0 \\ &= \frac{e^{jkr}}{r}\tilde{F}(k_w),\end{aligned} \tag{13.305}$$

where we have used Eq. (76) from Appendix II to solve the integral and

$$\tilde{F}(k_w) = \int_0^{\infty}\tilde{f}(w_0)J_0(k_ww_0)w_0dw_0, \tag{13.306}$$

which is simply the Hankel transform or spatial frequency spectrum of the normal pressure gradient distribution $\tilde{f}(w_0)$ in the w plane:

$$\tilde{f}(w_0) \;=\; -\frac{\partial}{\partial z_0}\tilde{p}(w_0, z_0)\Big|_{z_0=0} \;=\; jk\rho_0 c\tilde{u}(w_0), \tag{13.307}$$

where k_w is the spatial frequency is given by

$$k_w \;=\; k\sin\theta. \tag{13.308}$$

In the case of a piston in an infinite baffle, the velocity distribution is just a step function in the w direction:

$$\tilde{f}(w_0) \;=\; \begin{cases} jk\rho_0 c\tilde{u}_0, & 0 \le w_0 \le a \\ 0, & w_0 > a. \end{cases} \tag{13.309}$$

so that applying the integral solution of Eq. (95) from Appendix II yields

$$\begin{aligned} \tilde{F}(k_w) \;&=\; jk\rho_0 c\tilde{u}_0 \int_0^a J_0(kw_0\sin\theta) w_0 dw_0 \\ &=\; jka^2\rho_0 c\tilde{u}_0 \frac{J_1(ka\sin\theta)}{ka\sin\theta}. \end{aligned} \tag{13.310}$$

By inspection of Eq. (13.102) we see that

$$D(k_w) \;=\; \frac{2}{jka^2\rho_0 c\tilde{u}_0}\tilde{F}(k_w). \tag{13.311}$$

Now let us convert from polar coordinates in r and θ to cylindrical coordinates in w and z, using

$$r \;=\; \sqrt{z^2 + w^2}, \tag{13.312}$$

$$\sin\theta \;=\; \frac{w}{\sqrt{z^2 + w^2}}, \tag{13.313}$$

and project the polar directivity pattern onto a distant parallel screen. Hence, the spatial frequency k_w at a point on the screen a horizontal distance w from the z axis is scaled by

$$k_w \;=\; k\sin\theta \;=\; \frac{kw}{\sqrt{z^2 + w^2}}. \tag{13.314}$$

At a given frequency $\omega = kc$, only the spectrum up to spatial frequency $k_w = k$ is displayed on the screen as θ varies from 0 to $\pi/2$. As the frequency is increased, more of the spectrum is shown but never the whole spectrum. We also note that the amplitude of the spectrum is scaled by $(z^2 + w^2)^{-1/2}$ due to the $1/r$ term in Eq. (13.101).

13.16 THE BRIDGE PRODUCT THEOREM

This important theorem in acoustics is a corollary of the fact that the pressure distribution in one plane is a Fourier transform of the velocity distribution in another one which is far away and parallel to it, as discussed in the previous section. For simplicity, let us consider a two-dimensional system in the xz plane of infinite extent in the y direction. We then multiply the Fourier transform of an arbitrary velocity distribution $f(x)$ by that of a line source at x_0 as follows:

$$\begin{aligned} F(K) &= \int_{-\infty}^{\infty} f(x)\, e^{jKx} dx \times \int_{-\infty}^{\infty} \delta(x - x_0)\, e^{jKx} dx \\ &= \int_{-\infty}^{\infty} f(x)\, e^{jK(x+x_0)} dx, \end{aligned} \tag{13.315}$$

where $\delta(x - x_0)$ is the Dirac delta function and we have used the property that

$$\int_{-\infty}^{\infty} \delta(x - x_0)\, e^{jKx} dx = e^{jKx_0}. \tag{13.316}$$

If we now substitute $x' = x + x_0$, we obtain

$$F(K) = \int_{-\infty}^{\infty} f(x' - x_0) e^{jKx'} dx', \tag{13.317}$$

which is simply the Fourier transform of the original distribution $f(x)$ shifted to a new origin at x_0 as illustrated in Fig. 13.41. This is somewhat analogous to the principle of amplitude modulation whereby multiplying a baseband signal by a single tone in the time domain produces a modulated tone with "sideband" spectrums either side of the tone in the frequency domain. Here the space domain is analogous to the frequency domain and the spatial frequency domain is analogous to the time domain, since the product is taken in the latter. Seeing that the far-field pressure of a planar source is the Fourier transform of the source velocity distribution, we can use the product theorem to derive the far-field pressure for a transducer array by simply taking the product of the directivity function for a single transducer and that of any number of point sources located in the array positions, as illustrated in Fig. 13.42.

13.17 RADIATION FROM A RIGID RECTANGULAR PISTON IN AN INFINITE BAFFLE [38,39]

Far-field pressure. Using the product theorem given in Sec. 13.16, the directivity pattern is equal to the product of the directivity patterns for two line arrays at right angles to each other [see

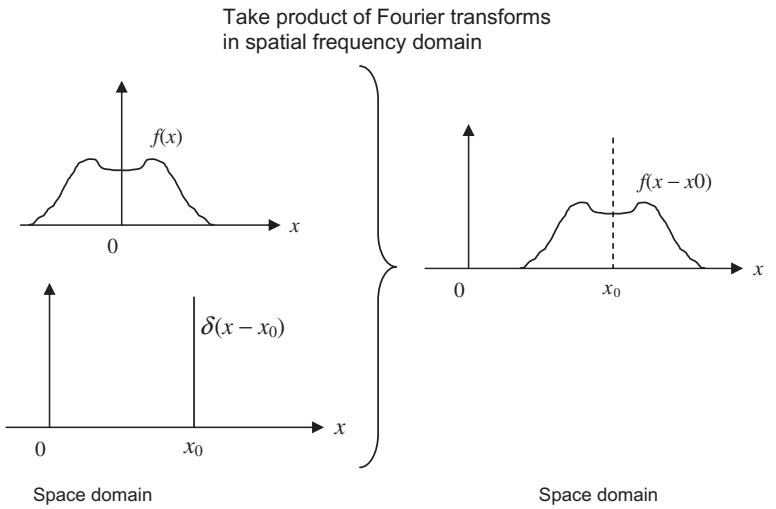

FIG. 13.41 Product theorem: Origin shifting.

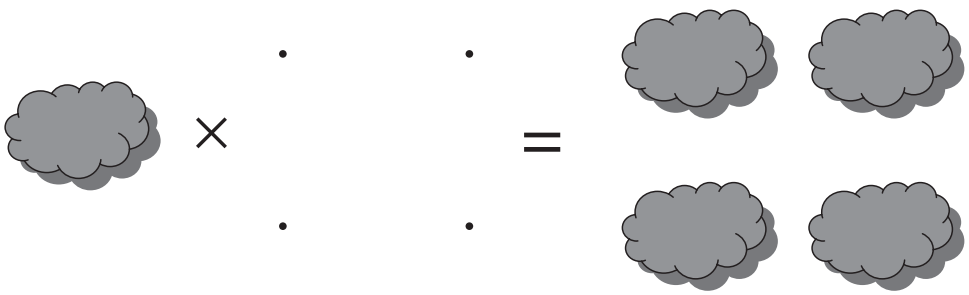

FIG. 13.42 Product theorem: Array creation.

Eq. (4.89)]. The directivity patterns for this type of radiating source with dimensions d_1 and d_2 are given by the formula

$$D(\theta_1, \theta_2) = \frac{\sin\left(\frac{1}{2}kd_1 \sin\theta_1\right)}{\frac{1}{2}kd_1 \sin\theta_1} \cdot \frac{\sin\left(\frac{1}{2}kd_2 \sin\theta_2\right)}{\frac{1}{2}kd_2 \sin\theta_2}, \tag{13.318}$$

where

θ_1 is the angle between the normal to the surface of the piston and the projection of the line joining the middle of the surface and the observation point on the plane normal to the surface and parallel to d_1.

θ_2 is the same as θ_1, with d_2 substituted for d_1.

It is often more convenient to express Eq. (13.318) in spherical coordinates using

$$\sin\theta_1 \;=\; \sin\theta\cos\phi, \qquad\qquad \sin\theta_2 \;=\; \sin\theta\sin\phi. \tag{13.319}$$

Also, we shall substitute $j_0(x) = (\sin x)/x$ to obtain

$$D(\theta,\phi) \;=\; j_0\left(\frac{1}{2}kd_1\sin\theta\cos\phi\right)\cdot j_0\left(\frac{1}{2}kd_2\sin\theta\sin\phi\right). \tag{13.320}$$

Radiation impedance. Using the Bouwkamp impedance theorem, the radiation resistance and reactance can be found by inserting Eq. (13.320) into Eqs. (13.271) and (13.272) respectively to give

$$\boldsymbol{R}_s \;=\; kd_1kd_2\frac{\rho_0 c}{\pi^2}\int_0^{\frac{\pi}{2}}\int_0^{\frac{\pi}{2}} j_0^2\left(\frac{1}{2}kd_1\sin\theta\cos\phi\right)\cdot j_0^2\left(\frac{1}{2}kd_2\sin\theta\sin\phi\right)\sin\theta\; d\theta d\phi, \tag{13.321}$$

$$X_s \;=\; -jkd_1kd_2\frac{\rho_0 c}{\pi^2}\int_0^{\frac{\pi}{2}}\int_{\frac{\pi}{2}+j0}^{\frac{\pi}{2}+j\infty} j_0^2\left(\frac{1}{2}kd_1\sin\theta\cos\phi\right)\cdot j_0^2\left(\frac{1}{2}kd_2\sin\theta\sin\phi\right)\sin\theta\; d\theta d\phi, \tag{13.322}$$

where $\boldsymbol{R}_s$ is the specific radiation resistance in $\mathrm{N\cdot s/m^3}$ (rayl), where the bold $\boldsymbol{R}$ indicates that the quantity varies with frequency, and X_s is the specific radiation reactance in $\mathrm{N\cdot s/m^3}$ (rayl). Substituting $u = \cos\theta$, together with $v = \sin\phi$, in Eq. (13.321) and $u = j\cos\theta$, together with $v = \sin\phi$, in Eq. (13.322) yields

$$\boldsymbol{R}_s \;=\; kd_1kd_2\frac{\rho_0 c}{\pi^2}\int_0^1\int_0^1 j_0^2\left(\frac{1}{2}kd_1\sqrt{1-u^2}\sqrt{1-v^2}\right)\cdot j_0^2\left(\frac{1}{2}kd_2\sqrt{1-u^2}v\right)\frac{1}{\sqrt{1-v^2}}du\,dv, \tag{13.323}$$

$$X_s \;=\; kd_1kd_2\frac{\rho_0 c}{\pi^2}\int_0^1\int_0^\infty j_0^2\left(\frac{1}{2}kd_1\sqrt{1-u^2}\sqrt{1-v^2}\right)\cdot j_0^2\left(\frac{1}{2}kd_2\sqrt{1-u^2}v\right)\frac{1}{\sqrt{1-v^2}}du\,dv. \tag{13.324}$$

An analytical solution to Eq. (13.323) can be found by expanding the Bessel functions using

$$j_0^2(x) \;=\; (\sin x)^2/x^2 \;=\; \sum_{n=1}^{\infty}\frac{(-1)^{n+1}2^{2n-1}}{(2n)!}x^{2n-2}, \tag{13.325}$$

which gives

$$\boldsymbol{R}_s \;=\; \frac{\rho_0 c}{4\sqrt{\pi}}\sum_{m=1}^{\infty}\sum_{n=1}^{\infty}\frac{(-1)^{m+n}}{\left(m-\frac{1}{2}\right)\left(n-\frac{1}{2}\right)m!n!\Gamma\left(m+n-\frac{1}{2}\right)}\left(\frac{kd_1}{2}\right)^{2m-1}\left(\frac{kd_2}{2}\right)^{2n-1}. \tag{13.326}$$

Equation (13.324) is much more complicated to solve. Firstly, the sine squared terms have to be expanded into cosine terms using Eqs. (46) and (50) from Appendix II. Then the infinite integral is solved before expanding the resulting Bessel and Struve functions. The remaining finite integral has to be split into two at $kd_1/(kd_1^2 + kd_2^2)^{1/2}$. Hence it can be shown that the following solution is obtained, which is the same as Stenzel's formula [38]

$$X_s = \frac{4\rho_0 c}{\pi}\sum_{m=0}^{\infty}\left(\frac{kd_2}{2}\right)^{2m+1}\frac{(-1)^m}{(2m+1)(m!)^2}\left\{\frac{\log\left(q+\sqrt{1+q^2}\right)}{2m+2}+q^{2m+1}\frac{\log\left(q^{-1}+\sqrt{1+q^{-2}}\right)}{2m+2}\right.$$
$$\left.+\frac{(-1)^m}{(2m+3)q}\left(\left(\left(1+q^{2m+2}\right)\sqrt{1+q^2}-\left(1+q^{2m+3}\right)\right)\right)\left(\frac{1}{2m+2}-(-1)^m\right)+f_m(q)\right)\right\}, \tag{13.327}$$

where $q = d_1/d_2$,

$$f_m(q) = \sum_{n=1}^{m}\frac{(-1)^n}{2n+1}\left(\left(1+q^{2m-2n+2}\right)\left(1+q^2\right)^{n+1/2}-1-q^{2m+3}\right)$$
$$\times\left(\frac{1}{2m+2}\binom{m}{m-n}+(-1)^{m-n}\frac{\left(2^{n-1}(n-1)!\right)^2}{(2n-1)!}+g_{m,n}(q)\right) \tag{13.328}$$

and

$$g_{m,n}(q) = \sum_{p=1}^{n}\frac{\left(2^{p-1}(p-1)!\right)^2}{(2p-1)!}\binom{m-p}{m-n}. \tag{13.329}$$

Separate plots of $\boldsymbol{R}_s/\rho_0 c$ and $X_s/\rho_0 c$ are shown in Fig. 13.43 and Fig. 13.44, respectively, as a function of kd where $d = d_2$ is the smallest dimension. Separate plots of $\boldsymbol{R}_s/\rho_0 c$ and $X_s/\rho_0 c$ are also shown in Fig. 13.45 and Fig. 13.46, respectively, as a function of ka, where a is a notional radius that gives the same circular area S as the actual area of the rectangular piston, which is given by $S = \pi a^2 = d_1 d_2$.

13.18 MUTUAL RADIATION IMPEDANCE BETWEEN RIGID CIRCULAR PISTONS IN AN INFINITE BAFFLE [40]

When a sound source is radiating in close proximity with other sources, their radiation characteristics may be affected by their acoustic interaction, depending upon their spacing. Here we consider two circular pistons, as shown in Fig. 13.47, of radius a and mounted in an infinite rigid baffle in the xy plane, which oscillate in phase in the z direction with a harmonically time dependent velocity $\tilde{u}_0$. We can apply the product theorem of Sec. 13.16 in order to obtain the directivity pattern by multiplying the directivity pattern of a single piston from Eq. (13.102) by that of two point sources from Eq. (4.80). Note that the latter is modified in order to include ϕ dependency.

$$D(\theta,\phi) = \frac{2J_1(ka\sin\theta)}{ka\sin\theta}\times\cos\left(\frac{\pi d}{\lambda}\sin\theta\sin\phi\right). \tag{13.330}$$

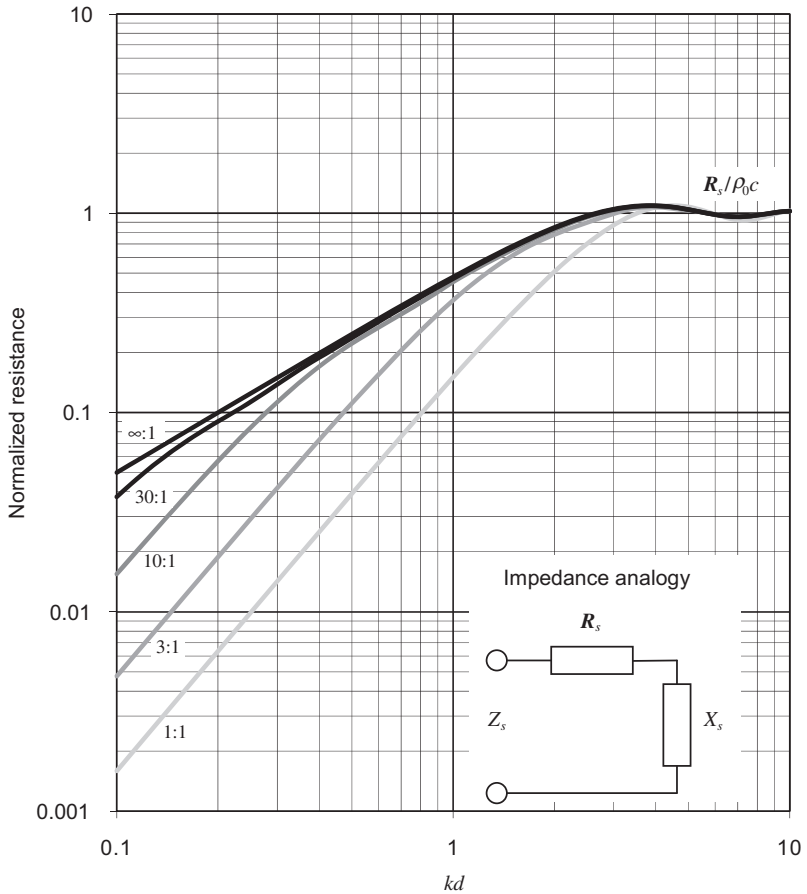

FIG. 13.43 Normalized specific radiation resistance $R_s/\rho_0 c$ of the air load on one side of a plane rectangular piston in an infinite flat baffle for five different aspect ratios d_1/d_2, where d_1 and d_2 are the dimensions of the piston.

Frequency is plotted on a normalized scale, where $kd = 2\pi d/\lambda = 2\pi f d/c$ and $d = d_2$ is the smallest dimension. In the case of $d_1/d_2 = \infty$, the impedance is that of an infinitely long strip.

We now apply the identity

$$\cos x = \sqrt{\frac{1}{2}(1 + \cos 2x)}$$

to Eq. (13.330) and insert the result into Eqs. (13.271) and (13.272) with $S = 2\pi a^2$ in order to obtain the radiation impedance by means of the Bouwkamp impedance theorem:

$$\begin{aligned} \boldsymbol{R}_s &= \boldsymbol{R}_{11} + \boldsymbol{R}_{12} \\ &= \frac{\rho_0 c}{\pi} \int_0^{2\pi} \int_0^{\frac{\pi}{2}} \frac{J_1^2(ka \sin\theta)}{\sin^2\theta} (1 + \cos(kd \sin\theta \sin\phi)) \sin\theta \, d\theta d\phi, \end{aligned} \tag{13.331}$$

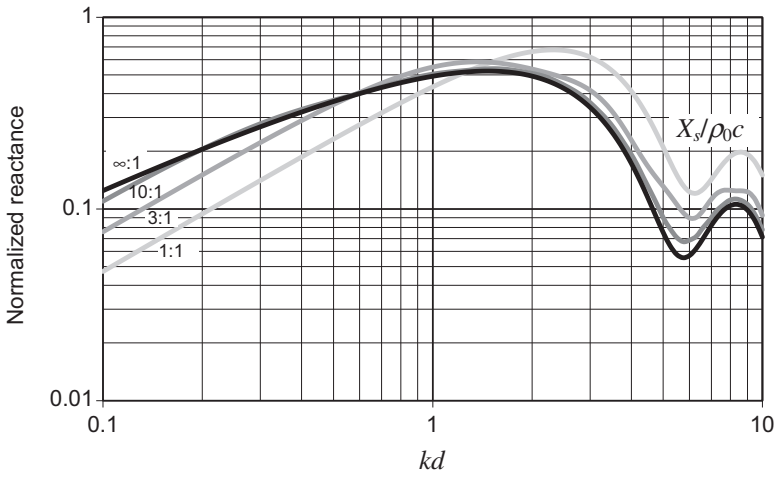

FIG. 13.44 Normalized specific radiation reactance $X_s/\rho_0 c$ of the air load on one side of a plane rectangular piston in an infinite flat baffle for four different aspect ratios d_1/d_2, where d_1 and d_2 are the dimensions of the piston.

Frequency is plotted on a normalized scale, where $kd = 2\pi d/\lambda = 2\pi f d/c$ and $d = d_2$ is the smallest dimension. In the case of $d_1/d_2 = \infty$, the impedance is that of an infinitely long strip.

where $\boldsymbol{R}_{11}$ is the *self* resistance of each piston and $\boldsymbol{R}_{12}$ is the *mutual* resistance between the two pistons. Also, the specific radiation reactance is given by

$$\begin{aligned} X_s &= X_{11} + X_{12} \\ &= -j\frac{\rho_0 c}{\pi}\int_0^{2\pi}\int_{\frac{\pi}{2}+j0}^{\frac{\pi}{2}+j\infty}\frac{J_1^2(ka\sin\theta)}{\sin^2\theta}(1+\cos(kd\sin\theta\sin\phi))\sin\theta\, d\theta\, d\phi, \end{aligned} \tag{13.332}$$

where X_{11} is the *self* reactance of each piston and X_{12} is the *mutual* reactance between the two pistons. The first term in each integral, which is independent of the spacing d, may be identified as the self impedance Z_{11} so that

$$Z_{11} = 2\rho_0 c\left(\int_0^{\frac{\pi}{2}}\frac{J_1^2(ka\sin\theta)}{\sin\theta}d\theta + \int_{\frac{\pi}{2}+j0}^{\frac{\pi}{2}+j\infty}\frac{J_1^2(ka\sin\theta)}{\sin\theta}d\theta\right), \tag{13.333}$$

which after substituting $k_w = k\sin\theta$, as discussed in Sec. 13.13, gives

$$Z_{11} = \boldsymbol{R}_{11} + jX_{11} = \rho_0 c\left\{\left(1 - \frac{J_1(ka)}{ka}\right) + j\frac{\mathbf{H}_1(ka)}{ka}\right\}. \tag{13.334}$$

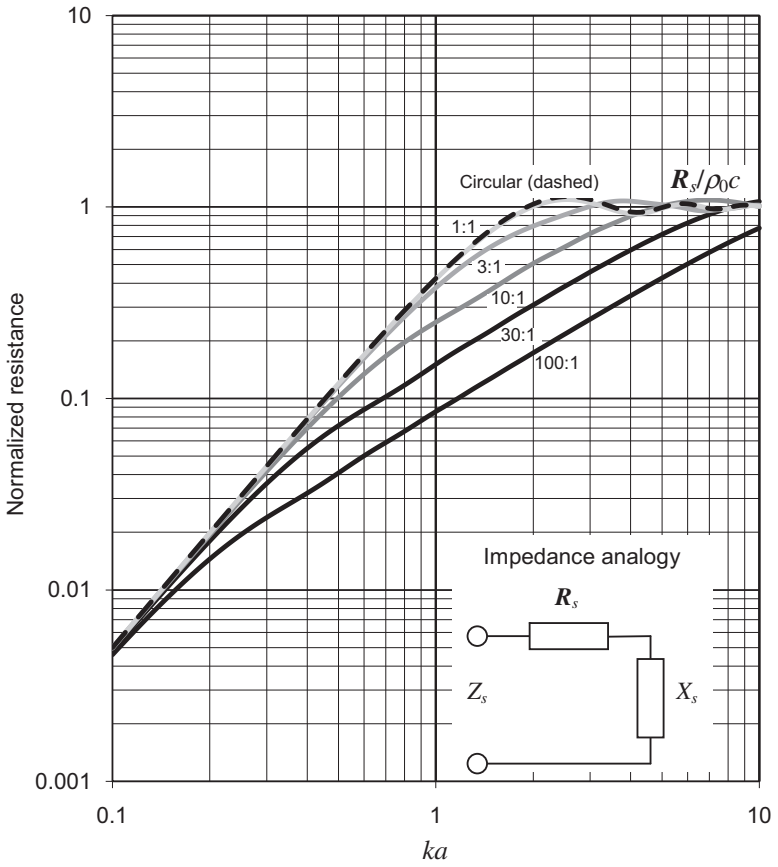

FIG. 13.45 Normalized specific radiation resistance $R_s/\rho_0 c$ of the air load on one side of a plane rectangular piston in an infinite flat baffle for five different aspect ratios d_1/d_2, where d_1 and d_2 are the dimensions of the piston.

Frequency is plotted on a normalized scale, where $ka = 2\pi a/\lambda = 2\pi fa/c$ and a is a notional radius that gives the same circular area S as the actual area of the rectangular piston, which is given by $S = \pi a^2 = d_1 d_2$.

The second term in each integral then gives the mutual impedance Z_{12} so that, after integrating over ϕ using the integral solution of Eq. (77) in Appendix II (with $z = kd \sin\theta$), we have

$$Z_{12} = 2\rho_0 c \left(\int_0^{\frac{\pi}{2}} \frac{J_1^2(ka\sin\theta)}{\sin\theta} J_0(kd\sin\theta)\, d\theta + \int_{\frac{\pi}{2}+j0}^{\frac{\pi}{2}+j\infty} \frac{J_1^2(ka\sin\theta)}{\sin\theta} J_0(kd\sin\theta)\, d\theta \right), \qquad (13.335)$$

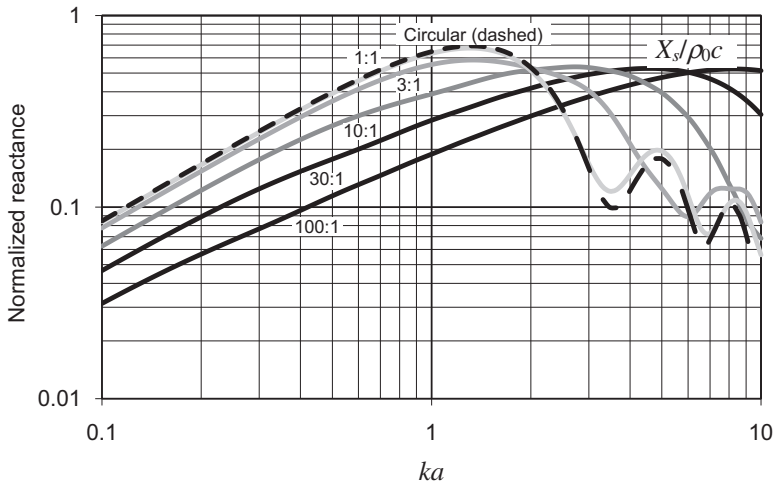

FIG. 13.46 Normalized specific radiation reactance $X_s/\rho_0 c$ of the air load on one side of a plane rectangular piston in an infinite flat baffle for five different aspect ratios d_1/d_2, where d_1 and d_2 are the dimensions of the piston.

Frequency is plotted on a normalized scale, where $ka = 2\pi a/\lambda = 2\pi fa/c$ and a is a notional radius that gives the same circular area S as the actual area of the rectangular piston, which is given by $S = \pi a^2 = d_1 d_2$.

which, after substituting $s = \sin\theta$ becomes

$$Z_{12} = 2\rho_0 c\left(\int_0^1 \frac{J_1^2(kas)}{s\sqrt{1-s^2}} J_0(kds)ds + \int_1^\infty \frac{J_1^2(kas)}{s\sqrt{1-s^2}} J_0(kds)ds\right). \tag{13.336}$$

We then expand the J_1 functions using the following Lommel expansion:

$$J_v(kas) = s^v \sum_{m=0}^{\infty} \left(\frac{ka}{2}\right)^m \frac{(1-s^2)^m}{m!} J_{v+m}(ka) \tag{13.337}$$

to give

$$Z_{12} = 2\sum_{m=0}^{\infty}\sum_{n=0}^{\infty}\left(\frac{ka}{2}\right)^{m+n}\frac{J_{m+1}(ka)J_{n+1}(ka)}{m!n!} \times\left(\int_0^1 J_0(kds)(1-s^2)^{m+n-\frac{1}{2}}sds + j(-1)^{m+n}\int_1^\infty J_0(kds)(s^2-1)^{m+n-\frac{1}{2}}sds\right), \tag{13.338}$$

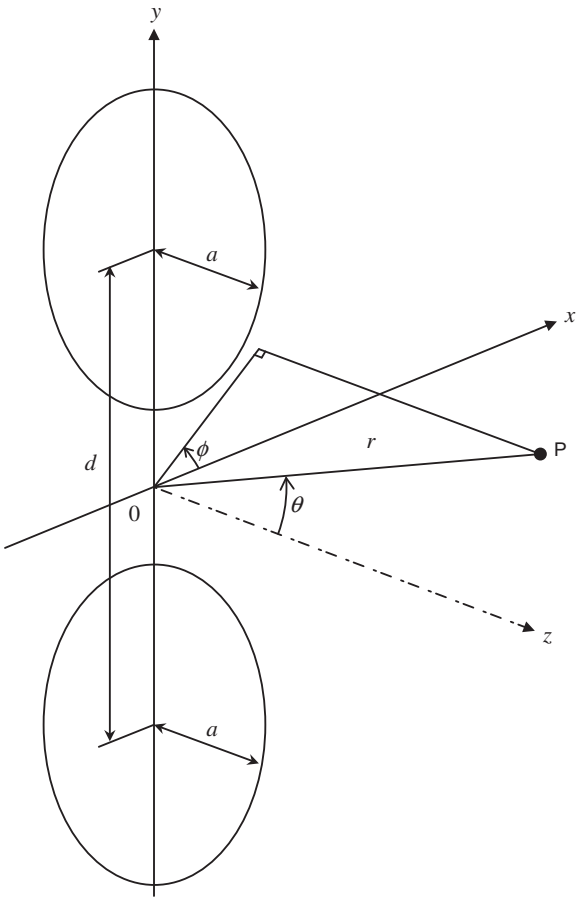

FIG. 13.47 Geometry of two circular pistons in an infinite baffle. The point of observation P is located at a distance *r* from the origin and elevation angle θ with respect to the *z* axis.

which can be solved with help from Eqs. (96), (97), and (98) from Appendix II to yield

$$Z_{12} = \boldsymbol{R}_{12} + jX_{12} = \frac{2\rho_0 c}{\sqrt{\pi}} \sum_{m=0}^{\infty} \sum_{n=0}^{\infty} \left(\frac{ka}{kd}\right)^{m+n} \frac{\Gamma\left(m+n+\frac{1}{2}\right) J_{m+1}(ka) J_{n+1}(ka)}{m!n!} h_{m+n}^{(2)}(kd) \tag{13.339}$$

where $h_{m+n}^{(2)}$ is the spherical Hankel function defined in Eq. (133) in Appendix II. For very large wavelengths and separations, where $ka << 1$ and $d >> a$, we have

$$Z_{12} = \boldsymbol{R}_{12} + jX_{12} = \rho_0 c \frac{k^2 a^2}{2} \left(\frac{\sin kd}{kd} + j\frac{\cos kd}{kd}\right), \tag{13.340}$$

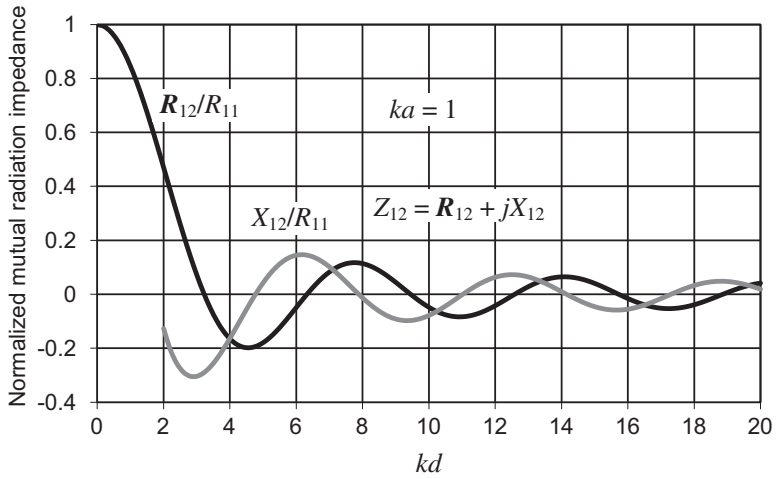

FIG. 13.48 Real and imaginary parts of the normalized mutual radiation impedance Z_{12} of the air load on one side of two plane circular pistons of radius *a* and separation *d* in an infinite flat baffle.

Relative separation is plotted on a normalized scale, where $kd = 2\pi d/\lambda = 2\pi fd/c$ and $ka = 1$.

where $\boldsymbol{R}_{11} = (ka)^2/2$. Plots of the real normalized mutual radiation resistance (R_{12}/R_{11}) and reactance (X_{12}/R_{11}) for $ka = 1$ are shown in Fig. 13.48 as a function of kd.

13.19 NEAR-FIELD ACOUSTICAL HOLOGRAPHY [41]

The forward problem. In Sec. 13.3 we stated that an infinite plane counts as a closed surface over which a boundary surface integral may be evaluated because it isolates the sources on one side of the plane from the observation field on the other. You will also recall from Sec. 13.15 that the far-field pressure distribution is the Fourier transform of the velocity distribution over an infinite plane. In order to calculate the near-field pressure we also have to take the inverse Fourier transform, and this technique is known as near-field acoustical holography. If we take the integral Green's function of Eq. (13.33) and insert it into the dipole part of the Kirchhoff–Helmholtz boundary integral of Eq. (13.28) or dipole Rayleigh integral, we obtain

$$\tilde{p}(x,y,z) = \frac{1}{8\pi^2}\int_{-\infty}^{\infty}\int_{-\infty}^{\infty} 2\tilde{p}_0(x_0,y_0,z_0)\int_{-\infty}^{\infty}\int_{-\infty}^{\infty} e^{-j(k_x(x-x_0)+k_y(y-y_0)+k_z(z-z_0))}dk_x dk_y dx_0 dy_0, \tag{13.342}$$

which gives the pressure $\tilde{p}(x,y,z)$ in the z-plane in terms of the pressure $\tilde{p}_0(x_0,y_0,z_0)$ on *both* faces of the z_0-plane. The *forward* problem is defined as the one where the field is calculated for $z \geq z_0$ and all sources are located in the region $z \leq z_0$. Rearranging the integrals gives

$$\tilde{p}(x,y,z) = \frac{1}{4\pi^2}\int_{-\infty}^{\infty}\int_{-\infty}^{\infty} e^{-jk_z(z-z_0)} \int_{-\infty}^{\infty}\int_{-\infty}^{\infty} \tilde{p}_0(x_0,y_0,z_0)e^{j(k_x x_0+k_y y_0)}dx_0dy_0e^{-j(k_x x+k_y y)}dk_xdk_y. \tag{13.343}$$

where

$$k_z = \begin{cases} \sqrt{k^2-k_x^2-k_y^2}, & k_x^2+k_y^2 \le k^2 \\ -j\sqrt{k_x^2+k_y^2-k^2}, & k_x^2+k_y^2 > k^2 \end{cases} \tag{13.344}$$

We shall now reconstruct this equation by a different method in three simple steps. First, we take the spatial Fourier transform of the pressure in the z_0-plane:

$$\tilde{P}(k_x,k_y,z_0) = \int_{-\infty}^{\infty}\int_{-\infty}^{\infty} \tilde{p}_0(x_0,y_0,z_0)e^{j(k_x x_0+k_y y_0)}dx_0dy_0 \tag{13.345}$$

The transformed pressure $\tilde{P}(k_x,k_y,z_0)$ contains no references to the spatial ordinates x and y. It is simply the wave-number spectra, each component of which represents a plane harmonic traveling wave, provided that the associated wave-number is real. However, non-propagating evanescent fields can exist, in which case the transform component represents a field of uniform phase that oscillates in time, but not in space, and decays exponentially with distance. Next, the wave-number spectra is propagated in k-space to the parallel z-plane by multiplying it with an exponent propagator term as follows

$$\tilde{P}(k_x,k_y,z_0,z) = e^{-jk_z(z-z_0)}\tilde{P}(k_x,k_y,z_0) \tag{13.346}$$

Over values of k_x and k_y for which k_z is real, the propagator is simply a phase term which does not affect the amplitude of the spectra. However, when k_z is imaginary, the propagator becomes a decaying exponent which when multiplied with the spectra represents non-propagating evanescent waves. Finally, we take the inverse Fourier transform in order to construct the pressure field in the z-plane which is essentially the sum of all the fields produced by each component of the wave-number spectra:

$$\tilde{p}(x,y,z) = \frac{1}{4\pi^2}\int_{-\infty}^{\infty}\int_{-\infty}^{\infty} \tilde{P}(k_x,k_y,z_0,z)e^{-j(k_x x+k_y y)}dk_xdk_y \tag{13.347}$$

Combining Eq. (13.347) with Eqs. (13.344) and (13.346) gives Eq. (13.343). However, Eq. (13.347) has computational and interpretational advantages over the Rayleigh integral and is particularly amenable to the digital processing of sound fields captured by planar microphone arrays in order to calculate the entire sound field of interest.

The reverse problem. It turns out that we can apply exactly the same equations that were used for the forward problem, above, to the inverse problem, where the field is calculated for $z \le z_0$ and all sources are also located in the region $z \le z_0$. The only difference now is that over values of k_x and k_y for which k_z is imaginary, the propagator becomes a growing exponent because the non-propagating evanescent waves increase in strength when approaching the sources.

13.20 TIME-REVERSAL

Imagine that we place a planar array of microphones between a stage and an audience and then make a recording of a performance by musicians on the stage. We assume that the extent of the array is large enough to be considered infinite and that the microphones are small enough and far enough apart not to disturb the sound field produced. We also assume that the ratio of the smallest wavelength to the microphone pitch is large enough not to introduce spatial aliasing. If we play back the recording through an infinite array of either omnidirectional (monopole) or bidirectional (dipole) loudspeakers in place of the microphones (making the same assumptions as with the microphones), we will faithfully reproduce the concert when listening from the audience side of the array. However, if we listen from the stage side, we will not hear what was heard by the musicians, but that which was heard by the audience. Reproducing a sound field with sources in it is not so easy. Near-field acoustical holography, as described in the previous section, only provides a way to *calculate* the sound field on the stage side. In other words, we only have a virtual field, not a real one.

In time reversal, we play the recording backwards. Although this obviously makes no sense for music, it does have an interesting effect in the case of signals such as a continuous tone or an impulse. During the recording, an impulse arrives at the middle microphone first and then the ones either side of that and works its way progressively towards the outermost microphones. During normal playback, the impulse leaves the loudspeakers in the same order as it arrived at the corresponding microphones, but if the recording is played backwards the sound emanates in reverse order starting from the outermost loudspeakers and finishing from the middle one. The effect of this is to focus the sound towards the source from which it was originally produced during the recording. If the sound was produced by a point source [see Eq. (4.71)], will the original source be faithfully reproduced?

In order to answer that question, let us now consider a simpler example. Suppose now that we have a spherical wave converging towards a point. If there is no source or sink at the focal point, the spherical wave will pass through the focal point and re-emerge as a diverging wave. From Eq. (2.99) we have

$$\tilde{p}(r) = \tilde{A}_+ \frac{e^{-jkr}}{r} + \tilde{A}_- \frac{e^{jkr}}{r}, \tag{13.348}$$

where $\tilde{A}_-$ is the amplitude of the sound pressure in the incoming wave at unit distance from the center of the sphere and $\tilde{A}_+$ is the same for the outgoing wave. In order to meet the boundary condition of pressure continuity, or zero pressure gradient, at the center, we set $\tilde{A}_+ = -\tilde{A}_-$ so that

$$\tilde{p}(r) = 2j\,\tilde{A}_- \frac{\sin kr}{r}, \tag{13.349}$$

The incoming wave is reflected back out again as if there were a rigid termination point at the center. In order to absorb it we have to place a point sink $-\tilde{A}_+ e^{-jkr}/r$ at the center. It has been pointed out that, when time reversing the waves produced by dropping a pebble into a pond, a pebble must rise out of the water at the end of the sequence. [44] In the case of a plane wave, it is relatively straight forward to absorb it using a $\rho_0 c$ termination as was shown in Sec. 2.4. In the case of a converging spherical wave, the characteristic impedance is only approximately $\rho_0 c$ at a distance of several wavelengths from the center, as demonstrated by Eq. (2.109). At closer distances, the impedance is mainly massive. Therefore, a sphere whose surface impedance is $\rho_0 c$ can only be used as an acoustic sink to absorb an incoming spherical wave if it has a diameter of several wavelengths.

If we now return to the problem of the planar loudspeaker array, the same principle applies. In the absence of any acoustic sink, the waves converge upon the point from which the sound originally emanated and re-emerge on the opposite side. As they pass through the focal point, there is a transition from the positive phase angle of the converging wave to the negative phase angle of the diverging one. Hence the imaginary part of the pressure field is zero in the plane of the focal point where the converging and diverging waves meet. In this way, the singularity of the original point source is removed and we are left with an approximation of it.

References

[1] Morse PM, Ingard KU. Theoretical Acoustics. New York: McGraw-Hill; 1968. p. 319–321. It should be noted that their derivation uses a bounded Green's function which accounts for the reflections from the boundary which have nothing to do with the boundary integral.

[2] Rayleigh JWS. The Theory of Sound, vol. II. New York: Dover; 1945. p. 107 & 109. Interestingly, Rayleigh derives Eqs. (13.27). and (13.28) by shrinking the volume integral of Eq. (13.25) down to a plane and then applying the appropriate boundary conditions in the plane.

[3] Arfken GB, Weber HJ. Mathematical Methods for Physicists, 6th ed. Florida: Academic Press; 2005. p. 60, Eq. (1.101a), p. 61, Eq. (1.104).

[4] Morse PM, Ingard KU. Theoretical Acoustics. New York: McGraw-Hill; 1968. p. 364–365.

[5] Lamb H. On the Propagation of Tremors Over the Surface of an Elastic Solid. Philos Trans R Soc London, Ser. A 1904;203:1–42.

[6] Sommerfeld A. Über die Ausbreitung der Wellen in der drahtlosen Telegraphie (On the Propagation of Waves in Wireless Telegraphy). Ann Phys 1909;4(28):665–736.

[7] Skudrzyk E. The Foundations of Acoustics: Basic Mathematics and Basic Acoustics. Wien: Springer-Verlag; 1971. p. 658.

[8] Watson GN. A Treatise on the Theory of Bessel Functions. 2nd ed. London: Cambridge University Press; 1944. Ch. XI.

[9] Rayleigh JWS. The Theory of Sound, vol. II. New York: Dover; 1945. p. 107 and 162.

[10] Chester Rice W, Kellogg Edward W. Notes on the Development of a New Type of Hornless Loudspeaker. Trans Am Inst Elec Eng 1925;44:461–75. Reprinted J Audio Eng Soc (1982);30(7/8):512–521. U.S. Patent No. 1,795,214.

[11] King LV. On the Acoustic Radiation Field of the Piezoelectric Oscillator and the Effect of Viscosity on the Transmission. Can. J. Res 1934;11:135–46.

[12] Mast TD, Yu F. Simplified Expansions for Radiation from a Baffled Circular Piston. J Acoust Soc Am 2005;118(6):3457–64.

[13] Stenzel H. Über die Berechnung des Schallfeldes einer kreisförmigen Kolbenmembran (On the Calculation of the Sound Field of a Circular Piston Diaphragm). Electr Nacr Tech 1935;12:16–30.

[14] Rayleigh JWS. The Theory of Sound, vol. II. New York: Dover; 1945. p. 138–146.

[15] Kuntz HL. Radiated Sound and the Geometric Nearfield. Noise Control Eng J 2008;56(4):269–81.

[16] Mellow TJ. On the Sound Field of a Resilient Disk in Free Space. J Acoust Soc Am 2008;123(4):90–101.

[17] Walker PJ. New Developments in Electrostatic Loudspeakers. J Audio Eng Soc 1980;28(11):795–9.

[18] Mellow TJ, Kärkkäinen LM. On the Sound Field of a Circular Membrane in Free Space and an Infinite Baffle. J Acoust Soc Am 2006;120(5):2460–77.

[19] Mellow TJ. On the Sound Field of a Resilient Disk in an Infinite Baffle. J Acoust Soc Am 2006;120(1): 90–101.

[20] Bouwkamp CJ. Theoretical and Numerical Treatment of Diffraction Through a Circular Aperture. IEEE Trans. Antennas and Propagation 1970;AP18–2:152–76. This is a translation of his PhD dissertation originally published in Dutch in 1941.

[21] Spence RD. A Note on the Kirchhoff Approximation in Diffraction Theory. J Acoust Soc Am 1949;21(2):98–100.
[22] Streng JH. Calculation of the Surface Pressure on a Vibrating Circular Stretched Membrane in Free Space. J Acoust Soc Am 1987;82(2):679–86.
[23] Mellow TJ, Kärkkäinen LM. On the Sound Field of an Oscillating Disk in an Open and Closed Circular Baffle. J Acoust Soc Am 2005;118(3):1311–25.
[24] Mellow TJ, Kärkkäinen LM. A Dipole Loudspeaker with a Balanced Directivity Pattern. J Acoust Soc Am 2010;128(5):2749–57.
[25] Nimura T, Watanabe Y. Effect of a Finite Circular Baffle Board on Acoustic Radiation. J Acoust Soc Am 1952;25(1):76–80.
[26] Sommerfeld A. Die frei schwingende Kolbenmembran (The Freely Oscillating Piston Membrane). Ann Phys 1942/3;5(42):389–420.
[27] Meixner J, Fritze U. Das Schallfeld in der nähe einer frei schwingenden Kolbenmembran (The Sound Field in the Vicinity of a Freely Oscillating Piston Diaphragm). Z. angew. Physik 1949;1:535–42.
[28] Wiener FM. On the Relation between the Sound Fields Radiated and Diffracted by Plane Obstacles. J Acoust Soc Am 1951;23:697–700.
[29] Streng JH. Calculation of Integrals which Occur in the Analysis of Circular Stretched Membrane Sound Radiation. J Acoust Soc Am 1988;83(3):1183–5.
[30] Mellow TJ, Kärkkäinen LM. On the Sound Field of an Oscillating Disk in an Open and Closed Circular Baffle. J Acoust Soc Am 2005;118(3):1–15.
[31] Levine H, Schwinger J. On the Radiation of Sound from an Unflanged Circular Pipe. Phys Rev Feb. 15, 1948;73:383–406.
[32] Babinet J. Mémoires d'optique météorologique (Memoirs on Meteorological Optics). C. R. Acad Sci Paris 1837;4:638.
[33] Kirchhoff G. Zur Theorie der Lichtstrahlen (On the Theory of Light Radiation). Sitz-Ber kgl preuβ Akad Wiss 22 June 1882:641–69.
[34] Wiener FM. On the Relation Between the Sound Fields Radiated and Diffracted by Plane Obstacles. J Acoust Soc Am 1951;23(6):697–700.
[35] Bouwkamp CJ. A Contribution to the Theory of Acoustic Radiation. Philips Research Rep 1945;1:251–77.
[36] Lipshitz SP, Scott TC, Salvy B. On the Acoustic Impedance of Baffled Strip Radiators. J Audio Eng Soc 1995;43(7/8):573–80.
[37] Mellow TJ, Kärkkäinen LM. On the Sound Fields of Infinitely Long Strips. J Acoust Soc Am 2011;130(1):153–67.
[38] Stenzel H. Die akustische Strahlung der rechteckigen Kolbenmembran (The Acoustic Radiation of the Rectangular Piston Diaphragm). Acustica 1952;2:263–81.
[39] Bank G, Wright JR. Radiation Impedance Calculations for a Rectangular Piston. J Audio Eng Soc 1990;38(5):350–4.
[40] Pritchard RL. Mutual Acoustic Impedance Between Radiators in an Infinite Baffle. J Acoust Soc Am 1960;32(6):730–7. The paper also includes an illustrative example of how the mutual radiation impedance can be calculated for a seven-piston hexagonal array.
[41] Williams EG. Fourier Acoustics: Sound Radiation and Nearfield Acoustical Holography. San Diego: Academic Press; 1999.
[42] Aarts RM, Janssen AJEM. On-axis and far-field sound radiation from resilient flat and dome-shaped radiators. J Acoust Soc Am 2009;125(3):1444–55.
[43] Mellow TJ, Kärkkäinen LM. Comparison of spheroidal and eigenfunction-expansion trial functions for a membrane in an infinite baffle. J Acoust Soc Am 2008;123(5):2598–602.
[44] Anderson BE, Griffa M, Larmar C, Ultrich AJ, Johnson PA. Timing reversal. Acoustics Today 2008;4(1):5–15.